Department of Precision and Microsystems Engineering

Study of multilayer thin film spaceplates

J.P.L. Ovaa

Report no : 2025.018
Professor : Fabian Maucher
Specialization : Optics
Type of report : MSc thesis report
Date : 17 June 2025

Study of multilayer thin film spaceplates

by

J.P.L. Ovaa

to obtain the degree of Master of Science
at the Delft University of Technology,
to be defended publicly on Wednesday July 2nd, 2025 at 14:00 PM.

Student number:	5148758	
Project duration:	September 1, 2024 – July 2, 2025	
Thesis committee:	Dr. F. Maucher,	TU Delft, supervisor
	Dr. N. Bhattacharya,	TU Delft
	Dr. S.F. Pereira,	TU Delft
Other:	Dr. R. Kohlhaas,	SRON, supervisor

TU Delft SRON

Abstract

Miniaturizing optical systems is necessary and useful for many different applications, such as cameras and optical sensors. Recent breakthroughs in metalenses have enabled ultra-thin optical components, driving efforts to reduce the free space propagation distances between them. This can be done using devices called spaceplates, which mimic the phase response of free space propagation within a shorter relative distance. This thesis investigates the properties of theoretical spaceplates comprised of multilayer thin film structures, designed through optimization. It explores the limits of achievable effective distances by stacking devices, ultimately demonstrating a theoretical effective distance of 23.3 mm for an NA of 0.087 and 1550 nm wavelength. It also finds manufacturing errors have a significant influence on this metric, reducing achievable effective distances to millimeter scales. Lastly, it explores combining the spaceplate function with angular stray light filtering to achieve multifunctional designs, with promising results.

Preface

Doing this thesis project was an amazing experience. I thoroughly enjoyed the process of solving problems in code, figuring out the underlying physics of unexpected behavior, and being allowed to completely get lost in a single topic for a full academic year. I want to thank Dr. Fabian Maucher and Dr. Ralf Kohlhaas, both of whom brought many insights and new questions to the table without which I would never have succeeded. Besides that, they were both enthusiastic about my project with me, which was very motivating. I also want to thank my girlfriend Alejandra for cheering me on, listening to my frustrated ramblings when I got stuck with problems, and celebrating with me when I solved them. I hope the thesis report is as enjoyable for you to read as doing the project was to me, or at least as interesting.

J.P.L. Ovaa
Delft, June 2025

Contents

1

Introduction and context

The field of optics has known a long history, seeing some of its first real application in lenses for vision correction in (and possibly before) the 13th century (Darrigol, 2012). In 1608 it was demonstrated by the invention of the telescope by Hans Lippershey that by putting lenses at certain distances from one another, light can be manipulated into projecting images in many different sizes and orientations, opening up a world of possibilities (Historiek.nl, 2024). In 1865, James C. Maxwell described light as being an electromagnetic wave, furthering the understanding of its behavior, like diffraction and interference patterns (Maxwell, 1865). This understanding then forms the basis for modern thin film optics. The design of thin film structures permits manipulation of transmitted light, particularly in the spectral domain. It can do so by creating resonant cavities between interfaces between different media, where the wave will partially be reflected. When periodic, analytical expressions can be found which allow for instance the creation of near-perfect mirrors, otherwise known as Bragg mirrors (Horsley et al., 2014). In the past few decades, manufacturing techniques have become so advanced they allow even more complex optics, through the use of photonic metamaterials. These materials have sub-wavelength sized features in the plane (essentially 2D-features), which are shaped in such a way they shape the phase profile of transmitted light. This way, ultra-thin and completely flat lenses can be made (Arbabi and Faraon, 2023).

Like in many other technological fields, with the advancements of fabrication came the possibility to make systems smaller and more efficient, by creating better and stronger lenses and making clever use of the understanding of light as a wave. The rise of metalenses has helped accelerating this effort, since they are so thin and highly customizable. However, when miniaturizing an optical system, there are two main parts one must consider: the lenses themselves, and the free space between them. This space is needed to allow phase profiles of light to propagate to the correct shape, like in the case where a converging beam needs a certain distance to focus to a point after passing through a lens. The presence of this space becomes glaringly obvious when one looks at any typical telescope or photo camera: the most simple versions of these systems only contain a few lenses which are meticulously put at given distances of free space to achieve the desired effect. In many systems, this makes free space a critical factor affecting system size.

For that reason, a new type of optical element was recently proposed which has the ability to compress this space by enacting the required phase shift over a shorter distance than the free space associated with that phase shift (Reshef et al., 2021), as can be seen in figure 1.1. This means that for a distance d_{eff} in free space a spaceplate of thickness $d \leq d_{eff}$ can enact the same operation on light, compressing it by a factor $R = d_{eff}/d$, otherwise known as the compression ratio.

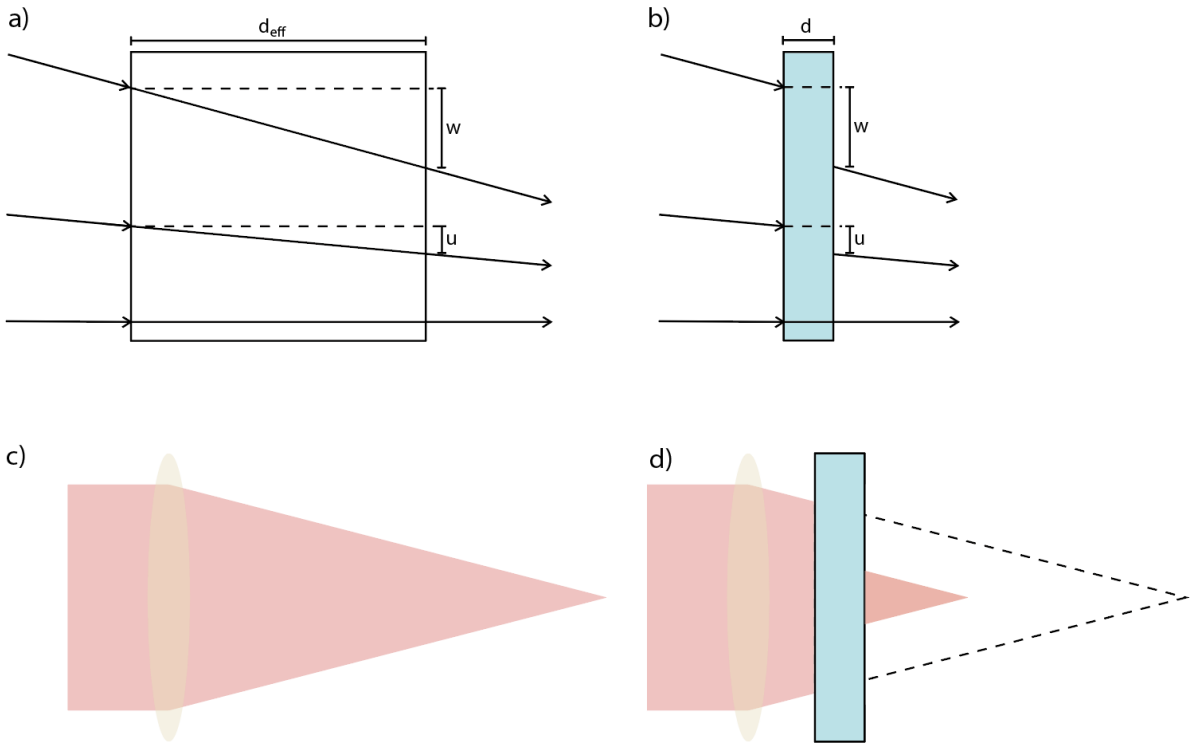

Figure 1.1: **a** Propagation through free space. **b** Propagation through spaceplate with same effective distance as in a. **c** Focusing through a lens in free space. **d** Focusing through a lens together with a spaceplate.

Having access to spaceplates would enable many optical systems to shrink down significantly. Furthermore, by combining them with the previously mentioned metalenses it would theoretically become possible to attach all components of the optical system together into one monolithic structure without the need for very complicated fixtures, as all components have flat surfaces.

To be able to compress space this way, a spaceplate needs to impart a phase to the incoming light, depending only on the incoming angle, as further explained in section 1.1. Since the first proposition of spaceplates, multiple new techniques have been proposed to achieve this effect in different ways, as are shown in section 1.2.

Out of these techniques, the use of thin film stacks was chosen to further investigate in this thesis. Multilayer thin film optics are understood very well, and relatively easy to fabricate using modern techniques (Danielzik et al., 2003). While the same effect might be possible using photonic metamaterials, taking a step back into multilayer thin films to create them might prove easier. Specifically, the question in this thesis was whether effective distances can be reached that may have possible uses in earth observation instruments for satellites, as miniaturization of those systems would be very valuable, both for weight and size requirements. This would require them to reach effective distances in the range of centimeters. Additionally, during this project it was found that thin film stacks also have a capability for filtering out angular stray light, which leads to a possibility of a multifunctional spaceplate. Therefore, angular stray light filtering using multilayer thin film stacks and the eventual combination with spaceplate functionality was also explored.

To investigate these questions, first the fundamental limits from literature are examined in section 1.3, along with other literature concerning the use of thin film stacks to create multifunctional spaceplates and angular stray light filters in sections 1.4 and 1.5. Then will follow the methods used to evaluate the properties of and optimize the thin film multilayer stacks, in chapter 2. The results of this research can be found in chapter 3, of which the resultant conclusions and discussions can be found in chapter 4.

1.1. Spaceplate basic principles

The concept of spaceplates was first introduced in Reshef et al., 2021. In their article, they explain the idea of an optic which transforms the phase profile of an incoming wave into the phase profile expected

from free space propagation, but within a smaller distance, meaning it compresses the necessary propagation space for the optical system. In very simple terms, a spaceplate enables light to travel between two planes as if it is in the background medium, but it does so in an actual distance smaller than the simulated propagation distance.

The propagation of the electric field $E(x, y, z)$ of a known plane wave with free space wavenumber $k_0 = \omega/c$ can be described by the Helmholtz equation, which follows from Maxwell's equations:

$$\nabla^2 E + k_0^2 E = 0 \tag{1.1}$$

Then taking apart the transverse (xy) and z-component of the Laplacian operator:

$$\frac{\partial^2}{\partial z^2} E + \left(\frac{\partial^2}{\partial x^2} + \frac{\partial^2}{\partial y^2}\right) E + k_0^2 E = 0 \tag{1.2}$$

Enacting the Fourier transform in the x- and y-direction where $F_{xy}\{E(x, y, z)\} = \hat{E}(k_x, k_y, z)$ will give:

$$\frac{\partial^2}{\partial z^2} \hat{E} + (k_0^2 - k_x^2 - k_y^2)\hat{E} = 0 \tag{1.3}$$

This is a simple differential equation, which has a possible solution:

$$\hat{E}(k_x, k_y, z) = \hat{E}(k_x, k_y, 0) \exp iz\sqrt{k_0^2 - k_x^2 - k_y^2} \tag{1.4}$$

This shows that the transfer function corresponding to free space propagation is:

$$H(k_x, k_y, z) = \exp iz\sqrt{k_0^2 - k_x^2 - k_y^2} \tag{1.5}$$

And so a plane wave's unhindered phase difference in a homogeneous medium between two points along the z-axis separated by a distance d_{eff} is the following:

$$\varphi_{SP}(k_0, k_x, k_y, d_{eff}) = d_{eff}\sqrt{k_0^2 - k_x^2 - k_y^2} = d_{eff} k_0 \cos\theta = k_z d_{eff} \tag{1.6}$$

Where θ is the angle between the k-vector and the z-axis. It is not named inside the function φ_{SP} since it is inherent to the vector form of k (being a vector with k_x, k_y, k_z as its components and magnitude k_0). An ideal spaceplate would impart this exact phase while being thinner than d_{eff}, thereby compressing the space with a factor $R = d_{eff}/d$, where d is the spaceplate's actual thickness.

This phase response is only dependent on the incoming angle and wavelength (i.e. values k_x and k_y) and should respond the same regardless of x, y coordinates. This operation is dependent on the input electric field at a certain region on the first interface, since the critical values k_x and k_y can only be determined by knowing the value of E over a region. This makes the spaceplate a non-local optic. This type of optical element is the exact opposite of an ideal thin lens, which will have a phase response dependent only on the local properties of the lens at a certain distance from the optical axis, and independent of the larger shape of the incoming electric field.

In further sections the transverse components of the k-vector, k_x and k_y, are combined in scalar k_{tv}, having magnitude $k_{tv} = \sqrt{k_x^2 + k_y^2}$. This can be done, since these systems usually use transversely invariant structures, making it possible to model them in 2D. Important to note about this quantity is that, due to the continuity condition over an interface, it will be the same regardless of the medium for any transversely invariant structure, like those mentioned in sections 1.2.2, 1.2.3 and 1.2.4.

1.2. Existing spaceplate concepts

Many different spaceplate concepts were proposed and some demonstrated in literature, which are listed in this section.

1.2.1. Simple homogeneous low index slab

A straightforward initial approach to realizing a spaceplate is to consider using a single slab of material with a refractive index lower than the background medium. Due to Snell's law, a slab like this would displace an incoming beam a certain distance, depending on the incoming angle. Snell's law is a consequence of the change of the speed of light between different media, and is formulated as follows:

$$n_1 \sin\theta_1 = n_2 \sin\theta_2 = n_3 \sin\theta_3 \tag{1.7}$$

Assuming $n_1 = n_3 = n_{background}$ this would result in a lateral displacement that mimics the expected displacement due to propagation while keeping the angle of propagation before and after the slab the same. This can be seen in figure 1.2.

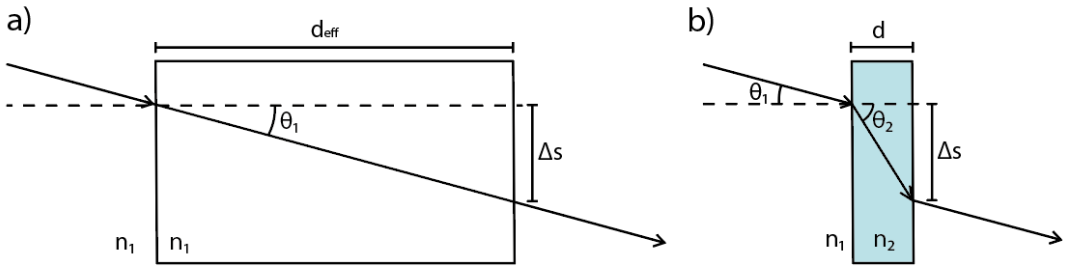

Figure 1.2: a) A lateral displacement due to propagating d_{eff} of free space. b) This can be recreated with a low-index slab of thickness d.

When trying to make a spaceplate this way, it is possible to define R using geometric relationships. If it turns out that R is a constant value regardless of incoming angle, then this indicates the material could be used as a spaceplate. Taking the lateral displacement after propagation as Δs:

$$\Delta s = d\tan\theta_2 = d_{eff}\tan\theta_1 \tag{1.8}$$

$$R = \frac{d_{eff}}{d} = \frac{\tan\theta_2}{\tan\theta_1} \tag{1.9}$$

Then by redefining these terms, one can come to R dependent on θ_1:

$$\tan\theta_1 = \frac{\sin\theta_1}{\sqrt{1-\sin^2\theta_1}} \tag{1.10}$$

$$\tan\theta_2 = \frac{\frac{n_1}{n_2}\sin\theta_1}{\sqrt{1-(\frac{n_1}{n_2}\sin\theta_1)^2}} \tag{1.11}$$

$$R = \frac{\frac{n_1}{n_2}\sqrt{1-\sin^2\theta_1}}{\sqrt{1-\left(\frac{n_1}{n_2}\sin\theta_1\right)^2}} \tag{1.12}$$

The second order Taylor expansion of R around $\theta_1 = 0$ will yield:

$$R = \frac{n_1}{n_2}\left(1 + \frac{(\frac{n_1}{n_2})^2 - 1}{2}\theta_1^2\right) + \mathcal{O}[\theta_1^4] \tag{1.13}$$

With θ_1 in radians. This shows that a simple homogeneous slab is not an ideal spaceplate, since this expression for R exponentially increases when the incoming angle increases instead of being constant

for any incoming angle. For very small angles (e.g. very close to $\theta_1 = 0$) it can approach the response of a spaceplate. This range gets bigger the closer n_2 approaches n_1, but doing this simultaneously makes $R(\theta_1 \approx 0) \approx \frac{n_1}{n_2}$ approach 1, making it less and less useful.

By expressing a maximum deviation away from $R(0)$ as $p = \frac{R(\theta_1)-R(0)}{R(0)}$ one can describe the angular range at which this works as follows:

$$\theta_1 \leq \sqrt{\frac{2p}{(\frac{n_1}{n_2})^2 - 1}} \tag{1.14}$$

Out of this can be concluded that this type of spaceplate is possible and may be useful for applications with a very small numerical aperture (NA). However, since materials with a refractive index lower than that of vacuum are not widely available, this solution is impractical for in-air or in-vacuum applications. This also does not take into account transmission intensity, which may also limit the usefulness of this concept.

1.2.2. Fabry-Pérot cavities

A simple way to create a spaceplate would be by using a series of identical Fabry-Pérot cavities (Chen and Monticone, 2021, Mrnka et al., 2022), as shown in figure 1.3. Shown here are the end results of lengthier derivations, which can be found in appendix B. Ideally, this type of design could result in systems such as that in figure 1.3 (a), where the whole optical system between lens and detector is a single monolithic structure.

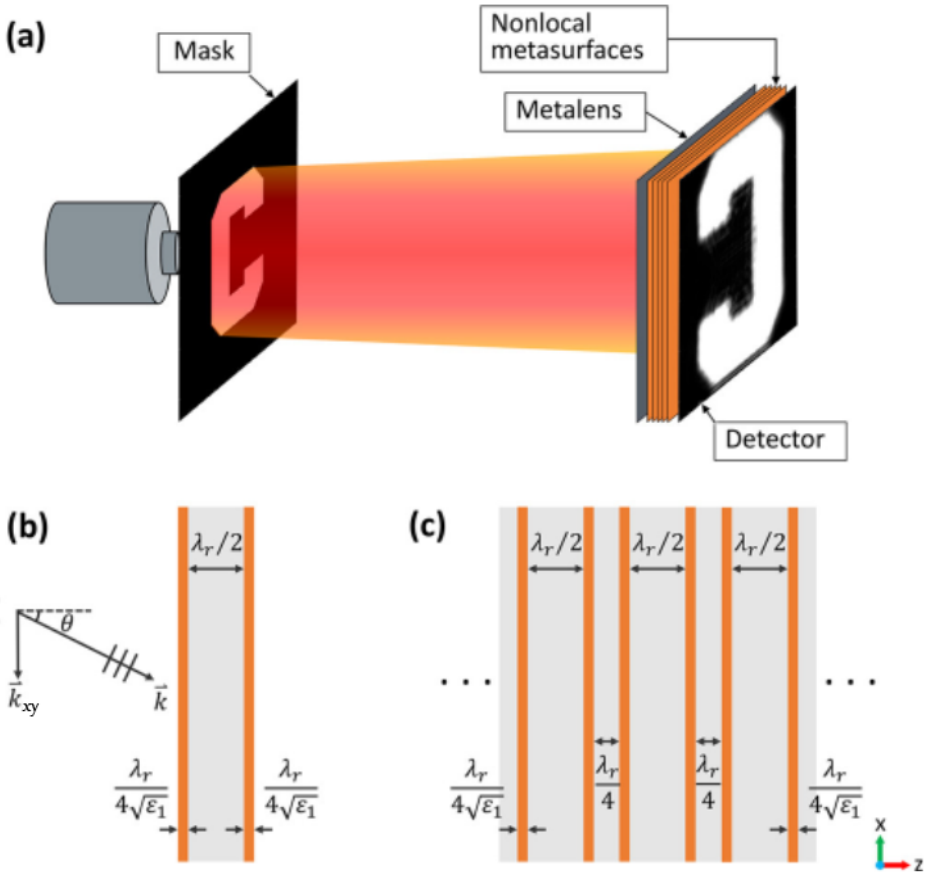

Figure 1.3: a) An ultrathin, solidstate imaging system realizable with spaceplates. b) A single dielectric resonance structure with ε_1 a high relative permittivity and ε of grey areas near unity. In this λ_r is wavelength of resonance frequency ω_r of the first even Fabry-Pérot-like resonance of the structure. c) Structure of n individual resonators which can function as a spaceplate. Figure adapted from Chen and Monticone, 2021.

Assuming $\omega \approx \omega_r$, the complex transmission phase of a single resonator as seen in figure 1.3 (b) is:

$$\varphi_t = \arctan(\frac{\omega - \omega_r}{\gamma_0}) \approx \frac{\omega - \omega_r}{\gamma_0} + \mathcal{O}\left[\left(\frac{\omega - \omega_r}{\gamma_0}\right)^3\right] \tag{1.15}$$

Where ω is the angular frequency of incoming light, ω_r is the resonant frequency of the structure and γ_0:

$$\gamma_0 = \frac{2\varepsilon_1\omega_r}{\pi(\varepsilon_1 - 1)(1 + \sqrt{\varepsilon_1} + \varepsilon_1)} = \frac{\omega_r}{2Q} \tag{1.16}$$

With ε_1 being the dielectric constant of the dielectric mirrors and Q being the quality factor of the resonator. Since the component of the wavevector along the propagation direction varies with angle, different incident angles result in differing effective resonance frequencies meaning the structure will impart a different phase depending on incoming angle.

The non-global phase change this can impart is between $-\pi/2$ and $\pi/2$, which is not enough to achieve significant compression of large effective distances. However, by stacking them into a structure as in figure 1.3c, the phases add up to useful values, namely a total phase variation of $n\pi$. The total phase for a stack is:

$$\varphi_t \approx \arctan\left(n \cdot \frac{\omega - \omega_r}{\gamma_0}\right) = n \cdot \frac{\omega - \omega_r}{\gamma_0} + \mathcal{O}\left[\left(n \cdot \frac{\omega - \omega_r}{\gamma_0}\right)^3\right] \tag{1.17}$$

In this phase the contributions of the layers between the structures (gray layers with thickness $\frac{\lambda_r}{4}$ are assumed to only add a global phase independent of incoming angle. In truth, their added phase is nonzero, but a much smaller contribution than that of the designed structures.

To relate this directly to incoming angle, one needs a relation of φ_t to k_{tv}. This can be achieved by assuming small angles, meaning k_{tv} is assumed to be small enough not to influence the field profile within the thin dielectric plates, having their individual reflection coefficients within those remain approximately real. This implies that the resonant frequency $\omega(k_{tv})$is only dependent on the length of space between dielectric mirrors, and the dispersion relation can be calculated based only on the required optical path length for constructive interference. This formula represents the shift in the resonance frequency depending on the difference in transverse momentum, which signifies the incoming angle of the light:

$$\sqrt{\omega^2(k_{tv})\mu_0\varepsilon_0 - k_{tv}^2} = 2\pi/\lambda_r = \frac{\omega_r}{c} \tag{1.18}$$

Rewriting this and using a Taylor expansion around $k_{tv} = 0$ (small angles):

$$\omega(k_{tv}) = c\sqrt{\omega_r^2/c^2 + k_{tv}^2} = \omega_r + \beta k_{tv} + \mathcal{O}[k_{tv}^4] \tag{1.19}$$

Where:

$$\beta = \frac{c^2}{2\omega_r} \tag{1.20}$$

Using equations 1.16, 1.17, 1.19 and 1.20 together and substituting them in equation 1.6 one can come to the formula for the effective distance of an n-layered spaceplate:

$$d_{eff} = n\frac{2\beta k_0}{\gamma_0} \approx n\frac{c}{\gamma_0} = n\frac{\lambda_r(\varepsilon_1 - 1)\left(1 + \sqrt{\varepsilon_1} + \varepsilon_1\right)}{4\varepsilon_1} \tag{1.21}$$

Mrnka et al., 2022 expands on this by naming a limit for the numerical aperture of such a spaceplate, which is based on the angular range where the spaceplate transmits $\geq 50\%$ of incoming power and the bandwidth that must be satisfied to remain close to resonance. It also assumes the reflection intensity to be independent from frequency and incoming angle. This results in the limit:

$$NA \leq \sqrt{1 - \frac{1}{(1 + \frac{1}{2Rl})^2}} \tag{1.22}$$

In which $R = d_{eff}/d_{actual}$ and l is the order of resonance (1, 2, 3 ...).

1.2.3. Multilayer thin film stack

The paper that initially proposed spaceplates introduced multiple possible ways of achieving them. One of these was a multilayer stack comprising different layers with different (sub-wavelength) thicknesses and refractive indices that together would effectively form many coupled cavities with different resonances, allowing more complex interference behavior. This is a more general form of a thin film spaceplate, whereas the method described in 1.2.2 specifically uses a single resonance toward which the periodic structure is tailored. Such a structure can be designed by using a transfer matrix method (as discussed in subsection 2.1) to calculate its complex transmission and then optimizing for targeted parameters, for instance by using gradient descent optimization. This method was further explored in J. T. R. Pagé et al., 2022, where theoretical spaceplates were achieved with a maximum R of 340 at an NA of 0.017, and an R of 15 at an NA of 0.087. The paper showed numerically that there exists a trade-off between numerical aperture and compression factor, and that the additional gain in compression gotten by adding degrees of freedom past 17 layers starts to plateau quickly.

The result of an optimization using the previously mentioned algorithm can be seen in figure 1.4. This particular one was optimized for operation on p-polarized light with an R of 19.7 and a maximum θ of 5, and had a final thickness after optimization of 2.38 μm, leading to an effective distance of 47 μm.

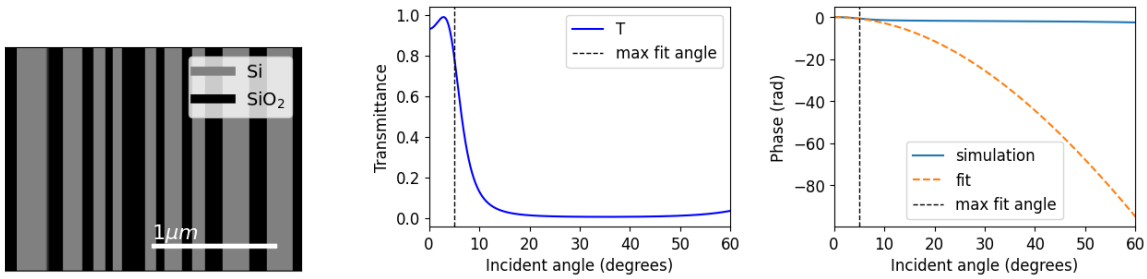

(a) Structure of the spaceplate

(b) Transmission intensity dependent on angle for p-polarized light

(c) Non-global imparted phase dependent on angle for p-polarized light

Figure 1.4: A structure generated using the code that was made publicly available at J. Pagé and Reshef, 2021 with R = 19.7, maximum angle 5 degree and 31 layers.

Interestingly, this also shows a possibility of using this type of structure to selectively transmit only a certain range of incoming angles. By adding an extra step in the optimization, one could shape the transmission profile in a way that only desired angles are let through. Using periodic thin film structures for angular stray light filtering has been done before, as discussed in section 1.5.

This type of spaceplate design using multilayer thin film layers is the one further investigated in this thesis. The particular behavior for angular stray light filtering is further investigated in section 3.4.

1.2.4. Birefringent material

The initial spaceplate proposal by (Reshef et al., 2021) also included an experimental demonstration using a uniaxial birefringent material which has an angle-dependent refractive index. A birefringent material has an anisotropic refractive index, meaning that the refractive index of the material is different along different directions. This means that depending on both polarization and incoming angle, light will experience a different refractive index. Since a spaceplate needs such an angular dependence to work, it is an apparent candidate for them.

Before finding birefringent materials as a possible solution, the condition for spaceplates needs to be rewritten as is shown below here. Firstly, one can define a refractive index ratio:

$$\tilde{n} = \tilde{n}(\theta_{SP}) = n(\theta_{SP})/n_{BG} \tag{1.23}$$

With SP signifying the property within the spaceplate itself and BG the property in background medium. In this case for instance, θ_{SP} is the angle away from the z-axis of the k-vector within the spaceplate.

Then using geometry and the continuity constraint of k_{tv}:

$$k_z^{(BG)} = k_{BG}\sqrt{1 - \tilde{n}^2 \sin^2 \theta_{SP}} \tag{1.24}$$

The required imparted phase by the spaceplate in distance d is the phase expected in background medium plus an irrelevant global phase (φ_G). In this phase, intervals of 2π for different incoming angles are physically irrelevant. Knowing this:

$$2\pi m = \varphi_{SP} - \varphi_{BG} - \varphi_G = k_z^{(SP)} d - k_z^{(BG)} d_{eff} - \varphi_G \tag{1.25}$$

Where m is an integer.

Combining these equations results in:

$$2\pi m = k_{BG} d\tilde{n} \cos \theta_{SP} - k_{BG} d_{eff}\sqrt{1 - \tilde{n}^2 \sin^2 \theta_{SP}} - \varphi_G \tag{1.26}$$

One can then isolate the phase offsets in a single parameter C:

$$C \equiv \left(m + \frac{\varphi_G}{2\pi}\right)\frac{\lambda}{n_{BG} d} = \tilde{n} \cos \theta_{SP} - \frac{d_{eff}}{d}\sqrt{1 - \tilde{n}^2 \sin^2 \theta_{SP}} \tag{1.27}$$

Then using $R = d_{eff}/d$ it becomes possible to define $\tilde{n}$:

$$\tilde{n}(\theta_{SP}) = \frac{n(\theta_{SP})}{n_{BG}} = \frac{C \pm \sqrt{C^2 + (R^2 - C^2)(1 + R^2 \tan^2 \theta_{SP})}}{(1 + R^2 \tan^2 \theta_{SP}) \cos \theta_{SP}} \tag{1.28}$$

In this, C is a parameter dependent only on the angle inside the spaceplate. This can be expressed in the integer m as such:

$$C(\theta_{SP}) = \frac{2\pi m(\theta_{SP}) + \varphi_G}{k_{BG} d} \tag{1.29}$$

C signifies the ratio of the total phase offset to the phase that would be accumulated normally in the background medium over distance d. It is an arbitrary number, meaning that equation 1.28 can have an infinite number of solutions, and so it covers an infinite collection of possible spaceplates.

By then taking C = 0, Reshef et al., 2021 was able to come to:

$$\frac{1}{n^2(\theta_{SP})} = \frac{\cos^2 \theta_{SP}}{n_{BG}^2 R^2} + \frac{\sin^2 \theta_{SP}}{n_{BG}^2} \tag{1.30}$$

For an extraordinary ray through a negative uniaxial birefringent material with $n_o > n_e$ with its extraordinary axis along the z-axis, the refractive index for an extraordinary ray is:

$$\frac{1}{n^2(\theta_{SP})} = \frac{\cos^2 \theta_{SP}}{n_o^2} + \frac{\sin^2 \theta_{SP}}{n_e^2} \tag{1.31}$$

This equation can be found by solving Maxwell's equations for anisotropic media and applying the correct boundary conditions as detailed in Jones, 2018.

So by finding a negative uniaxial birefringent material with an extraordinary refractive index equal to n_{BG} and aligning it correctly, one can get a spaceplate that works for all incoming angles and has an R equal to n_o/n_e for any extraordinary ray. Since C=0 in this case, it also means that the global phase offset should be zero, meaning it could potentially be used to compress space within interferometers as well.

Notably, this does require the incoming fields to have an extraordinary polarization, which in this context means this only works for p-polarized light as it is shown in figure 1.5. If s-polarized light is used instead, then the angular dependence of the refractive index completely falls away and the spaceplate will function as a medium with index n_o would do. This happens since the birefringent properties of the

material are caused by a directional property of electrons in the material, and so the electric field must have a component oscillating in that direction.

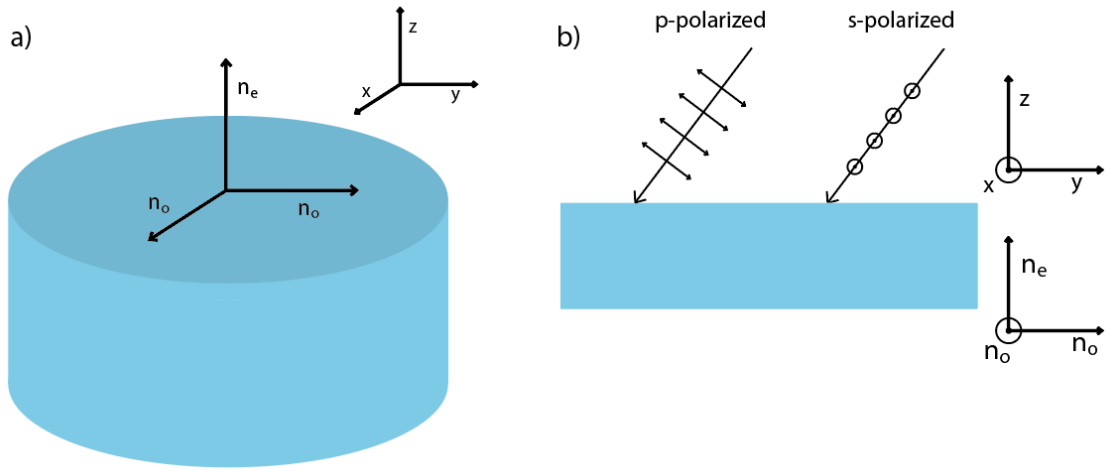

Figure 1.5: **a** A uniaxial birefringent material with its extraordinary axis parallel to z. **b** Incident p-polarized and s-polarized rays onto the uniaxial birefringent material.

Unfortunately, naturally occurring birefringent crystals have $n_e > 1$ and so a background medium other than air is needed for them to work as spaceplates. The paper Reshef et al., 2021 found and experimentally proved a working material, calcite ($n_e = 1.486$, that needed linseed oil ($n = 1.48$) as its background material to function and had $R = 1.12$. Without the development of novel birefringent materials with tailored refractive indices, this approach is currently impractical for use in air or vacuum.

It may be possible to find other materials that fulfill the requirements of equation 1.28 for a differently chosen C, though it is currently unclear which.

1.2.5. Photonic crystals

Previous concepts all used structures which were transversely invariant, meaning they only consisted of layers of material that had no geometry in the plane perpendicular to the optical axis. Such structures can be used, in photonic metamaterials, which have structures with sub-wavelength sized features in this plane. In the case of spaceplates, photonic crystals, which have a repeating feature pattern across the plane, can be used to manipulate the transmitted phase profile. A spaceplate was proposed in Guo et al., 2020 which relied on Fano resonances in a photonic crystal to shape the phase profile of transmitted light. Fano resonance occurs through interference of two coupled resonant modes and results in an asymmetric transmission profile depending on input frequency. This input frequency relates to wavelength and incoming angle, since it is the frequency in a certain direction, defined by the crystal lattice (meaning it has a dependency on k_{tv}). Such a crystal has sub-wavelength structures fabricated on or in its surface (as seen in figure 1.6), which form these resonances, allowing them to shape the phase profile of transmitted light. Additionally, these structures can be designed to have a very high transmission intensity around the intended frequency range and have a large design freedom making them ideal for designing spaceplates for many different applications.

The approach of Guo et al., 2020 demonstrated promising performance, with a maximum found R of 144 for an NA of 0.01, and an R of 11.2 for an NA of approximately 0.11.

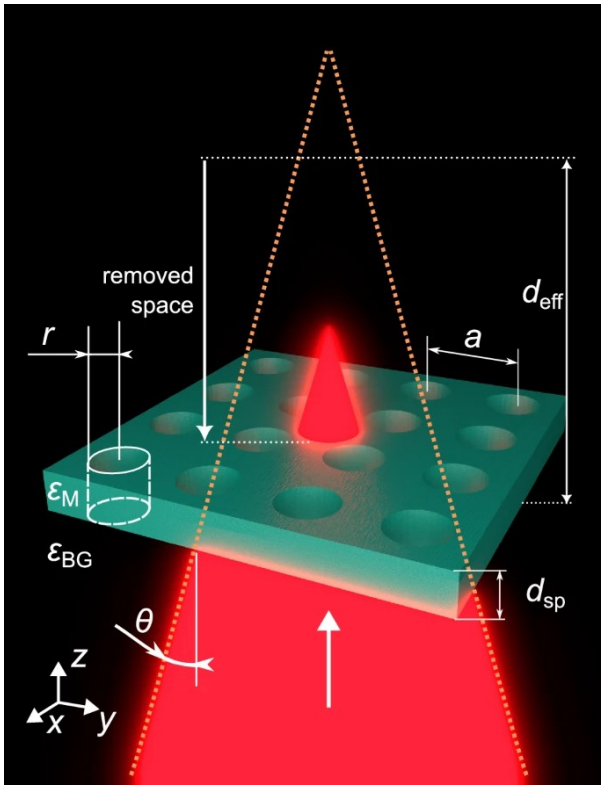

Figure 1.6: A photonic crystal functioning as a spaceplate. Figure adapted from Díaz-Fernández et al., 2024.

A more recent study of using photonic crystals to achieve spaceplate functionality was Díaz-Fernández et al., 2024. The designs in this paper make use of the fact that light has both even and odd resonance frequencies, both of which can be used separately to influence the phase of transmitted light through a photonic crystal. By having the two structures integrated in the same geometry (even electric and odd magnetic symmetry), double the compression factor of a single resonance spaceplate can theoretically be achieved. By then also applying the Huygens' condition (Pfeiffer and Grbic, 2013), a transmission intensity approaching 1 (meaning 100% power is transmitted) can be attained. For this reason, they are referred to as Huygens' spaceplates. The possibility of doubling the compression factor can be seen in the following formula for complex transmission phase through such a spaceplate (Díaz-Fernández et al., 2024):

$$\arg[t_{SP}(\omega, k_{tv})] \approx \arg[t_{SP}(\Omega_{0,1}, \Omega_{0,2})] + k_{tv}^2\left(\frac{\alpha_1}{\gamma_1 + \gamma_1\Omega_{0,1}^2} + \frac{\alpha_2}{\gamma_2 + \gamma_2\Omega_{0,2}^2}\right) \tag{1.32}$$

Wherein $\arg[t_{SP}(\Omega_{0,1}, \Omega_{0,2})]$ represents a global phase, $\Omega_{0,1}$ and $\Omega_{0,2}$ represent the frequency detuning factors for the normal incidence as $\Omega_{0,1} = \frac{\omega - \omega_1(0)}{\gamma_1}$ and $\Omega_{0,2} = \frac{\omega - \omega_2(0)}{\gamma_2}$ and α_1 and α_2 represent the frequency dispersion of each resonance at small incidence angles as $\omega_1(k_{tv}) \approx \omega_1(0) + \alpha_1 k_{tv}^2$. Frequency itself in later figures is represented using:

$$\Omega_i = \frac{\omega - \omega_i(k_{tv})}{\gamma_i} \tag{1.33}$$

Each resonance, 1 and 2 (even and odd), has its own added phase dependent on some parameters, whereas the formula for $\arg[t_{SP}]$ of a single resonance structure is the same but with one less resonance. This implies that by including both resonances in one geometry, their effects can be added without added thickness. This was also shown numerically, as presented in figure 1.7. In this figure, the orange line represents compression depending on wavelength, where $\Phi = \frac{\alpha_1}{\gamma_1 + \gamma_1\Omega_{0,1}^2} + \frac{\alpha_2}{\gamma_2 + \gamma_2\Omega_{0,2}^2}$.

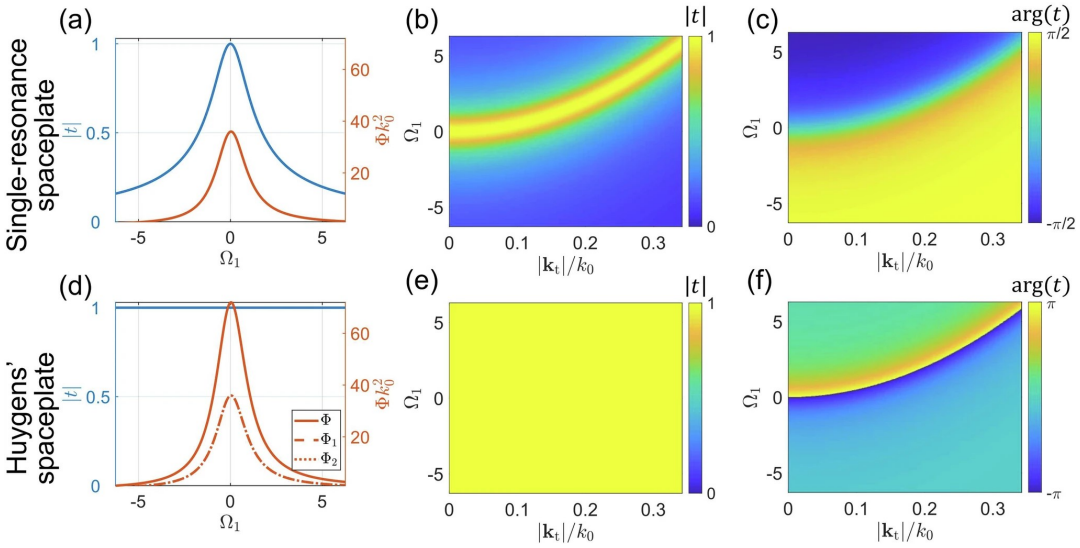

Figure 1.7: (a) Transmission coefficient amplitude at normal incidence and compression parameter versus frequency for a spaceplate with single even (electric) resonance. Parameters of the resonance are $\gamma_1 = 0.032\omega_1$, $\alpha_1 = 1.15c^2/\omega_1$, and $t_d = 0.01$. (b, c) Complex transmission coefficient for different frequencies and angles of incidence. (d-f) Same for a Huygens' spaceplate with $\omega_2 = \omega_1$, $\gamma_2 = \gamma_1$, $\alpha_2 = \alpha_1$, and $t_d = 1$. This figure was adapted from Díaz-Fernández et al., 2024.

Furthermore, by tuning the even and odd resonances for slightly different frequencies, one can make the structure have almost exactly the same phase response for a band of wavelengths between the two resonance frequencies. This means that it opens up possibilities of broadband structures that are better at retaining good compression factors and numerical aperture than their single-frequency counterparts. This was also numerically demonstrated as seen in figure 1.8.

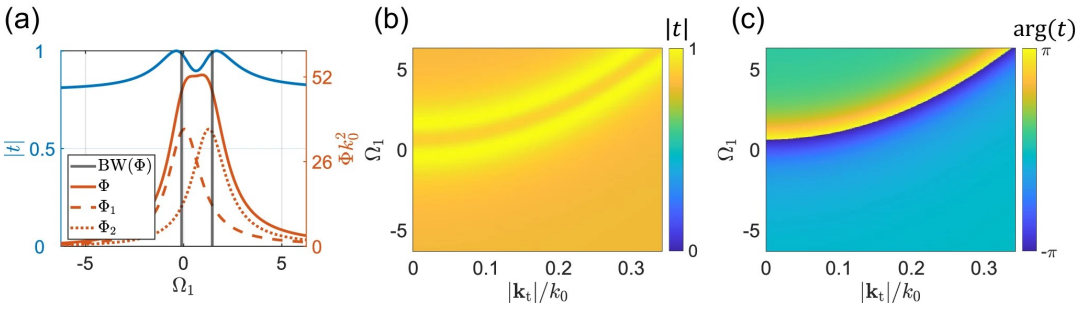

Figure 1.8: (a) Transmission coefficient at normal incidence (blue) and compression parameter (red) for the spaceplate slightly detuned from the Huygens' condition. The two resonances are separated by $\omega_2 - \omega_1 = \Delta\omega = 4\gamma/\pi$, with $\gamma_1 = \gamma_2 = 0.032\omega_1$, $t_d = 0.8$, and $\alpha_1 = \alpha_2 = 1.15c^2/\omega_1$. Within the frequency region between the two vertical black lines, the spaceplate shows a near constant compression. (b, c) Complex transmission coefficient for different frequencies and angles of incidence. This figure was adapted from Díaz-Fernández et al., 2024.

A student of Diaz-Fernández published a thesis (Wei, 2024) looking into further optimization of these structures using rigorous coupled-wave analysis, managing to attain a structure with an R of 5.17 with NA of 0.29 .

The amount of transmission intensity that these kinds of spaceplate allows seem promising, since it would allow multiple of the devices to be combined for a larger propagation distance reduction. However, since the actual spaceplate thickness is also usually smaller than a single wavelength, the amount of stacking required to reach effective distances on a centimeter scale is enormous, and might still lower the performance a considerable amount. It also makes the fabrication process of a spaceplate for effective distances above a millimeter exceedingly challenging. Comparing this to thin film spaceplates, the technology needed to achieve stacking of the photonic crystal spaceplates is way less feasible due to the added geometry fabrication steps.

Due to the complexity of these structures and limited time, this thesis will not further investigate design of a spaceplate using these photonic crystals with geometry in the transverse plane.

1.2.6. Three-lens system

For much larger devices, Sorensen et al., 2023 proposed a type of spaceplate consisting of three (thin) lenses, which is able to do optical compression on a larger scale. This system is shown here in figure 1.9.

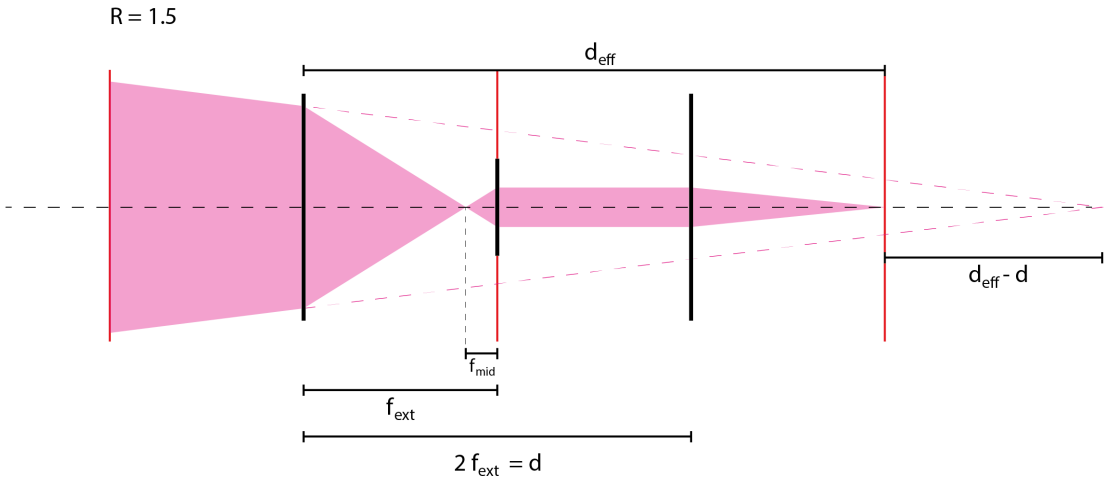

Figure 1.9: Three lenses (black) that together form a spaceplate. Focal planes of external lenses shown in red. Different situations of incoming light are shown in appendix C.

To understand it, it is important to understand the Fourier optics of lenses. It is known that an ideal positive lens performs a Fourier transform between its two focal planes, depending on spatial frequency, which in this context relates to the incoming angle of the light. By placing two identical lenses a distance of $2f$ away from each other, f being their focal distance, one gets a "4f system". This is a system where the input field at the focal plane before the first lens gets a Fourier transform onto the plane at the focal plane after the first and before the second lens, after which it once again experiences a Fourier transform onto the focal plane after the second lens. This effectively reproduces the electric field of the focal plane before the first lens, but mirrored about the optical axis and displaced by a distance of $4f$. These systems also exist with lenses of different focal lengths, but that would introduce unwanted magnification in this case. Technically speaking, this system alone would be a spaceplate with $R = 0$, since it has an effective distance of zero with a thickness of $4f$.

To make this system into a useful spaceplate, it needs to manipulate the phase of the incoming waves depending on their incoming angle. Since this is exactly the property which is projected onto the plane between the two lenses, known as the Fourier plane, one can place a spatially varying phase mask at this location to properly shape the phase profile. Since it will become clear this is also a lens, the focal distance of the two lenses that provide the Fourier plane will be called the external focal distance f_{ext} and that of the middle lens will be f_{mid}.

To derive the properties of the required phase mask, first the small-angles approximation is used to redefine the required phase. The phase from free space propagation over a distance z_0 for small angles is as follows:

$$\varphi_{SP} = z_0 k_0 \cos\theta \approx z_0 k_0 (1 - \frac{\theta^2}{2}) \approx z_0 k_0 (1 - \frac{k_{tv}^2}{2k_0^2}) \tag{1.34}$$

In this, z_0 is taken instead of d_{eff} since it does not signify the effectively propagated distance between the outer two lenses, but instead between the ends of the 4f system, meaning $d_{eff} = z_0 - 2f_{ext}$.

Then taking only the part of the required phase shift that is dependent on the transverse momentum (non-global phase), it leaves a required imparted phase:

$$\varphi_{SP} = -z_0 \frac{k_{tv}^2}{2k_0} \tag{1.35}$$

Once again making use of the small angle approximation, one can relate k_{tv} to r (distance from

optical axis at the Fourier plane) and f_{ext} for this system by combining equations 1.36 and 1.37 to come to equation 1.38:

$$r = f_{ext} \tan\theta \approx f_{ext}\theta \tag{1.36}$$

$$k_{tv} = k_0 \sin\theta \approx \theta k_0 \tag{1.37}$$

$$k_{tv} \approx \frac{r k_0}{f_{ext}} \tag{1.38}$$

This then leads to the required imparted phase at the Fourier plane:

$$\varphi_{SP} = -\frac{z_0 k_0 r^2}{2 f_{ext}^2} \tag{1.39}$$

The phase added by an ideal thin spherical lens with a focal distance f_{mid} in the paraxial approximation is given by:

$$\varphi_{mid} = -\frac{k_0 r^2}{2 f_{mid}} \tag{1.40}$$

Equating this to equation 1.39, meaning this lens is placed on-axis in the Fourier plane, shows that the effective distance ”experienced” by the light through the total system as it is shown in figure 1.9 is:

$$z_0 = \frac{f_{ext}^2}{f_{mid}} \tag{1.41}$$

Again, note that this definition of z_0 is the experienced propagation length for the system totaling a length of $4f_{ext}$, since it includes a length of f_{ext} on each side of the external lenses to include the Fourier transforms. This defines the effective propagation distance between the outer lenses as:

$$d_{eff} = z_0 - 2f_{ext} = \frac{f_{ext}^2}{f_{mid}} - 2f_{ext} \tag{1.42}$$

Then, knowing $d = 2f_{ext}$ and $R = d_{eff}/d$ one can find R:

$$R = \frac{f_{ext}}{2f_{mid}} - 1 \tag{1.43}$$

This makes it apparent that for a system where $f_{mid} < f_{ext}/4$, R will be bigger than one, meaning these lenses replace more space than they occupy. It is also possible for this formula to become smaller than one, at which point the system will take up more space than it mimics, as demonstrated in Sorensen et al., 2023. Important to realize is that all light going through this type of spaceplate will be mirrored through the z-axis.

A key advantage of this type of spaceplate, is its ability to compress large distances while remaining relatively simple in composition. In Sorensen et al., 2023, the largest spaceplate managed to replace a distance of 4.39 meters, with the resulting image presumably remaining observable without need for highly sophisticated instrumentation. Furthermore, this system functions well for broadband light barring chromatic aberrations, and regardless of polarization. This combination of properties is unique within the spaceplate designs discussed here.

One drawback of the system is that it can be rather sensitive to longitudinal misalignment of the lenses, since it is important that the middle lens is placed exactly at a distance of f_{ext} apart from each external lens. The bigger drawback however, is that the numerical aperture is very limited due to the need for very large lens diameters:

$$NA = \begin{cases} \left(1 + 4N_1^2\right)^{-\frac{1}{2}}, & D_1 \le D_2 \le f_{mid} D_3 / \left(f_{ext} - f_{mid}\right) \\ \left[1 + 16N_2^2(1+R)^2\right]^{-\frac{1}{2}}, & D_2 \le D_1 \le f_{mid} D_3 / \left(f_{ext} - f_{mid}\right) \\ \left[1 + 4N_3^2(1+2R)^2\right]^{-\frac{1}{2}}, & D_1, D_2 \ge f_{mid} D_3 / \left(f_{ext} - f_{mid}\right). \end{cases} \tag{1.44}$$

In which $N_i = f_i/D_i$, where f_i and D_i are the respective diameter and focal length of the lenses in figure 1.9 from right to left. This numerical aperture is also assuming the field of view as drawn in the figure, meaning axial with the focus at f_{ext} away from the last lens. Should a pixel array for observation be desired, then the limits will tighten more due to different incoming angles and off-axis light needing to be included.

In most situations N_3 turns out to be the limiting factor, since it is the most physically realizable type of system. In their experiments, they managed a maximum incoming angle of about 3 degrees.

Should this factor no longer form such a problem, then NA will be limited by the Abbe Sine condition according to equation 1.45 and R could end up being limited by diffractive effects, if really pushed.

$$NA = \frac{1}{2(R+1)} \tag{1.45}$$

A last significant drawback is the fact that, due to the use of traditional lenses and propagation within the spaceplate, the current design cannot be miniaturized very far. Especially when needing large numerical apertures, the device needs quite a lot of space itself, since it needs big lenses to work. The use of metalenses may be of help with this.

An interesting possibility is integrating another type of spaceplate within the propagation space of this one, specifically in the space between lenses where the light will not travel at a high angle (in figure 1.9 between middle and right lens). Taking R_{SP} as the other type spaceplate compression and R_{3L} as that of the three lens system, it would result in a compression:

$$R_{actual} = \frac{2R_{3L}}{1 + \frac{1}{R_{SP}}} \tag{1.46}$$

As this formula shows, the furthest a single added spaceplate could increase the total compression factor is nearing a factor 2 (for which R_{SP} would need to be very large). Realistically, this means that at first glance this is not a great way to increase the compression of the system, since there are simpler ways.

1.2.7. Overview and comparison

Based on the reviewed techniques, a rough overview of their relative properties can be made. This overview is presented below in tables 1.1 and 1.2.

Type of spaceplate	**Bandwidth**	**Numerical aperture**	**Transmission intensity**
Low index slab	Large	Very small	Large
Fabry-Pérot	Very small	Moderate	Moderate to large
Multilayer stack	Small	Moderate	Moderate to large
Birefringent material	Large	Large	Large
Photonic crystals	Small	Moderate	Large
Three-lens system	Large	Small	Moderate

Table 1.1: Properties of different spaceplate techniques: bandwidth, numerical aperture, and transmission intensity

Type of spaceplate	**Effective distance scale**	**Achievable Compression Ratio**	**Polarization dependence**
Low index slab	Large	Very small	Very small
Fabry-Pérot	Small	Moderate to large	Very small
Multilayer stack	Small	Moderate to large	Moderate to large
Birefringent material	Large	Very small	Very large
Photonic crystals	Very small	Moderate to large	Moderate to large
Three-lens system	Very large	Moderate	Very small

Table 1.2: Properties of different spaceplate techniques: effective distance range, compression, and polarization dependence

In this overview, what should be kept in mind is the possibility for stacking multiple spaceplates onto each other to achieve a larger d_{eff} at the cost of a certain amount of transmission intensity and possibly aberrations or deviations from the desired phase profile, depending on the chosen method. Furthermore, it should be noted that both multilayer stacks and photonic crystals rely a lot on optimization processes, meaning their properties in this table can be somewhat tuned to suit their envisioned application. The possible bandwidth of multilayer stacks is also estimated to be higher than that of Fabry-Pérot for that exact reason, even if they are very similar in their way of functioning. The tunability also extends to polarization dependence, since a device can be optimized for both s- and p-polarization, possibly enabling the design of polarization independent spaceplates. This possibility is also highlighted in the conclusion of Guo et al., 2020.

1.3. Fundamental limits

This section discusses two fundamental limits regarding spaceplates. What should be noted, is that though they both end up forming limits for the same parameter, they depend on different variables and so could not be resolved to come to a single equation. Since both are valid, whichever limit is tighter in the given use case will be the operational bound for that use case.

1.3.1. Miller thickness limit

David A. Miller has recently established a fundamental limit on how much optical systems can physically be compressed while still theoretically being able to function in Miller, 2023, a limit henceforth called the Miller thickness limit.

Miller writes about how, in non-local optics like the spaceplate, a single input and output are not related only to each other, but an output in one location is dependent on input information from many locations, which overlaps with the input for other output locations as well. This means it displays overlapping nonlocality (ONL). These input-output channels have to relay information sideways within the optic, meaning it automatically leads to thickness (since, for true zero thickness the information would have to travel sideways instantly, i.e. faster than light).

It is specified that a device that has an array of N independent output sensors will need a number C of sideways communication channels within the optic to achieve a full image. The term independent here means that none of these sensors have overlap, meaning that their inputs can be seen as orthogonal. For a fully overlapping nonlocal imager, one can say that the amount of channels needed to image one half of the pixels, is equal to N/2. For this example, we will look at the imaging of the left half of the pixels.

By defining an aperture splitting the two halves, one can evaluate the number of sideways channels, as seen in figure 1.10. Half of the channels needed to image the left half will be coming from the same side, meaning they are not crossing the aperture in the middle. This would require $C_{RL} = N/4$ sideways communication channels from right to left. Due to the assumption that the optic is a reciprocal system (light can be sent through backward with the inverse result of the forward direction), we cannot neglect the channels needed to image from the left output side to the right input side. This means that the amount of sideways channels $C = C_{RL} + C_{LR} = N/4 + N/4 = N/2$. This result is general for 1D optical elements, meaning it applies to transversely invariant structures such as multilayer thin film spaceplates.

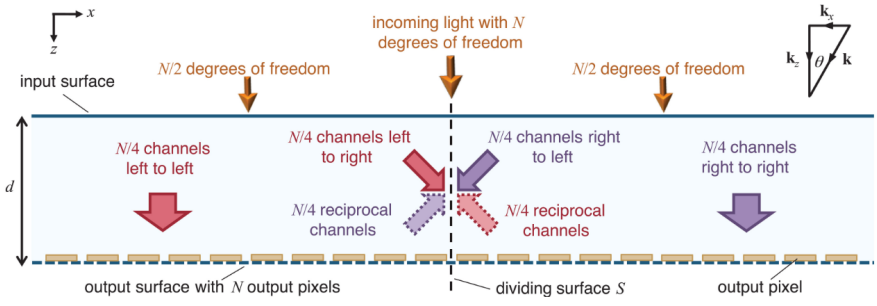

Figure 1.10: In a reciprocal ONL imager, the amount of channels crossing the dividing aperture is equal to N/2. Image adapted from Miller, 2023

For the 1D imager, diffraction heuristics say that for each separate channel a space of $\lambda_0/2n_r$ is needed, with λ_0 being the wavelength of the imaged light and n_r being the refractive index of the material between input- and output-plane. If our material is made of a range of materials, then we can say that the thickness $d \geq \frac{C\lambda_0}{2n_{max}}$. However, this is under the presumption that all angles $\pm$ 90 degrees are available for propagation, and so for conveying information through a channel. In reality, optics often make use of a limited numerical aperture meaning limited angular range $0 \leq \theta \leq \theta_{max}$, leaving only a fraction $\alpha = 1 - \cos\theta_{max} \leq 1$ available. This makes the ultimate limit for thickness of a 1D imager:

$$d \geq \frac{C\lambda_0}{2\alpha n_{max}} \tag{1.47}$$

This boundary is not something that can be passed, unless one or more of the underlying assumptions is violated by the structure of the spaceplate. Firstly, the amount of channels needed could theoretically be halved by violating the assumption of reciprocity. One could say that, if we are looking at the amount of channels needed to image one side, we should be able to neglect the number of channels going to the other side, making $C = N/4$ the total number of needed channels. This would mean it could halve the needed thickness. However, if reciprocity is assumed, then the channels in the opposite direction are needed to image this side anyways, pointing from output to input, which is why for now C is assumed to be $N/2$. While Miller discusses the possibility of violating the principle of reciprocity, no feasible implementation of this is currently known.

The possibility of using dimensional interleaving (DI) is also mentioned. This is a technique where certain degrees of freedom are reconfigured to use a different dimension, for example putting a part of N_x into N_y. It would make the whole equation into a 2D problem, and probably not gain much assuming an equal amount of degrees of freedom in both x and y. However, in situations where the observer is only present in virtually one dimension (say, a single line of pixels), this may become interesting.

For a spaceplate, knowing the Miller thickness limit also puts a bound on R, assuming a known aperture for incoming light and pixel-size of the camera/observer, in addition to the previously needed variables. Assuming an ideal system where all space between input and output of the light is occupied by the spaceplate, d_{eff} is equal to the distance that would be traveled in free space to achieve the same magnification, as seen in figure 1.11.

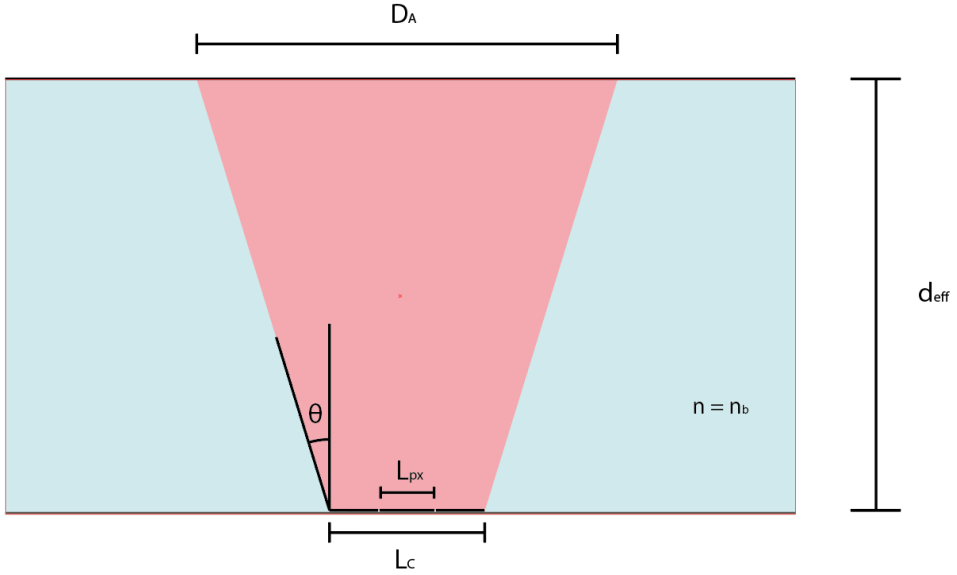

Figure 1.11: Light propagating from an input aperture to an array of pixels.

This shows that the following holds:

$$D_A = L_C + 2d_{eff}\tan\theta = L_{px}N + \frac{2\sqrt{\alpha(\alpha-2)}}{1-\alpha}d_{eff} \tag{1.48}$$

$$d_{eff} = \frac{(D_A - L_{px}N)(1-\alpha)}{2\sqrt{\alpha(\alpha-2)}} = Rd \tag{1.49}$$

Using equations 1.47 and 1.49 one can arrive at a final equation limiting the compression ratio of a transversely invariant spaceplate:

$$R_{max} \leq \frac{2\alpha n_{max}(D_A - L_{px}N)(1-\alpha)}{N\lambda_0\sqrt{\alpha(\alpha-2)}} \tag{1.50}$$

This equation shows there is a large dependency on the range of available angles α. Additionally, the number of independent outputs N has a large influence, since it prescribes the number of channels needed.

1.3.2. Bandwidth limit

The article Shastri et al., 2022 introduced a limit to the bandwidth of a spaceplate, dependent on numerical aperture and the compression ratio of that spaceplate. Investigating this fundamental limit is important to understand what is and is not possible, and to prevent futile efforts to design impossible devices.

Understanding this limit starts with defining the variables around an ideal spaceplate. The formula for the imparted phase remains the same as formula 1.6, where in figure 1.12 the other dimensions are illustrated.

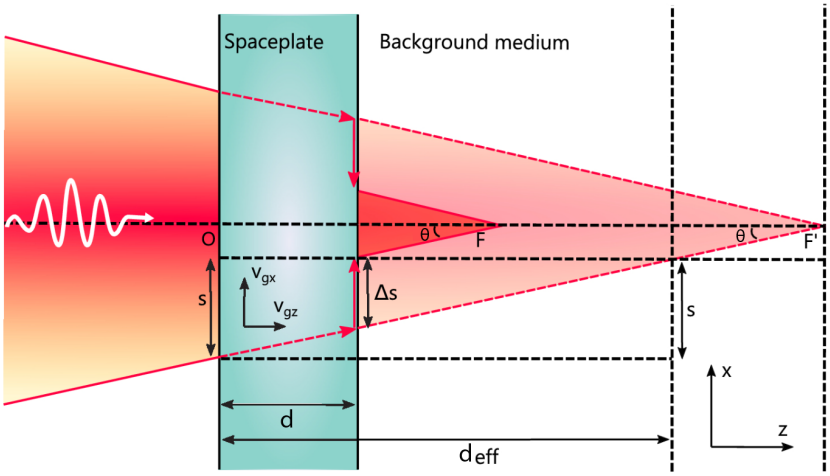

Figure 1.12: Spaceplate with parameters (figure adapted from Shastri et al., 2022).

Using a ray-optics approach, one could interpret the action of a spaceplate as moving the ray in the spaceplate-plane by a distance Δs relative to propagation in the background medium, with a direction and magnitude depending on its incoming angle. This required transversal displacement can be written as:

$$\Delta s = (d_{eff} - d)\tan(\theta) \tag{1.51}$$

It is then stated that in general, the transverse displacement s that a ray or wave experiences in a material structure can be formulated as $s = v_{gx}\tau$, where v_{gx} is the group velocity in the transverse direction and τ is the group delay imparted by the structure. One could get to the same result by varying v_{gz} instead, but the choice is made not to do so, since in the actual structure the relation between group velocities is not constant and in this approach the spaceplate is taken more as a black box. Using the previously stated definitions, one can find:

$$\Delta s = v_{gx}\tau - v_{gx}^0\tau^0 = v_{gx}\tau - c\sin(\theta)\tau^0 \tag{1.52}$$

In which $\tau^0 = d/(c\cos(\theta))$ is the time delay experienced by the wave in the background medium for length d and $c = c_0/n_b$ is wave velocity in the background medium, e.g. without the spaceplate.

From this equation, it is clear that Δs can only be increased by either increasing v_{gx} or τ to be larger than their counterpart in the background medium. Increasing v_{gx} would be possible by having a medium with a lower refractive index than the background medium, but most applications need to function in background media with low indices (air, vacuum), and so this is usually not an option. Then changing τ remains. It can be achieved by relying on resonances within the material to add a delay to the wave. By then taking $\Delta T = \tau - \tau^0$ and using equation 1.52 one can find:

$$\Delta T = \frac{\Delta s + (\sin(\theta) - v_{gx}/c)d\sec(\theta)}{v_{gx}} \tag{1.53}$$

Note that this delay becomes larger with increasing angle of incidence θ and smaller with increasing v_{gx}. For $\theta = 0$, $\Delta s = (d_{eff} - d)\tan\theta = 0$ and ΔT becomes equal to d/c, which is the exact time spent inside the spaceplate medium.

By using the definitions of $NA = n_b \sin\theta$ and $R = d_{eff}/d$ one can rewrite equation 1.53 to:

$$\Delta T = d\frac{R \cdot \mathrm{NA}/n_b - v_{gx}/c}{v_{gx}\sqrt{1 - (\mathrm{NA}/n_b)^2}} \tag{1.54}$$

Delaying light in this way for a certain bandwidth also comes with a defined limit (Miller, 2007), which for now can be written as:

$$\Delta T \Delta\omega \leq \kappa \tag{1.55}$$

Then applying equation 1.54 and defining a center frequency $\omega_c = 2\pi c/\lambda_c$ with wavelength λ_c in the background medium results in:

$$\frac{\Delta\omega}{\omega_c} \leq \frac{1}{2\pi}\frac{\kappa}{d/\lambda_c}\frac{\sqrt{1 - (\mathrm{NA}/n_b)^2}v_{gx}/c}{R \cdot \mathrm{NA}/n_b - v_{gx}/c} \tag{1.56}$$

To be able to use this formula specifically to create a bound for structures made of transversely invariant structures like multi-layer stacks, two variables, κ and v_{gx} are still difficult to fill in.

For finding the transverse group velocity v_{gx} for a multi-layer transversely invariant structure it was found in Gerken and Miller, 2005 to be approximated as follows:

$$v_{gx} \approx c_0 \sin(\theta)/n_{eff}^2 \tag{1.57}$$

In which n_{eff}^2 is a weighted average of the layers of the structure:

$$n_{eff}^2 = \frac{\sum(n_i^2 d_i/\sqrt{n_i^2 - (\sin\theta)^2})}{\sum(d_i/\sqrt{n_i^2 - (\sin\theta)^2})} \tag{1.58}$$

Wherein θ signifies the incidence angle in vacuum and i indexes the layer that is being summed.

To find a general κ, Shastri et al., 2022 derived Miller's upper bound for kappa found in Miller, 2007 but replacing the background wavenumber k_b by the longitudinal wavenumber $k_{z,b} = k_b\cos\theta$ and making the permittivity contrast factor angle-dependant: $\eta(z,\omega,\theta) = \eta(z,\omega)/(\cos\theta)^2$. Assuming the ideal spaceplate to work for both p- and s-polarization, this results in:

$$\kappa = \frac{\pi}{\sqrt{3}}\frac{d}{\lambda_c}\eta_{max}/\cos\theta \tag{1.59}$$

With $\eta_{max} = |(\epsilon_{max} - \epsilon_{min})/\epsilon_b|$ where ϵ_{min} and ϵ_{max} are the minimum and maximum permittivity for any wavelength in any point in the structure and $\epsilon_b = \sqrt{n_b}$ is the relative background permittivity. It should be noted that for a spaceplate comprised only out of a single mode resonator, κ can be presumed to be 2 (Mann et al., 2019). In Shastri et al., 2022, the limit using the modified κ of Miller is what they then call Miller's limit, not to be confused with the previously discussed Miller thickness limit.

Rewriting this limit to focus on effective distance instead will result in:

$$d_{eff} \leq \frac{d(\frac{\eta_{max}}{2\sqrt{3}} + \frac{\Delta\omega}{\omega_c})n_b^2 v_{gx}}{\frac{\Delta\omega}{\omega_c}\mathrm{NAc}_0} \tag{1.60}$$

This equation shows that to maximize d_{eff}, the permittivity contrast should be as big as possible, and having a lower numerical aperture and bandwidth allow for a larger d_{eff}. Lastly, making the plate itself thicker obviously makes d_{eff} bigger, but this can only be done so much before phase aberrations and/or transmission intensity losses become too large to tolerate. If, instead, the focus is only on the compression ratio $R = \frac{d_{eff}}{d}$:

$$R \leq \frac{(\frac{\eta_{max}}{2\sqrt{3}} + \frac{\Delta\omega}{\omega_c})n_b^2 v_{gx}}{\frac{\Delta\omega}{\omega_c}\mathrm{NAc}_0} \tag{1.61}$$

This bound should be kept in mind when optimizing or evaluating a spaceplate for multiple performance criteria.

1.4. Multifunctional thin film spaceplates

A use for spaceplates as aberration correctors for three different types of aberrations was proposed in Shao et al., 2024. The correcting behavior relies on two aspects of multilayer thin film spaceplates, which are shown in figure 1.13.

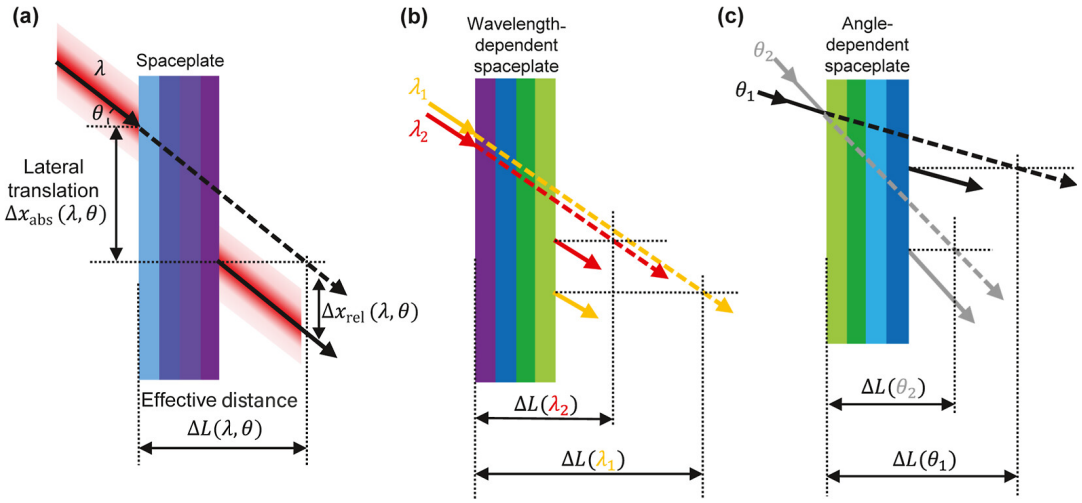

Figure 1.13: Different dependencies of a spaceplate, figure adapted from Shao et al., 2024. (a) A functioning spaceplate with an effective distance ΔL dependent on wavelength and incoming angle. (b) A spaceplate that can be used to correct chromatic aberrations by exploiting wavelength dependence of ΔL. (c) A spaceplate that can be used to correct angle dependent aberrations by altering ΔL dependent on incoming angle.

By using the dependence on the wavelength of the incoming light to change the effective distance, it is possible to correct chromatic aberrations that are introduced by a lens, if those are well known. Furthermore, since the phase profile depending on the incoming angle can be engineered using an optimization algorithm, it is possible to add an extra component to the phase profile beside the perfect phase parabola expected from traveling the effective distance. This extra component can correct for spherical aberrations and Petzval field curvature, both of which are erroneous effects caused by an unintended phase difference between an ideal phase profile and their own in the image plane, depending on the angle away from the optical axis. Shao et al., 2024 uses gradient optimization of multilayer thin film structures with both the layer thicknesses and refractive indices as free variables to design these aberration correcting spaceplates, and demonstrates their theoretical capabilities. The paper shows a theoretical design which can successfully correct chromatic aberrations between 488 nm and 658 nm at NA = 0.087, eliminating a difference in focal distance of approximately 22 μm. It is stated that this

device was designed for operation up to a NA of 0.34. It also shows a spaceplate design which can successfully correct Petzval field curvature for incoming angles into the lens up to 10 degrees, achieving a focal distance range 7 μm instead of 21 μm without the spaceplate. Lastly, a device is shown which corrects spherical aberrations of a lens, but which introduces a coma-type aberration when incoming light before the lens is angled away from the normal by 4 degrees.

This report also explores the concept of multifunctional spaceplates, though not for aberration correction. Instead, it focuses on combining the spaceplate function with angular stray light filtering. The results of this exploration can be found in section 3.5.

1.5. Angular stray light filtering using thin films

Thin film stacks can be made to create not just tailored phase profiles, but also tailored transmission intensity profiles. This fact can be used to create angular stray light filters which only transmit incoming light up to a certain incident angle relative to the optical axis at a given wavelength, as was demonstrated in Qian et al., 2017. The design of this filter relies on the concept of photonic bands and bandgaps of a periodic structure, such as the one shown in figure 1.14.

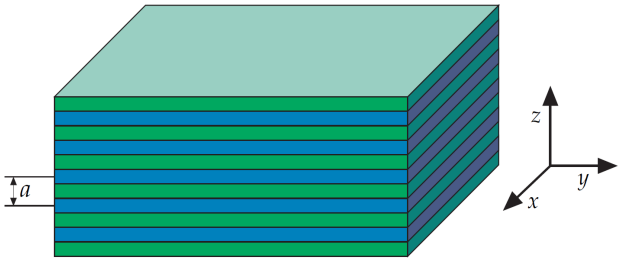

Figure 1.14: A periodic structure with a period consisting of two layers. Figure adapted from Joannopoulos et al., 2011.

An example of the resulting photonic bands can be seen in figure 1.15. In this figure, it is assumed that the incoming wave has a k-vector which lies in the zy-plane, meaning quantity k_x is assumed to be zero and k_y is therefore the only nonzero transverse wavenumber component. The ratio between k_y and $k_0 = \frac{2\pi}{\lambda}$ can therefore represent the different incoming angles.

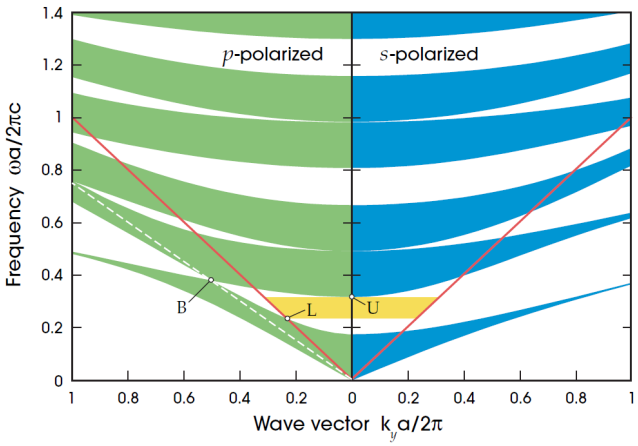

Figure 1.15: Allowed photonic bands of a quarter-wave stack with dielectric constants ε of 13 and 2, with allowed bands colored in. Incoming angles through air only exist above the straight red line, the light line ($\omega = ck_y$). The white dashed line represents the Brewster angle, causing a crossing at B. The yellow shaded region between lower edge L and upper edge U represents the range of wavelengths that will be reflected in air regardless of incoming angle. Figure adapted from Joannopoulos et al., 2011.

In a photonic band (colored in), transmission through the crystal structure is possible, and in a bandgap (white) it is not. Establishing whether a certain incoming plane wave falls inside a photonic band requires some theory, which is expanded on in appendix A. Essentially, using the transfer matrix

of a single period of a periodic structure, one can find the Bloch wavenumber K of the structure, which is further dependent on wavelength and incoming angle.

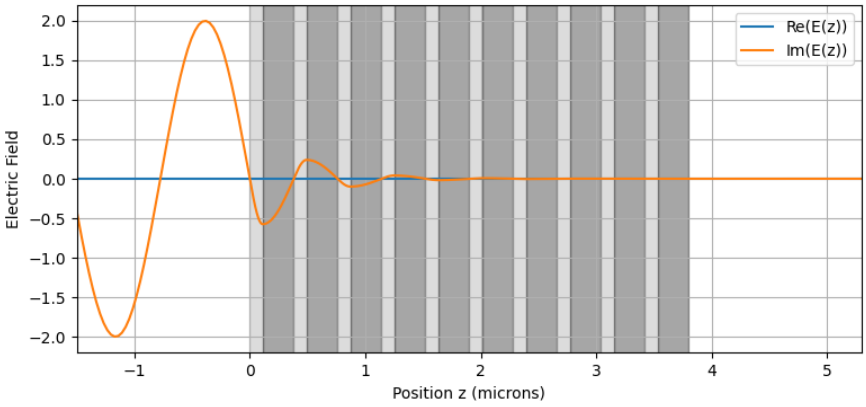

(a) Bragg mirror without defects.

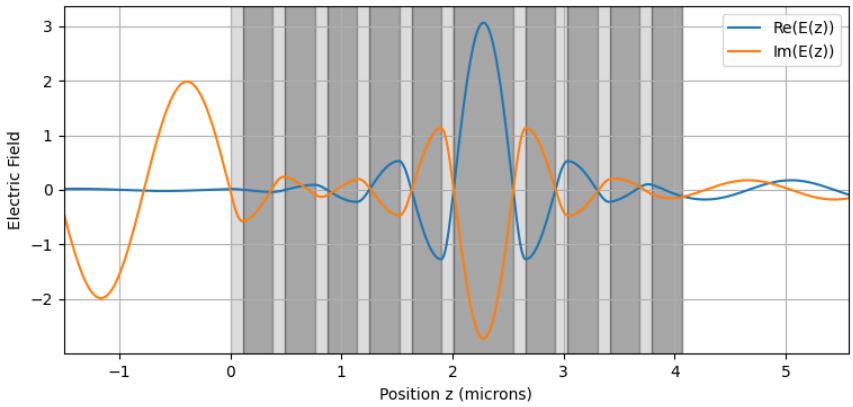

(b) Bragg mirror with single defect, being a double layer thickness.

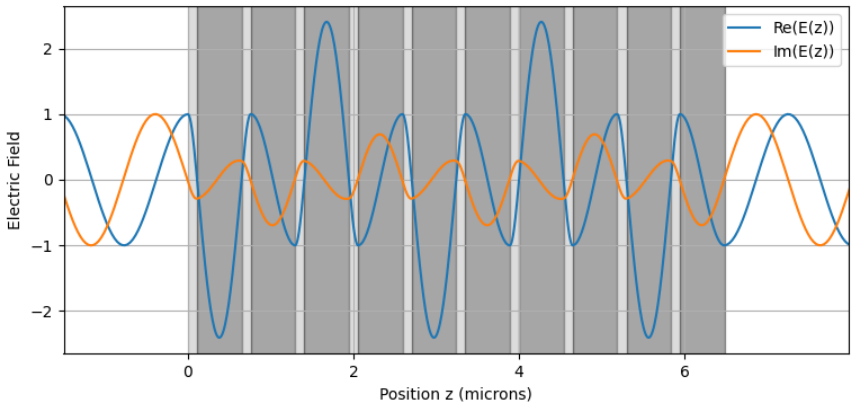

(c) Repeating structure of subsequent quarter-wave and half-wave thicknesses.

Figure 1.16: Electric field amplitude of light at normal incidence traveling through selected structures. (a) Exponentially decaying waves in a Bragg mirror with refractive indices 3.48 and 1.44 with 10 periods. (b) The result of a single defect layer with half-wave instead of quarter-wave thickness. (c) A periodic structure with alternating quarter-wave and half-wave thick layers.

When this number has an imaginary component, at that wavelength and angle there is no possible resonant state of the light wave inside the structure, and so (assuming infinite periodicity) there is

no transmission. Be aware that the resonant state meant here is not one to do with resonant states from quantum mechanics like some of those referred to in Moiseyev, 2011, but only relates to a self-sustaining electromagnetic wave inside the context of the optical cavities created by the interfaces of a multilayer structure. In the case where K is a complex value, the incoming waveform will exponentially decay inside the structure. When this occurs, this combination of wavelength and incoming angle falls within the photonic bandgap. If K is a real number, then for that wavelength and incoming angle a resonant state does exist and transmission is possible, meaning it is inside a photonic band instead. An example of this is shown in figure 1.16, where introducing a single defect in the layer thicknesses allows for a resonant state of the wave and therefore transmission through the structure. If this defect was instead part of a repeating pattern, like in figure 1.16c, one can see transmission is possible.

A numerical plot of photonic bands can be seen in figure 1.17. In this plot the y-axis label is simplified by using $\omega = 2\pi c/\lambda$. By tuning the thicknesses of two layers with different refractive indices and using that as the period of a repeating pattern in a thin film stack, one can tune the height of the horizontal blue dotted line seen in figure 1.17, thereby tuning whether light can be transmitted at certain angles or not. In this case, the result of an optimization of periodic structures which will be discussed in section 3.4.1 was used as the plotted structure, and so the cutoff of the photonic band is around an incoming angle of 5 degrees in air. In the case of Qian et al., 2017, a physical prototype was made which demonstrated transmission intensity values between 0.8 and approximately 0.18 between incoming angles of 0 and 2 degrees away from the surface normal, and transmission intensity near zero after incoming angles of approximately 6 degrees.

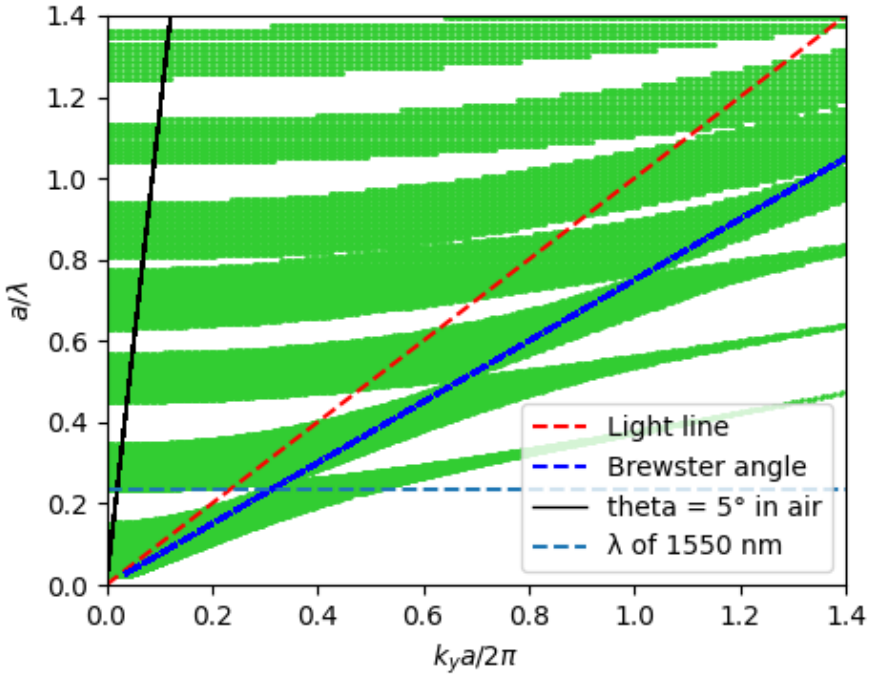

Figure 1.17: Numerical analysis of photonic bands of a structure with a period of 2 layers for p-polarized light.

The design of a stray light filter using periodic thin films does not solely depend on the photonic band structure, however. Since the photonic band graph assumes infinite periodicity, it does not show the actual transmission intensity values inside the band for a finite structure. Therefore, the methodology used in Qian et al., 2017 starts from a design which is within a transmissive band up to a couple degrees, and then involves tuning the amount of repetitions and the individual layer thicknesses of the unit cell to find a combination which has a transmission peak closest to the bandgap at the desired wavelength. Plots of these tunable variations are presented in figure 1.18.

This way, high transmission at normal incidence is guaranteed while still filtering transmission at oblique angles. However, designing this way does not seem to allow having high transmission intensity

for a range of angles, meaning it may not be optimal for applications which only want to filter out light at higher incident angles. Therefore, an exploration of non-periodic thin film structures was conducted, the results of which can be found in section 3.4.

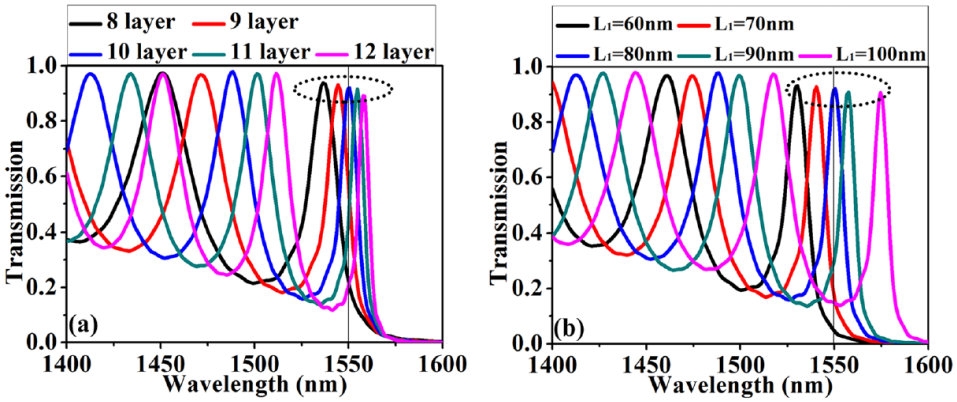

Figure 1.18: Transmission intensity spectrum of periodic angular light filter, figure adapted from Qian et al., 2017. A unit cell consists of layers L_1 and L_2 where $L_1 = 80$nm and $L_1 + L_2 = 534$nm. (a) Transmission spectrum with differing number of unit cell repetitions but same unit cell. (b) Transmission spectrum for 10 unit cell repetitions with changing unit cell thicknesses while maintaining $L_1 + L_2 = 534$nm.

2

Methods

2.1. Transfer matrix method

To calculate the intensity and phase of both transmission and reflection of multilayer thin film structures, the simplest (and generally least computationally expensive) methods are those using transfer matrices. Two different matrix formalisms were explored. They work using slightly different terms, but ultimately give the same results. The second method ended up being the method chosen for the optimization algorithm, but the first was used for validation purposes and may also be more intuitive to some, hence why it is still included here. Important to note is that all refractive indices are taken as purely real numbers, meaning absorption of light by the media is not taken into account in this thesis.

2.1.1. Fresnel-based transfer matrix method

The first of the two methods often used is one based on the Fresnel coefficients between two media with different refractive indices (Yariv and Yeh, 2007). This method relies on two types of matrices, those describing interfaces between two materials of different refractive indices, and those describing traveling a distance through a homogeneous material. First, the Fresnel equations for each interface are considered (Born and Wolf, 1999). These equations are well known in optics, and are based on the continuity conditions of electric and magnetic fields through a surface. They result in reflection and transmission coefficients of an interface:

$$t_s = \frac{2n_1 \cos\theta_1}{n_1 \cos\theta_1 + \frac{\mu_{r1}}{\mu_{r2}} n_2 \cos\theta_2} \tag{2.1}$$

$$r_s = \frac{n_1 \cos\theta_1 - \frac{\mu_{r1}}{\mu_{r2}} n_2 \cos\theta_2}{n_1 \cos\theta_1 + \frac{\mu_{r1}}{\mu_{r2}} n_2 \cos\theta_2} \tag{2.2}$$

$$t_p = \frac{2n_1 \cos\theta_1}{\frac{\mu_{r1}}{\mu_{r2}} n_2 \cos\theta_1 + n_1 \cos\theta_2} \tag{2.3}$$

$$r_p = \frac{\frac{\mu_{r1}}{\mu_{r2}} n_2 \cos\theta_1 - n_1 \cos\theta_2}{\frac{\mu_{r1}}{\mu_{r2}} n_2 \cos\theta_1 + n_1 \cos\theta_2} \tag{2.4}$$

In which s and p stand for their respective types of polarization as shown in figure 2.1, θ is the angle between surface normal and the beam and μ_i denotes the magnetic permeability of the medium. The coefficients at a single interface are real numbers as long as all refractive indices are real numbers as well, as is assumed in this thesis.

Notably, when considering the transmission and reflection coefficients from medium 1 to medium 2 (t_{12} and r_{12}) and from medium 2 to medium 1 (t_{21} and r_{21}), they satisfy the relationships:

$$t_{12}t_{21} - r_{12}r_{21} = 1 \tag{2.5}$$

$$r_{12} = -r_{21} \tag{2.6}$$

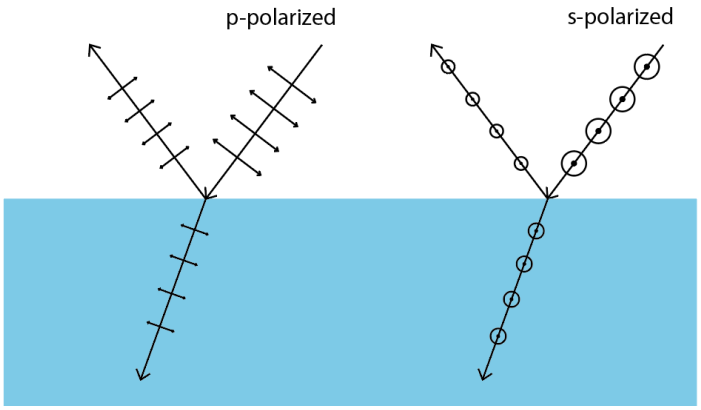

Figure 2.1: Polarization of incident light.

Using these coefficients, one can now formulate a set of equations describing the amplitudes of forward and backward traveling waves v and w respectively, on either side of the incidence plane between layers 1 and 2:

$$v_2 = v_1 t_{12} + w_2 r_{21} \tag{2.7}$$
$$w_1 = v_1 r_{12} + w_2 t_{21} \tag{2.8}$$

Applying equations 2.5 and 2.6 enables rewriting this set of equations to:

$$v_1 = \frac{1}{t_{12}} v_2 + \frac{r_{12}}{t_{12}} w_2 \tag{2.9}$$
$$w_1 = \frac{r_{12}}{t_{12}} v_2 + \frac{1}{t_{12}} w_2 \tag{2.10}$$

Generalizing these equations for layers number j and $j+1$ instead of 1 and 2 and rewriting them into a matrix form delivers the characteristic matrix F for finding the amplitudes v and w at an interface:

$$\begin{pmatrix} v_j \\ w_j \end{pmatrix} = \begin{pmatrix} 1 & r_{j,j+1} \\ r_{j,j+1} & 1 \end{pmatrix} \frac{1}{t_{j,j+1}} \begin{pmatrix} v_{j+1} \\ w_{j+1} \end{pmatrix} = F_{j,j+1} \begin{pmatrix} v_{j+1} \\ w_{j+1} \end{pmatrix} \tag{2.11}$$

Between interfaces, the forward and backward traveling waves accumulate a phase shift δ dependent on the thickness d_j and refractive index n_j of the layer, the angle inside the medium and the vacuum wavelength of the light:

$$\delta_j = \frac{2\pi}{\lambda_0} d_j \cos\theta_j \tag{2.12}$$

Where θ_j can easily been found using Snell's law and a known angle θ_0 in a known medium with refractive index n_0:

$$n_0 \sin\theta_0 = n_j \sin\theta_j \tag{2.13}$$

Knowing δ_j, one can write out the relationship between amplitudes of v and w at the start and end of layer j along the optical axis culminating in characteristic phase P:

$$\begin{pmatrix} v_{j,start} \\ w_{j,start} \end{pmatrix} = \begin{pmatrix} e^{-i\delta_j} & 0 \\ 0 & e^{i\delta_j} \end{pmatrix} \begin{pmatrix} v_{j,end} \\ w_{j,end} \end{pmatrix} = P_j \begin{pmatrix} v_{j,end} \\ w_{j,end} \end{pmatrix} \tag{2.14}$$

Consequently, this permits the formulation of forward and backward traveling waves through a multilayer structure by multiplying matrices. For instance, going from air (layer 0) through two layers (layers 1 and 2) into a substrate (layer 3), the forward and backward traveling waves at the interfaces of the two layers to their environment are:

$$\begin{pmatrix} v_0 \\ w_0 \end{pmatrix} = F_{01}P_1F_{12}P_2F_{23}\begin{pmatrix} v_3 \\ w_3 \end{pmatrix} \tag{2.15}$$

Generalizing this method for a structure with an arbitrary total of N layers, the wave amplitudes of forward and backward traveling light v and w can be found using the complete transfer matrix of the structure, $\tilde{M}$:

$$\begin{pmatrix} v_{in} \\ w_{in} \end{pmatrix} = F_{01}\prod_{j=1}^{N}(P_jF_{j,j+1})\begin{pmatrix} v_{out} \\ w_{out} \end{pmatrix} = \tilde{M}\begin{pmatrix} v_{out} \\ w_{out} \end{pmatrix} \tag{2.16}$$

From matrix $\tilde{M}$ one can then find t and r like so:

$$\begin{pmatrix} 1 \\ r \end{pmatrix} = \tilde{M}\begin{pmatrix} t \\ 0 \end{pmatrix} \tag{2.17}$$

$$r_{stack} = \frac{\tilde{M}_{10}}{\tilde{M}_{00}}, \quad t_{stack} = \frac{1}{\tilde{M}_{00}} \tag{2.18}$$

Complex transmission t holds the phase information that can be compared to the desired phase resultant of propagation through the multi-layer stack. The magnitude of the transmitted field can simply be found using the following equation:

$$T_{stack} = 1 - R_{stack} = 1 - |r_{stack}|^2 \tag{2.19}$$

Important to note, from these calculations, is that the polarization of the incoming light matters greatly for the transmitted light through a multi-layer stack, both in magnitude and phase. If the light is not linearly polarized to be either s- or p-polarized, then these polarizations will be (partially) separated unless both are optimized for simultaneously.

2.1.2. Characteristic transfer matrix method

The matrix formalism used by J. Pagé and Reshef, 2021, colloquially known as the characteristic transfer matrix method, instead does not focus on forward and backward traveling wave amplitudes, but on the electric and magnetic field magnitude at interfaces, as described in Pedrotti et al., 2017.

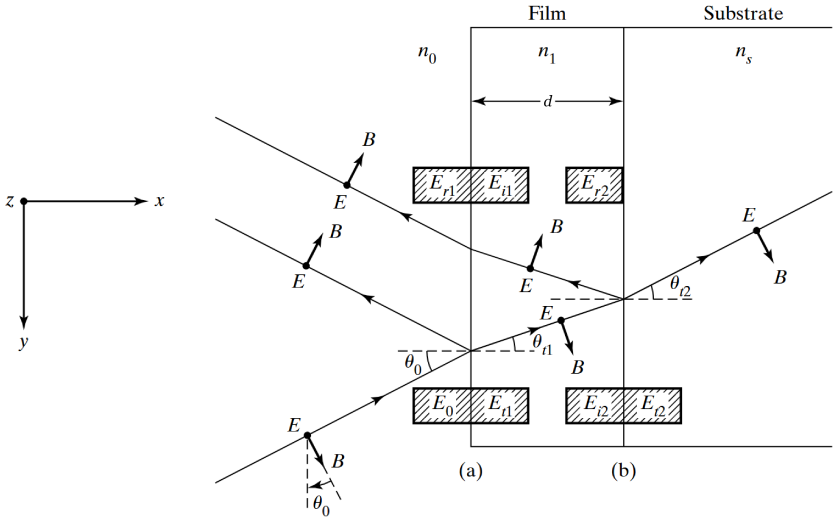

Figure 2.2: Definitions of fields traveling through a single thin film into a substrate, adapted from Pedrotti et al., 2017. Note that the resultant field of any interaction at boundary (a) will have a subscript 1 and at boundary (b) a subscript 2.

Working out the formalism can be done using the definitions given in figure 2.2. Important to realize about this figure is that the terms inset in the figure represent all light traveling in a certain direction on a side of the boundary. For instance, E_{r1} represents the light from both the reflection on the first incident

layer and transmitted light coming back out of the thin film after being reflected inside it. Furthermore, this image represents the situation for s-polarization, with the bold dots representing an electric field vector perpendicular to the xy-plane. Also notice that the y-component of **B** is flipped in the reflected wave, while the z-component of **E** is not. This is a consequence of positive sign convention for electric waves combined with the formulation of the Poynting vector, which expresses the direction of propagation of the energy of the electromagnetic plane wave, given by:

$$\mathbf{S} = \varepsilon_0 c^2 \mathbf{E} \times \mathbf{B} \tag{2.20}$$

Using the definitions from figure 2.2 and using the Maxwell's boundary conditions which state that the tangential components of the resultant **E**- and **B**-fields are continuous over the boundary between two different mediums, one can formulate the magnitude of the fields at the boundaries:

$$E_a = E_0 + E_{r1} = E_{t1} + E_{i1} \tag{2.21}$$
$$E_b = E_{r2} + E_{i2} = E_{t2} \tag{2.22}$$
$$B_a = B_0 \cos\theta_0 - B_{r1} \cos\theta_0 = B_{t1} \cos\theta_{t1} - B_{i1} \cos\theta_{t1} \tag{2.23}$$
$$B_b = B_{i2} \cos\theta_{t1} - B_{r2} \cos\theta_{t1} = B_{t2} \cos\theta_{t2} \tag{2.24}$$

One can relate the magnitudes E and B of fields **E** and **B** using:

$$B = n\sqrt{\varepsilon_0 \mu_0} E \tag{2.25}$$

Combining equations 2.23, 2.24 and 2.25 one can relate the fields:

$$B_a = \gamma_0 (E_0 - E_{r1}) = \gamma_1 (E_{t1} - E_{i1}) \tag{2.26}$$
$$B_b = \gamma_1 (E_{i2} - E_{r2}) = \gamma_s E_{t2} \tag{2.27}$$

Where γ are defined using the refractive index and angle in the respective medium:

$$\gamma_0 = n_0 \sqrt{\varepsilon_0 \mu_0} \cos\theta_0 \tag{2.28}$$
$$\gamma_1 = n_1 \sqrt{\varepsilon_0 \mu_0} \cos\theta_{t1} \tag{2.29}$$
$$\gamma_s = n_s \sqrt{\varepsilon_0 \mu_0} \cos\theta_{t2} \tag{2.30}$$

To find the relation between angles in the different mediums, one can use Snell's law:

$$n_0 \sin\theta_0 = n_1 \sin\theta_{t1} = n_s \sin\theta_{t2} \tag{2.31}$$

One can also find a relationship between the fields inside the film using their phase difference:

$$E_{i2} = E_{t1} e^{-i\delta} \tag{2.32}$$
$$E_{i1} = E_{r2} e^{-i\delta} \tag{2.33}$$

Where δ represents the accumulated phase from traveling from one side of the film to the other, defined as:

$$\delta = \frac{2\pi}{\lambda_0} n_1 d \cos\theta_{t1} \tag{2.34}$$

Revisiting boundary (b), one can now write:

$$E_b = E_{t1} e^{-i\delta} + E_{i1} e^{i\delta} = E_{t2} \tag{2.35}$$
$$B_b = \gamma_1 (E_{t1} e^{-i\delta} - E_{i1} e^{i\delta}) = \gamma_s E_{t2} \tag{2.36}$$

Which can be rewritten to:

$$E_{t1} = \frac{\gamma_1 E_b + B_b}{2\gamma_1} e^{i\delta} \tag{2.37}$$

$$E_{i1} = \frac{\gamma_1 E_b - B_b}{2\gamma_1} e^{-i\delta} \tag{2.38}$$

Then by using the Euler identities, which are as follows:

$$2\cos\delta = e^{i\delta} + e^{-i\delta} \tag{2.39}$$

$$2\sin\delta = e^{i\delta} - e^{-i\delta} \tag{2.40}$$

One can arrive at the set of equations relating the field at boundary (a) to boundary (b):

$$E_a = E_b \cos\delta + B_b \frac{i\sin\delta}{\gamma_1} \tag{2.41}$$

$$B_a = E_b(i\gamma_1 \sin\delta) + B_b \cos\delta \tag{2.42}$$

These equations can then be put into matrix form:

$$\begin{pmatrix} E_a \\ B_a \end{pmatrix} = \begin{pmatrix} \cos\delta & \frac{i\sin\delta}{\gamma_1} \\ i\gamma_1 \sin\delta & e^{i\delta_l} \end{pmatrix} \begin{pmatrix} E_b \\ B_b \end{pmatrix} = M \begin{pmatrix} E_b \\ B_b \end{pmatrix} \tag{2.43}$$

This matrix successfully relates the fields at the two boundaries, and is known as the transfer matrix of the film. If boundary (b) is actually the start of a second film, this transfer matrix is still valid. Furthermore, the formula can be used directly to find the transfer matrix of this second film by filling in the correct parameters. For an arbitrary number of layers, just as formula 2.16 in the previous section, all transfer matrices can be multiplied to find the total transfer matrix:

$$\begin{pmatrix} E_a \\ B_a \end{pmatrix} = \prod_{j=1}^{N} M_j \begin{pmatrix} E_b \\ B_b \end{pmatrix} = \tilde{M} \begin{pmatrix} E_b \\ B_b \end{pmatrix} \tag{2.44}$$

This formulation still requires some work to extract the transmission and reflection coefficients. Defining the last boundary of the stack as being boundary number N and the subsequent refractive index of the substrate as n_s, one can write:

$$E_a = E_0 + E_{r1} \tag{2.45}$$

$$E_b = E_{tN} \tag{2.46}$$

$$B_a = \gamma_0(E_0 - E_{r1}) \tag{2.47}$$

$$B_b = \gamma_s E_{tN} \tag{2.48}$$

Filling in equation 2.43 results in:

$$\begin{pmatrix} E_0 + E_{r1} \\ \gamma_0(E_0 - E_{r1}) \end{pmatrix} = \begin{pmatrix} \cos\delta & \frac{i\sin\delta}{\gamma_1} \\ i\gamma_1 \sin\delta & e^{i\delta_l} \end{pmatrix} \begin{pmatrix} E_{tN} \\ \gamma_s E_{tN} \end{pmatrix} = \begin{pmatrix} m_{11} & m_{12} \\ m_{21} & m_{22} \end{pmatrix} \begin{pmatrix} E_{tN} \\ \gamma_s E_{tN} \end{pmatrix} \tag{2.49}$$

In which m_{11}, m_{12}, m_{21} and m_{22} are the components of $\tilde{M}$ to be used for the sake of simplification from here on out. This is equivalent to the following set of equations:

$$E_0 + E_{r1} = (m_{11} + m_{12}\gamma_s)E_{tN} \tag{2.50}$$

$$\gamma_0(E_0 - E_{r1}) = (m_{21} + m_{22}\gamma_s)E_{tN} \tag{2.51}$$

The following definitions for t and r are used:

$$t = \frac{E_{tN}}{E_0} \tag{2.52}$$

$$r = \frac{E_{r1}}{E_0} \tag{2.53}$$

Using some algebra, this leads to the final expressions for t and r dependent on the total transfer matrix of the structure:

$$t = \frac{2\gamma_0}{\gamma_0 m_{11} + \gamma_0\gamma_s m_{12} + m_{21} + \gamma_s m_{22}} \tag{2.54}$$

$$\tag{2.55}$$

$$r = \frac{\gamma_0 m_{11} + \gamma_0\gamma_s m_{12} - m_{21} - \gamma_s m_{22}}{\gamma_0 m_{11} + \gamma_0\gamma_s m_{12} + m_{21} + \gamma_s m_{22}} \tag{2.56}$$

These are complex coefficients, from which the phase change introduced by the multilayer structure can be deduced, just as in the method shown in section 2.1.1. The previously derived equations were obtained using definitions of s-polarized light. For p-polarized light, one can follow the same steps, but changing the situation so that $\mathbf{E}$ is in the direction that $\mathbf{B}$ is currently in in figure 2.2, and rotating $\mathbf{B}$ accordingly so that the direction is still correct according to the definition of the Poynting vector. In this case, the cosine terms show up in the terms for the electric field instead, as that now has a component in the x-direction. Ultimately, this derivation comes down to the same transfer matrix except for a change in the definition of γ_m with m denoting the medium, where it is divided instead of multiplied by the cosine term. For clarity, both definitions are listed here:

$$\gamma_{m,\ p-pol.} = n_m \frac{\sqrt{\varepsilon_0\mu_0}}{\cos\theta_m} \tag{2.57}$$

$$\gamma_{m,\ s-pol.} = n_m \sqrt{\varepsilon_0\mu_0}\cos\theta_m \tag{2.58}$$

At normal incidence, $\cos\theta_m = \cos 0 = 1$ which results in equal outcomes for both situations, as is to be expected.

2.2. Optimization

The design of a thin film spaceplate can be done using optimization, as was demonstrated in J. T. R. Pagé et al., 2022. However, when looking at the code provided in J. Pagé and Reshef, 2021, it becomes apparent that the optimization method is rather rudimentary, and can be improved upon.

When regarding this as an optimization problem, it is one with a freedom space that has a number of dimensions equal to the amount of layers of the structure to be optimized. The thicknesses of these layers are to be changed until the optimal solution has been found. In J. T. R. Pagé et al., 2022 it is suggested that near optimal compression can be reached with 17 layers for a certain system, but since more requirements aside from high compression may be introduced, adding extra layers to extend the freedom space may be desirable.

Due to the complexity of the structure and possible added requirements, it may be assumed that this will be a highly non-convex problem, meaning many local optima will exist which are worse solutions than the global optimum. Simply starting with a gradient descent method from a random point inside this freedom space will most likely result in the algorithm converging on a local optimum. Therefore, it is wise to use a global search algorithm as an initial stage which can rule out many low-quality local optima and provide a promising region in the freedom space, after which a gradient descent method can optimize within that region to get to the nearest optimal location in the parameter space. This still may not be the actual global optimum, but guarantees better results than a gradient descent method on its own.

2.2.1. Particle swarm optimization

For a global search algorithm, particle swarm optimization is chosen (Kennedy and Eberhart, 1995, Clerc, 2012). Several others were considered, namely simulated annealing, genetic algorithms, and differential evolution. The choice for particle swarm optimization is made since it offers a relatively simple approach that allows for a lot of nuance in parameters. The other methods may still be useful, but a single global search method seems enough, as they should all converge to relatively similar results.

The chosen implementation of particle swarm optimization works as follows. First, a swarm of particles is generated, each having an initial position in the freedom space, $\mathbf{x}_p$, which is a vector containing the coordinates (layer thicknesses) in each of the corresponding n dimensions (number of layers) for particle p. They are generated using latin hypercube sampling (LHS), which is a method of sampling meant to randomly spread out samples evenly over dimensions in a multidimensional space (McKay et al., 1979). This is done using the built in function from the scipy library for python (SciPy Developers, n.d.). Each particle also gets a random velocity $\mathbf{v}_p$ in the same number of directions, with all vector components v_d of $\mathbf{v}_p = [v_1, v_2, \ldots, v_n]$ having a magnitude according to a uniform random distribution:

$$v_d \sim U(-0.5\Delta th, 0.5\Delta th) \tag{2.59}$$

Where Δth is equal to the difference between the lower and upper boundary on individual layer thickness. Let $\mathbf{s}_p$ be the best known location of the individual particle p itself and $\mathbf{g}$ be the best known location of the entire swarm of particles, then an iteration of the particle swarm optimization will consist of updating the velocity and location of each particle p inside the swarm according to the following formulas:

$$v_{p,d,new} = wv_{p,d} + c_s r_s(s_{p,d} - x_{p,d}) + c_g r_g(g_d - x_{p,d}) \tag{2.60}$$

$$\mathbf{x}_{p,new} = \mathbf{x}_p + \mathbf{v}_p \tag{2.61}$$

In which d signifies the single dimension that is updated, $r_s, r_g \sim U(0,1)$, and w, c_s and c_g are the inertia weight and the cognitive and social coefficient, respectively. The basic idea here is that any single particle will start moving in a random direction, and in each iteration ”chooses” where to go next based in part on its best known location ($\mathbf{s}$) and that of the group ($\mathbf{g}$) in combination with the initial randomly assigned velocity. Throughout the process, the inertia weight and coefficients are then changed so that, at the end, the inertial weight is low and all particles converge toward $\mathbf{g}$, which is assumed to be the global optimum. In an ideal world, the swarm will be large enough to have covered the entire freedom space and reviewed all local optima, but in reality the found solution is most likely not global in this thesis, since the search space has many dimensions and there is limited computational power. Each time the process is repeated different solutions may be found due to randomness in the process. The chosen weights for the particle swarm optimization in this study were found by finetuning them using trial and error and are as follows:

$$c_s = 1.5 \tag{2.62}$$

$$c_g = 0.2 + 1.8(j/N) \tag{2.63}$$

$$w = 0.9 - 0.4(j/N) \tag{2.64}$$

Wherein j signifies the current iteration count and N signifies the total number of iterations the process will go through, as is given at the start. Whenever a particle then crosses the boundary of a dimension (exceeding the boundary thickness for a certain layer), its velocity in that dimension is flipped by multiplying it with -1 and $x_{p,d}$ is set to be equal to the boundary that was crossed. This way, particles ”bounce off” the boundaries so that they do not lose all velocity and can still continue exploring the search space.

2.2.2. Fletcher-Reeves conjugate method

For the gradient descent algorithm, the Fletcher-Reeves conjugate gradient method is chosen (Papalambros and Wilde, 2017). This algorithm only requires first order derivative information, which leaves the amount of necessary evaluations per optimization steps relatively small whilst still being an

effective gradient descent method. Higher order methods could also work, but are considered too computationally expensive since they need more evaluations of the fitness function in different locations.

The conjugate gradient method works as follows. First, the starting position is defined as $\mathbf{x}_1$. Next, the first search direction is defined as $\mathbf{d}_1 = \nabla f(\mathbf{x}_1)$, where f is the fitness function. Since this thesis uses a figure of merit as its fitness function which increases with better solutions (section 2.2.3), the search direction is in the direction of the positive gradient of $f(\mathbf{x})$. Next, a line search is performed toward the next location in the optimization space:

$$\mathbf{x}_{j+1} = \mathbf{x}_j + \alpha_j \mathbf{d}_j \tag{2.65}$$

The line search consists simply of ”walking” in the direction $\mathbf{d}_j$ while evaluating the fitness using $f(\mathbf{x})$ and stopping at the point where increasing α_j no longer increases fitness function $f(\mathbf{x}_{j+1})$. The next search direction is then determined:

$$\mathbf{d}_{j+1} = \nabla f_{j+1} + \frac{||\nabla f_{j+1}||^2}{||\nabla f_j||^2} \tag{2.66}$$

After this step the steps in equations 2.65 and 2.66 are repeated N times, after which the next direction $\mathbf{d}_{N+1} = \nabla f(\mathbf{x}_{N+1})$, where N is equal to the number of dimensions in the search space (which is equal to the number of layers in the structure that is being optimized). This is necessary since the algorithm has worse convergence after approximately N steps.

2.2.3. Figure of merit

All of the evaluations of the fitness function of a location within the parameter space are done using a figure of merit (FOM) as the fitness function. This figure is to be maximized by the optimization algorithms, and is the inverse of a loss function. Due to there being a number of requirements for practical use of a spaceplate besides absolute compression, it is quite a large function, with weights that can be set to zero to eliminate optimization towards the corresponding targeted property if necessary. The formula for the FOM for a structure designed for a discrete wavelength is as follows:

$$FOM = \left(w_{fit}\sigma_{fit} + w_{T,w}\sigma_{T,w} + w_{T,f}\sigma_{T,f} + w_{pol}\sigma_{pol} + w_{highR}(1/R')\right)^{-1} \tag{2.67}$$

In which all weights are denoted as $w_{property}$, which will now be explained. In this equation, σ_{fit} is the root mean square error (RMSE) between an ideal spaceplate phase ϕ and the transmitted phase by the current design ϕ'. The factor R for which ϕ is determined is either a target compression ratio, or the most closely fitted ratio (using a built-in fit algorithm) to the current phase profile.

$$\sigma_{fit}^2(\phi', \phi) = \frac{1}{\theta_{max}} \int_0^{\theta_{max}} (\phi' - \phi)^2 \, d\theta \tag{2.68}$$

Where θ_{max} denotes the maximum acceptance angle for which the spaceplate is supposed to work, in radians.

Furthermore, $\sigma_{T,w}$ and $\sigma_{T,f}$ represent the RMSE's of the normalized transmission over the angular range where a high transmission intensity is intended (T_w) and angles to be filtered out (T_f), respectively. For the wanted angles it is the difference away from full transmission, and for the filtered angles the difference away from zero transmission:

$$\sigma_{T,w}^2(T_w) = \frac{1}{\theta_{max}} \int_0^{\theta_{max}} (1 - T_w)^2 \, d\theta \tag{2.69}$$

$$\sigma_{T,f}^2(T_f) = \frac{1}{\pi/2 - \theta_{max}} \int_{\theta_{max}}^{\pi/2} \left(T_f - 0\right)^2 d\theta = \frac{1}{\pi/2 - \theta_{max}} \int_{\theta_{max}}^{\pi/2} T_f^2 d\theta \tag{2.70}$$

This formulation leaves space for changing the desired transmission in a given region to a different value, which is why the zero is still named in equation 2.70. Matching compression factors for both p- and s-polarization is expressed using σ_{pol}, and attempts only to minimize the difference:

$$\sigma_{pol}^2 = \frac{1}{\theta_{max}} \int_0^{\theta_{max}} \left(R_p - R_s\right)^2 d\theta \tag{2.71}$$

In which R_p and R_s are the compression factors of the current design for p- and s-polarization, which are determined by fitting their phase profiles to that of an ideal spaceplate for the angular region $[0, \theta_{max}]$.

Lastly optimization for a high compression is achieved simply by the factor $1/R'$, where R' is the current compression factor of the spaceplate design. Of course, when a target is set for the compression factor, this term is not considered, as this is then caught in σ_{fit} by fitting it to an ideal phase profile $\phi(\theta)$ corresponding to the target R.

All of this is relatively straightforward. However, once it becomes necessary to formulate the FOM for a spectral band, a few things change. For every single (discrete) wavelength considered, the transmitted phase and intensity are different. Therefore, the RMSE's and R' have to be evaluated on all of these wavelengths, after which the mean value of each of the RMSE's is taken. For any evaluated value X, this means:

$$\sigma_{X,\Delta\lambda} = \frac{1}{\Delta\lambda}\int_{\lambda_0-\Delta\lambda}^{\lambda_0+\Delta\lambda} \sigma_{X,\lambda} d\lambda \tag{2.72}$$

Where $\Delta\lambda$ is the given width of the wavelength range, λ_0 is the center wavelength, and $\sigma_{X,\lambda}$ is the RMSE for value X at wavelength λ.

Additionally, a term is added which evaluates whether the compression factors of different wavelengths match with one another, and punishes large differences. This is done by taking the RMSE between the mean value of R ($\langle R' \rangle$) and the value of R at each wavelength (R'_λ) over the spectral band:

$$\sigma^2_{R,\Delta\lambda} = \frac{1}{\Delta\lambda}\int_{\lambda_0-\Delta\lambda}^{\lambda_0+\Delta\lambda}\left(R'_\lambda - \frac{1}{\Delta\lambda}\int_{\lambda_0-\Delta\lambda}^{\lambda_0+\Delta\lambda} R'_\lambda d\lambda\right)^2 d\lambda = \frac{1}{\Delta\lambda}\int_{\lambda_0-\Delta\lambda}^{\lambda_0+\Delta\lambda}\left(R'_\lambda - \bar{R}'\right)^2 d\lambda \tag{2.73}$$

This then results in the FOM for a spectral band:

$$FOM = \Big(w_{fit}\sigma_{fit,\Delta\lambda} + w_{T,w}\sigma_{T,w,\Delta\lambda} + w_{T,f}\sigma_{T,f,\Delta\lambda} + w_{pol}\sigma_{pol,\Delta\lambda} + w_{highR}(1/\bar{R}') + w_{R,\Delta\lambda}\sigma_{R,\Delta\lambda}\Big)^{-1} \tag{2.74}$$

3

Results

Many structures were generated for this thesis. To make sure they can be compared easily and do not deviate too much from previous literature, they all us SiO_2 (refractive index n = 1.444) and Si (refractive index n = 3.47638) and are generally designed for operation at (or around) a wavelength of 1550 nm.

3.1. Single structures

To test the optimization algorithm and to slowly allow complexity of the system to build up, the results are compiled based on complexity.

Evaluating and interpreting the results can be done based off the transmission intensity and phase plots, combined with the fitted compression ratio R and the estimated Strehl ratio ($\mathbb{S}$) of the structure. The Strehl ratio is a metric related to imaging quality, often used for lenses. It is the ratio of the peak intensity of the focus of a Gaussian beam traveling through a real optical element to this peak after going through an ideal optical element. It ranges from 0 to 1, and if $\mathbb{S} \geq 0.8$ diffraction will limit image resolution more than the introduced optical aberrations, making the optical element 'diffraction limited'. The Strehl ratio of a structure is estimated by taking the negative exponent of the mean square error of the phase fit that remains after R is fitted onto the phase profile such that this error is minimal van den Bos, 2000:

$$\mathbb{S} \approx e^{-\sigma_{fitted}^2} \tag{3.1}$$

Note that σ_{fitted} is not necessarily the same as σ_{fit} from equation 2.68, since this can also refer to the fit to a target compression ratio R while σ_{fitted} only aims to minimize the root mean square error of the fit, with R being a free variable. Any valid spaceplate included in 3.1 has a Strehl ratio of at least 0.96 (meaning phase profile RMSE is smaller than 0.2). This should ensure all spaceplates are diffraction limited and are feasible for use in a sensitive optical system.

3.1.1. Reproducing results

The code provided in J. Pagé and Reshef, 2021 was designed to optimize a structure to mimic free space propagation of light for a single given wavelength, with a target R to optimize towards. By then selecting a higher target R, greater compression could be achieved until the optimization no longer managed to converge to a satisfactory result.

This code has since been reworked as has been explained in section 2.2. Entering the same starting requirements, (target R of 340, 27 layers, $\lambda = 1550$nm), yields a functioning spaceplate with properties similar to those found in J. T. R. Pagé et al., 2022. These results can be seen in figure 3.1.

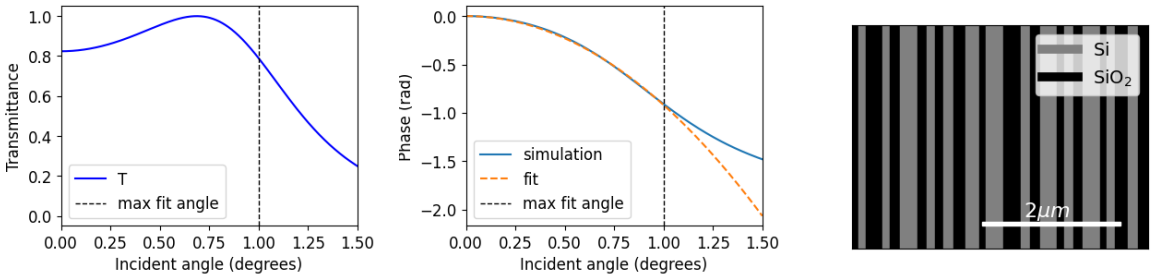

(a) Transmission intensity (b) Simulated phase (c) Structure

Figure 3.1: A spaceplate design for p-polarized light with an R of 351, and a Strehl ratio of 0.99997, exceeding that of J. T. R. Pagé et al., 2022.

While this design does not exactly match the compression factor found in the cited paper, it does show the capabilities of the optimization algorithm to get close to its results.

After producing the previous result relatively quickly, an attempt was made using a target R of 500 instead, to see whether improvements could be made. This resulted in the structure which can be seen in figure 3.2. After this, further attempts yielded results with Strehl ratios lower than that of J. T. R. Pagé et al., 2022, and so the exploration was halted here. Further exploration of this situation also seems futile, since its applications are limited due to polarization dependence, low angular range and zero bandwidth, problems that will be discussed in the next section.

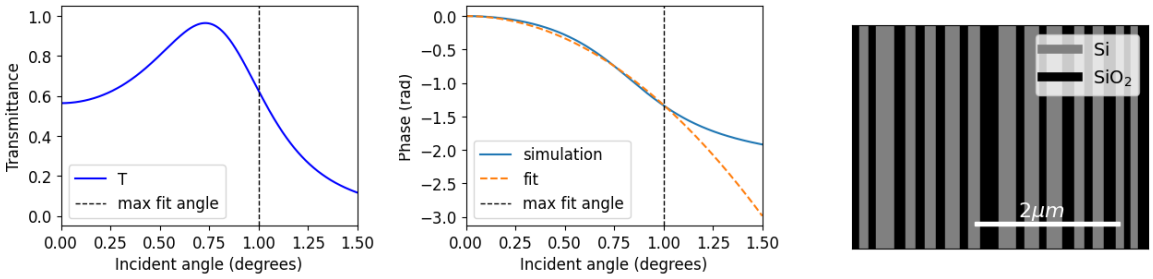

(a) Transmission intensity (b) Simulated phase (c) Structure

Figure 3.2: A spaceplate design for p-polarized light with an R of 545, and a Strehl ratio of 0.9995, still exceeding that of J. T. R. Pagé et al., 2022.

3.1.2. Exploring optimization capabilities

For the sake of testing the optimization algorithm, starting parameters are chosen to which complexity will be added in steps. First off, the parameters are as follows:

- Target R = 40
- Number of layers = 27
- λ = 1550 nm
- θ_{max} = 5 degrees (meaning NA = 0.087)
- Optimized polarization = p-polarization

The reasoning for the relatively low θ_{max} is explained at the end of section 3.2. This results in the spaceplate design seen in figure 3.3. This spaceplate has a thickness of 4.25 μm and an effective distance of 151 μm, with an R of 35.5 and Strehl ratio 0.9865.

There are three main problems with this design for practical use. The first is the lack of transmission in certain wanted angles, which will cause unwanted changes in the PSF of transmitted light and in general will lead to a loss of power. Secondly, this spaceplate is designed to work for p-polarized light. If s-polarized light travels through this spaceplate, it will in this case experience a distance of 138 μm instead of 151, meaning unpolarized light will smear out between the effective distances of its polarized

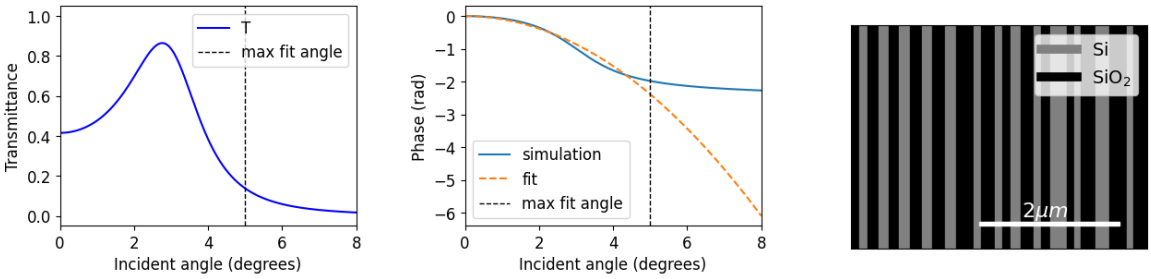

(a) Transmission intensity (b) Simulated phase (c) Structure

Figure 3.3: A spaceplate design for p-polarized light with a compression ratio of 35.5 and an NA of 0.087.

components. Third and last, this spaceplate is optimized for a single wavelength only, and so will not have the same compression or transmission for other wavelengths.

To tackle the problem of transmission, a term was added in the figure of merit calculation, as explained in section 2.2.3. Selecting a spaceplate design with a normalized transmittance > 0.8 over the wanted angular range with the highest possible R then yields the design seen in figure 3.4. The spaceplate has a thickness of 2.98 μm and an effective distance of 54.49 μm, with an R of 18.3 and Strehl ratio 0.99998.

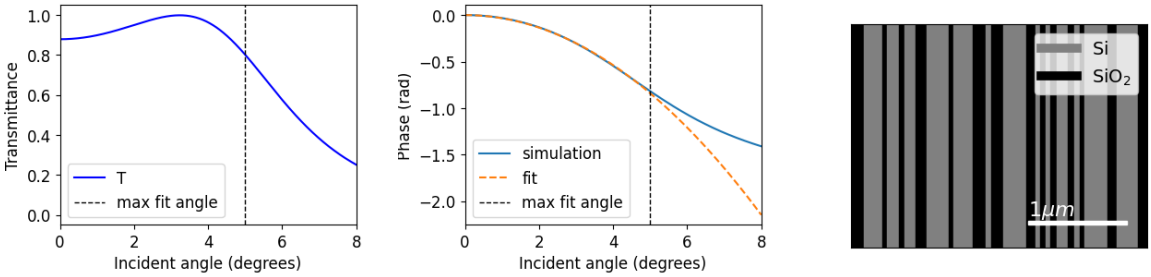

(a) Transmission intensity (b) Simulated phase (c) Structure

Figure 3.4: A spaceplate design for p-polarized light with a compression ratio of 18.3 and an NA of 0.087, achieving average transmission intensity in the intended region of 0.9335.

Disregarding transmission profiles for a moment, the issue of difference in compression for different polarizations also needs addressing. By having the optimization match the compression of both polarizations, this problem is solved up to a point. In this case, a spaceplate for which the compression factors of both polarizations were within 1% of each other is deemed satisfactory. The resultant spaceplate can be seen in figure 3.5. It has a thickness of 4.05 μm, an effective distance of 49.2 μm, and Strehl ratio 0.9998. Its compression factors are 12.14 and 12.17, for p- and s-polarization respectively.

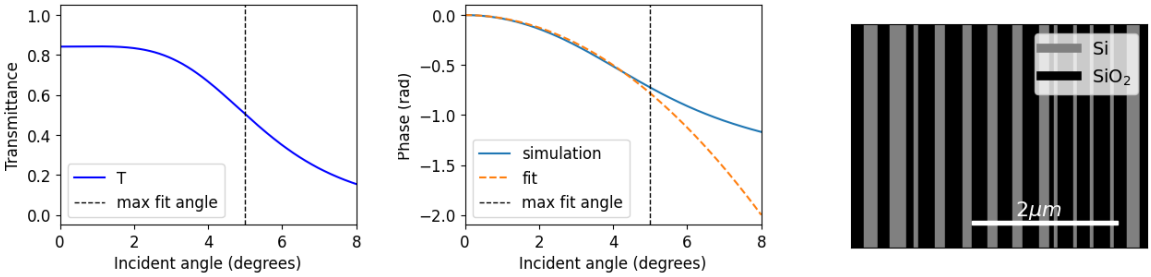

(a) Transmission intensity (b) Simulated phase (c) Structure

Figure 3.5: A (semi) polarization-independent spaceplate design with compression ratios of 12.14 and 12.17 for p- and s-polarized light respectively, and an NA of 0.087.

Lastly, optimizing the spaceplate for multiple wavelengths at the same time shows one of the flaws

of the thin film spaceplate. Due to the design relying on a combination of resonances within the structure, the influence of wavelength on the transmitted phase profile is very large, meaning consistent compression is difficult to achieve. To illustrate this, a spaceplate design is optimized for a bandwidth of 1 nm and one with a bandwidth of 5 nm and their compression ratios dependent on wavelength are shown in figure 3.6.

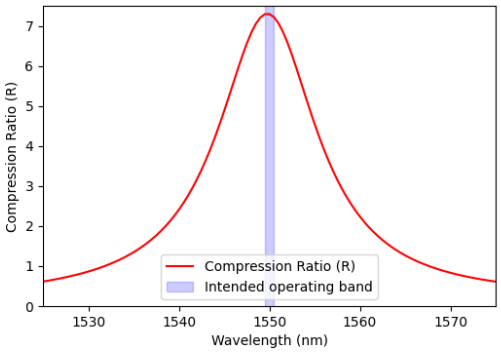

(a) Compression of structure optimized for band of 1 nm around 1550 nm.

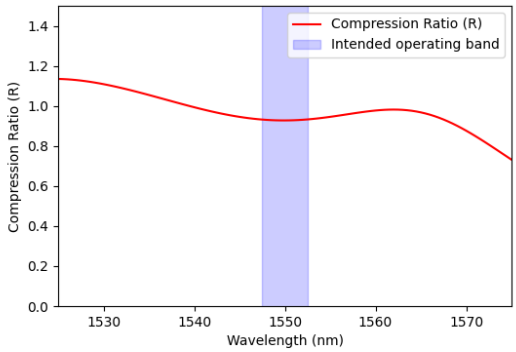

(b) Compression of structure optimized for band of 5 nm around 1550 nm.

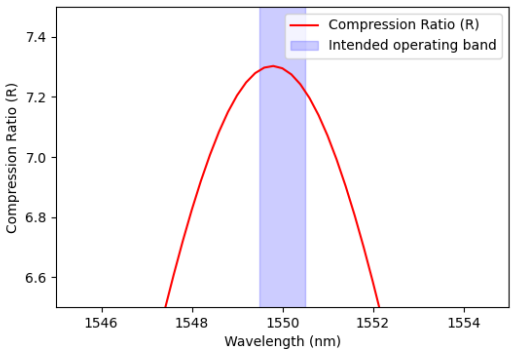

(c) Compression of structure optimized for band of 1 nm around 1550 nm zoomed in on intended band.

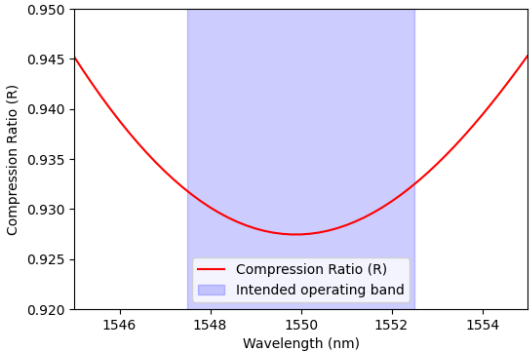

(d) Compression of structure optimized for band of 5 nm around 1550 nm zoomed in on intended band.

Figure 3.6: Plots showing the compression factor dependent on wavelength of two different spaceplate designs, optimized for 1 nm and 5 nm bands respectively around a center-wavelength of 1550 nm. The plots clearly show the wavelength dependence has a large influence on performance in terms of compression factor.

The results in figure 3.6 shows that expanding the required operational bandwidth of the spaceplate leads the optimization algorithm to design devices with lowered compression factors. Only adding a 1 nm bandwidth as a requirement lowers the highest found compression factor to approximately 7.3, which is roughly 5 times lower than that without this constraint. Within this band of 1 nm, there is also still a significant variation in compression factor, within an interval size of 0.1. Increasing the bandwidth further to 5 nm results in spaceplate designs which have compression factors below 1, meaning propagation space was lengthened instead by this spaceplate.

Considering this was only at a maximum bandwidth of 5 nm, which cannot be considered very broad, the choice was made to focus research in this thesis on monochromatic (discrete wavelength) spaceplates, in order not to limit compression ratios and effective distances by added bandwidth requirements.

3.2. Dependence on maximum incident angle

To establish the relations of different achievable parameters through the designed algorithm, a sweep is conducted through incoming angles. This is done for spaceplate designs with 27 layers, again at 1550 nm. Layer thicknesses at start are set between 50 and 250 nm. All spaceplates were required to

meet a threshold Strehl ratio of 0.967 (which translates to RMSE of the phase equal to approximately 1/30) to ensure they were usable as spaceplates. The resulting graph, shown in figure 3.7, shows a large dependency between the maximum accepted incoming angle and the maximum compression factor. This was to be expected, looking at the formulation of the limit of R in equation 1.61.

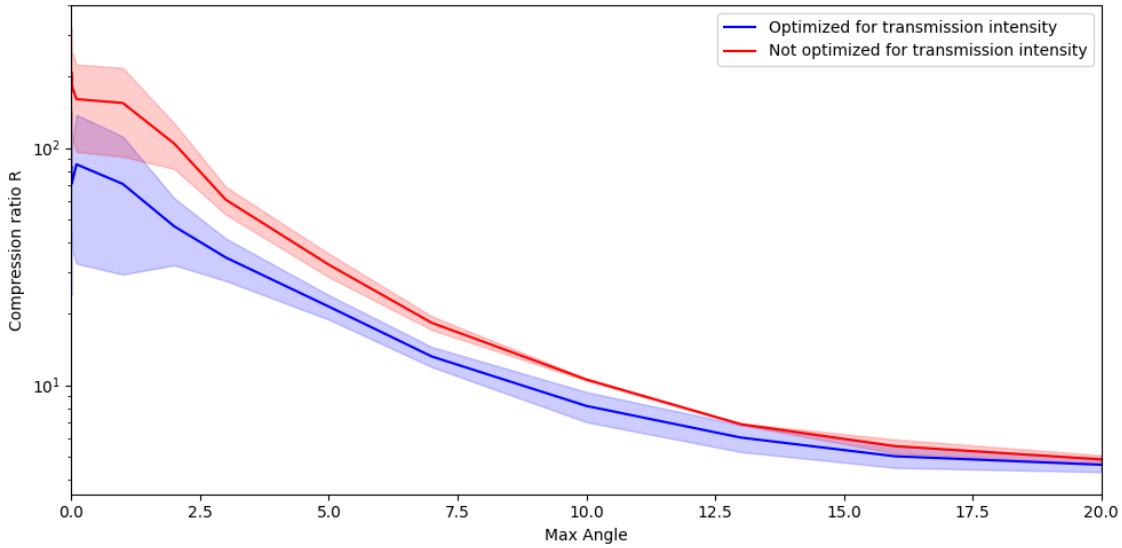

Figure 3.7: Mean compression ratio R versus θ_{max}, surrounded by an area of one standard deviation above and one below the mean. Results in blue from optimization with $w_{T,w} = 0.25$ results in red with $w_{T,w} = 0$ (see equation 2.67). The compression factor R decreases with larger maximum incoming angles in degrees, i.e. higher NA.

What is interesting in this figure is the fact that it does not seem to go towards infinity around $\theta = 0$. At this angle, R becomes arbitrary since it effectively removes the need for a specific phase profile. This means that the function in 3.7 is discontinuous at $\theta = 0$. Besides this, however, the maximum value for R found from these optimizations is 467, at a very small angle ($\theta_{max} = 0.0001$). Previous results have shown that it is possible to exceed this value, but not by an enormous margin, which would be expected if there was a divergence toward infinity at $\theta = 0$. Whether or not there actually is a divergence in the globally optimal solutions is impossible to say from these results, as they showcase the inability of the optimization algorithm to reliably find the global optimum.

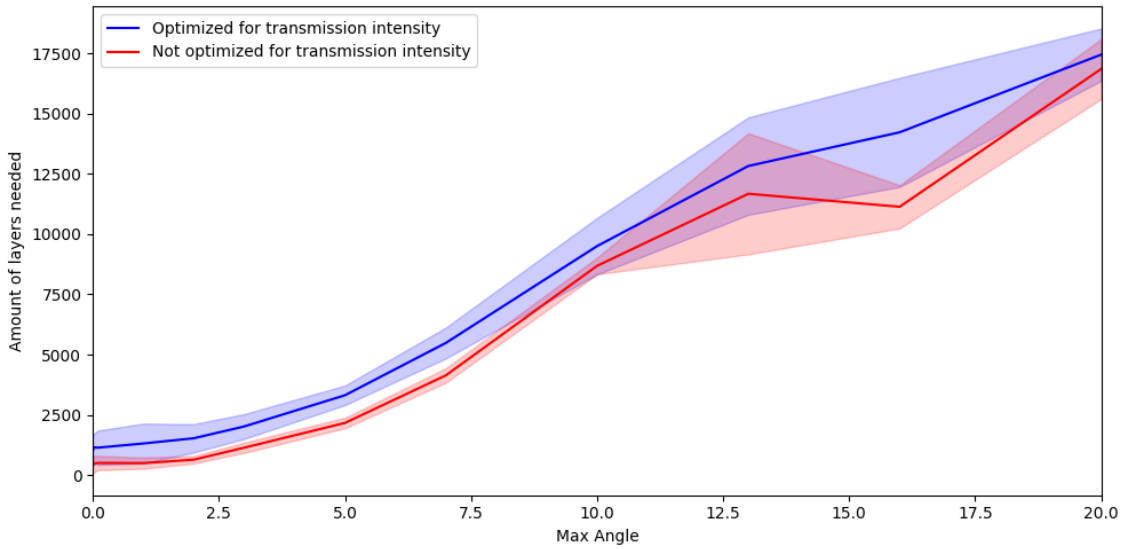

Figure 3.8: The mean amount of layers needed to theoretically achieve 1 cm of effective distance, surrounded by one standard deviation above and one below the mean.

A consequence of the decreasing compression factor with increasing incoming angles is the need for a larger amount of layers to achieve the same effective distance for larger incoming angles. Using the assumption that the structure can be repeated to achieve a higher effective distance without it affecting the compression factor or quality of the phase profile, a rough estimate can be made of the amount of layers needed to reach some arbitrary effective distance. Plotting this, using the same spaceplate designs as those used for the last figure, results in figure 3.8. Of course, these assumptions are quite steep, so the actual values will most likely be higher, if reaching 1 cm of effective distance for a useful numerical aperture is even possible at all. For this reason, in the rest of this thesis a conservative maximum acceptance angle of 5 degrees (NA of 0.087) is used for the spaceplate designs.

3.3. Achieving large effective distances through repetition

Whether a spaceplate can actually be useful in industry is highly dependent on its absolute effective distance in the end. In this section, monochromatic spaceplates are used in an attempt to maximize this distance.

If the spaceplate functions flawlessly, transmitted light should not differ from the light coming into it, except in the distance traveled. Therefore it stands to reason that sending light through multiple spaceplates consecutively would not change their functioning. Since it is increasingly computationally expensive to expand the number of layers in the optimization protocol in order to extend the resultant effective distances, repeating a unit cell may be an avenue to reach large effective distances nonetheless. Repeating a structure that functions as a spaceplate should ideally result in a structure that retains the same compression factor, effectively scaling the effective distance by a factor N, with N being the number of repetitions. This is assuming the repetition of the structure does not introduce undesired additional interferences across different unit cells which could change the transmission phase and magnitude profiles. Additionally, angles that previously provided constructive interference resulting in a high transmission intensity would be expected not to decrease in transmission, since this same exact constructive interference pattern is present in each separate ”spaceplate” that is stacked on top of each other. Lastly, any error of the phase would be expected to add linearly, since it is also expected that the induced phase profile adds linearly.

To test these hypotheses and see if additional interferences between unit cell structures play a large role, optimized structures are repeated and their transmission phase and intensity are evaluated using TMM. This is done for three structures, all of which consist of 33 alternating layers of silicon and silicon-dioxide, optimized for a wavelength of 1550 nm for a half angle up to 5 degrees (NA = 0.087) in air. Of these designs, the second design has layer thickness boundaries that are shifted by 50 nm to have generally thicker layers, and the third design is only optimized for p-polarized light. These alterations are made to gauge their effects on achievable effective distances.

Additionally, modern manufacturing techniques are not without flaws. When manufacturing similar layer thicknesses, confidence intervals upwards of 5 nanometers are usual (Qian et al., 2017, Hattrick-Simpers et al., 2019). Precision errors like these can have significant effects on the functioning of multilayer thin film optics, which rely on interference based on a relationship between the wavelength and angle of traveling waves and the thickness of the medium (Mielenz, 1960).

This section shows results of attempts of repeating the structure of three different spaceplate designs as much as possible, to achieve an effective distance that has a possibility for practical applications. It also reviews the effects of precision errors in layer thicknesses on the achievable effective distances.

3.3.1. Unit structure

In this section, the structures and transmission intensity versus incoming angle are shown of the designs that were repeated in an attempt to reach a large effective distance. All of the designs consist of 33 alternating layers of silicon and silicon dioxide, and are optimized for a wavelength of 1550 nm and a half angle up to 5 degrees (NA = 0.087). The second design has a focus on using bigger layer thicknesses, and the third design was only optimized to function as a good spaceplate for p-polarized light. Additional information on the results of the spaceplate optimization can be found in table 3.1.

	Design 1	Design 2	Design 3
Effective distance in microns	19.26	25.12	30.23 (p) 24.77 (s)
Compression factor	2.94 (p & s)	2.95 (p & s)	3.99 (p) 3.27 (s)
RMSE of fitted phase profile in rad	5.49e-4 (p) 5.02e-4 (s)	5.23e-4 (p) 1.11e-3 (s)	3.18e-4 (p) 2.23e-4 (s)
Strehl Ratio	0.99945 (p) 0.99950 (s)	0.99880 (p) 0.99890 (s)	0.99968 (p) 0.99978 (s)
Layer thickness boundaries in nm	150–300	200–350	150–300
Polarization	p & s	p & s	p or s

Table 3.1: Spaceplate designs to be repeated to reach large effective distances.

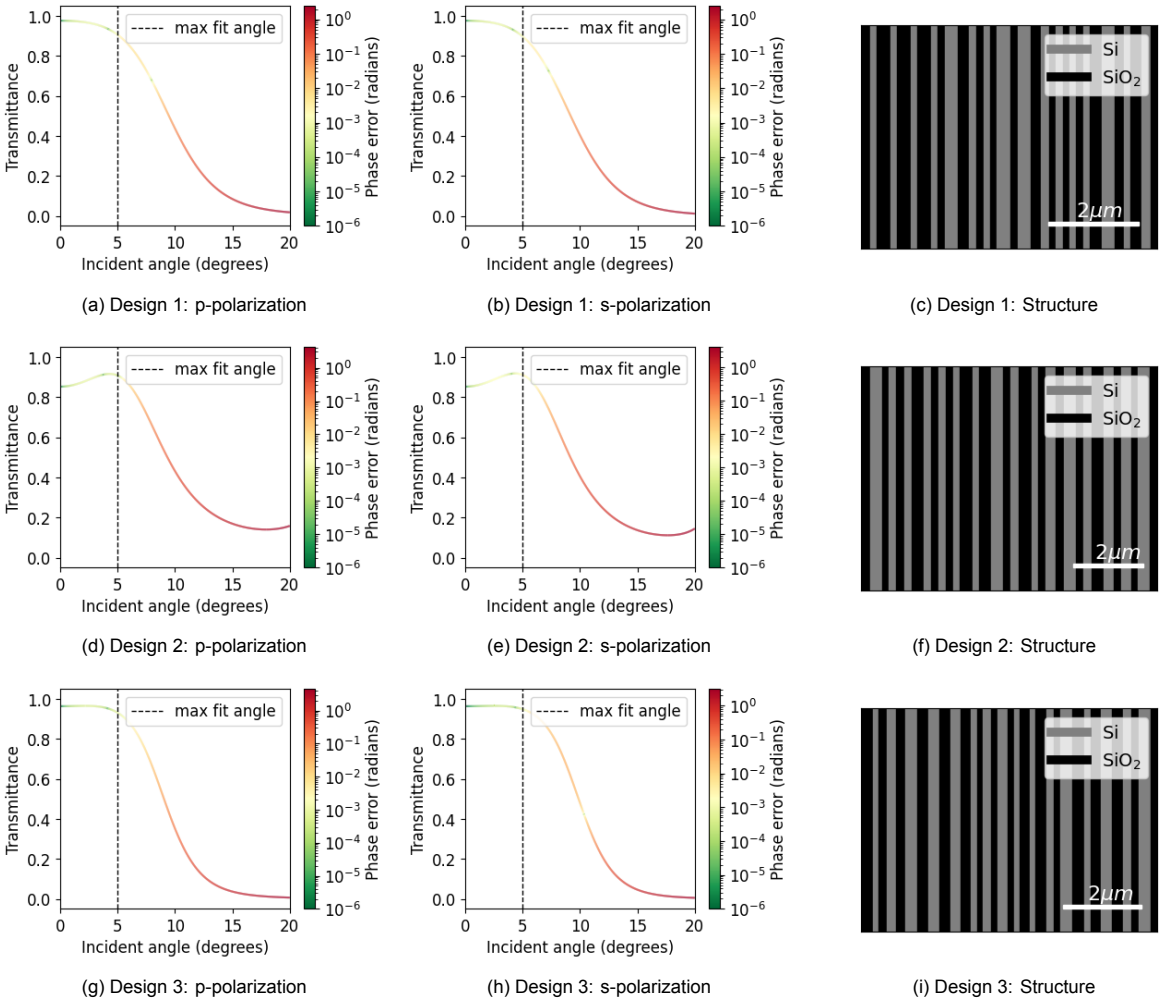

(a) Design 1: p-polarization (b) Design 1: s-polarization (c) Design 1: Structure

(d) Design 2: p-polarization (e) Design 2: s-polarization (f) Design 2: Structure

(g) Design 3: p-polarization (h) Design 3: s-polarization (i) Design 3: Structure

Figure 3.9: Comparison of three spaceplate designs with corresponding transmission intensity and phase error (= fit(θ) - simulated phase at θ) for p- and s-polarization, and structures.

As figure 3.9 shows, all three have a transmission intensity near 1 within the intended angular range.

What has become apparent during the optimization attempts is that adjusting the layer thickness boundaries in this way, from design 1 to design 2, will have an adverse effect on the RMSE of the phase profile, meaning it matches the intended phase profile less. Still, it does function at a spaceplate quite

well and would, in this non-repeated form, easily fit into a diffraction limited system. It also performs worse in terms of compression, going from 2.94 to 2.51.

Additionally, loosening the constraints by only optimizing for p-polarization instead of both polarizations leads to better results in the other parameters, allowing for a higher compression factor while simultaneously allowing a better match to the phase profile, as shown in the difference of RMSE between designs 1 and 3. Interestingly, the phase match is better for s-polarization than it is for p-polarization while its compression factor is significantly lower.

3.3.2. Ideal structure

In this section, the results are shown of repeated stacking of the structures that were shown in section 3.3.1. During this repetition none of the thicknesses in the structure get altered, and there is no gap in between them.

The designs are repeated up until they are no longer diffraction limited, which is assumed to be at a Strehl ratio of 0.8. Strehl ratio is approximated using equation 3.1 which was shown earlier in section 3.1.

Repeatedly stacking these designs results in an increase in the RMSE of the phase fit, which is the reason it is not possible to repeat them thousands of times and still end up with a useful device. The RMSE of the phase fit versus the amount of repetitions of the base structure of each of the designs can be seen in figure 3.10. This figure shows that the RMSE of the phase fit follows a semi-linear pattern, which implies that the influence of additional internal interferences due to repetition on the phase fit is relatively small. There is some oscillation in the pattern, which is likely caused by these additional interferences.

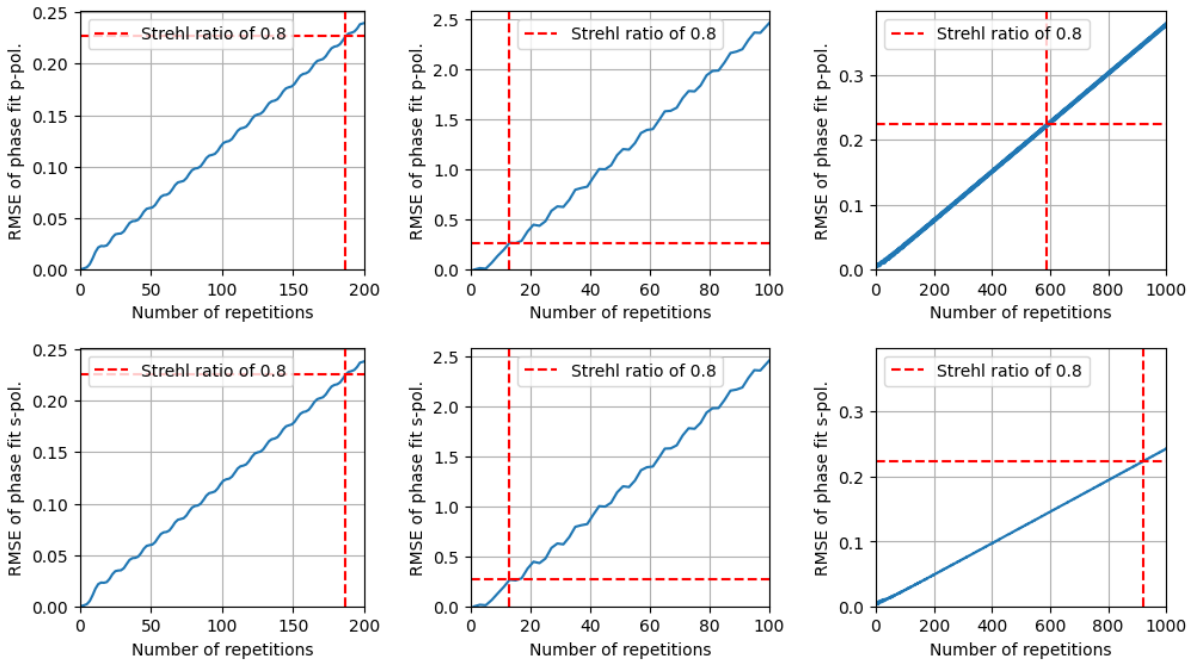

(a) Design 1, reaching 185 repetitions before no longer being diffraction limited

(b) Design 2, reaching 12 repetitions before no longer being diffraction limited

(c) Design 3, reaching 589 and 919 repetitions for p- and s-polarized light respectively before no longer being diffraction limited

Figure 3.10: RMSE of the phase fit versus amount of repetitions, with Strehl ratio of 0.8 at the red dotted lines.

Unfortunately, based on these results no relation could be found between the RMSE of the phase fit of the unit structure to the approximate linear rate of increase of the RMSE with the number of repetitions of this structure. The effective distance one could theoretically achieve while remaining diffraction limited, shown in figure 3.11, is completely dependent on this rate of increase. Additionally, this figure confirms the assumption that stacking a spaceplate will result in a linear increase of its effective distance. In this graph, too, a slight oscillation is visible due to added internal interferences,

but a general linear trend is clearly present, and the compression ratios remain close to those of the spaceplate that forms the unit cell.

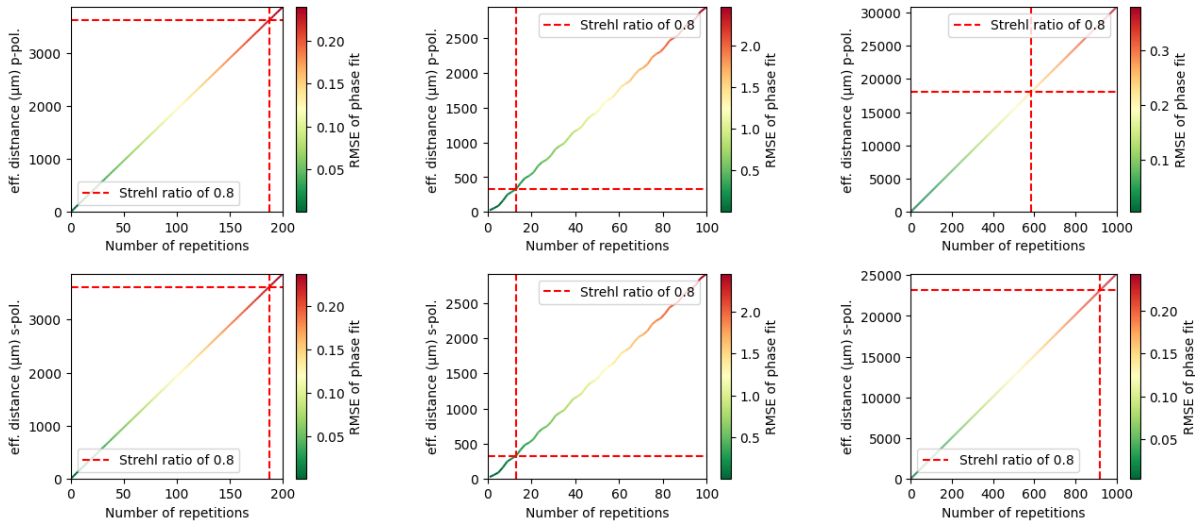

(a) Design 1, reaching an effective distance of 3.575 mm before no longer being diffraction limited

(b) Design 2, reaching an effective distance of 0.304 mm before no longer being diffraction limited

(c) Design 3, reaching effective distances of 18.2 and 23.2 mm for p- and s-polarized light respectively before no longer being diffraction limited

Figure 3.11: Effective distance versus amount of repetitions, with Strehl ratio of 0.8 at the red dotted lines.

Repeating these structures until they cross Strehl ratio of 0.8 does not take into account transmission intensity. This intensity is also highly dependent on the interference patterns inside the structure, and whether there are possible states in which the incoming wave can sustain itself inside the structure. Figure 3.12 shows that having a high transmission intensity at these amounts of layers is still possible.

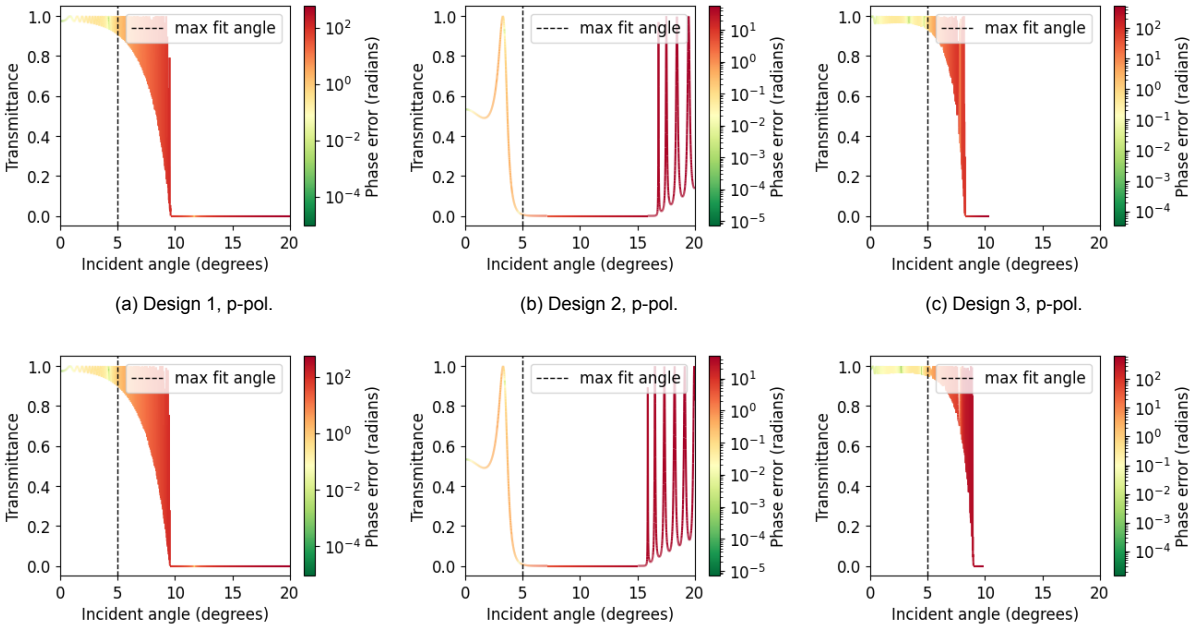

(a) Design 1, p-pol.

(b) Design 2, p-pol.

(c) Design 3, p-pol.

(d) Design 1, s-pol.

(e) Design 2, s-pol.

(f) Design 3, s-pol.

Figure 3.12: Transmission and phase error of repeated spaceplate structures for p- (top) and s-polarization (bottom).

For both design 1 and 3, a transmission intensity near 1 is reached. The result of design 2 shows that this high transmission is not fully guaranteed, and should be examined before any actual repeated manufacturing takes place. Also, the transmission intensity plot of design 2 shows that at higher incident angles, transmission peaks may occur which is important to note if angular stray light is an issue for the envisioned application.

A summary of the properties of the repeated structures with the number of repetitions at which they have a Strehl ratio of 0.8 is shown in table 3.2. Notably, this shows that achieving effective distances into the centimeter range is theoretically possible, while maintaining a decent transmission intensity (assuming zero absorption). However, it also shows that the amount of layers that would need to be manufactured for this is very high and so probably not feasible.

Design	Pol.	Eff. Distance (mm)	Thickness (mm)	Layers	Avg. Trans.	R
1	Both	3.575	1.211	6105	0.9768	2.95
2	s	0.303	0.102	396	0.4762	2.97
	p	0.305	0.102	396	0.4722	2.99
3	p	18.2	4.46	19437	0.9798	4.08
	s	23.2	6.95	30327	0.9810	3.34

Table 3.2: Summary of effective distances, structure thickness, number of layers, average transmittance, and compression ratio for each design and polarization.

3.3.3. Manufacturing errors

Theoretically repeating a structure to achieve a large effective distance still does not guarantee this distance can be realized in practice. To further evaluate the manufacturability of thin film spaceplates with large effective distances, precision errors were introduced. This was done by taking the thicknesses of the repeated structure, and adding a precision error ϵ to them according to a uniform distribution:

$$\epsilon_p \sim U(-e_p, e_p) \tag{3.2}$$

With e_p being the maximum precision error induced by the manufacturing process. Note that this evaluation does not account for a possible accuracy error (which would introduce a constant offset to all thicknesses), and assumes all layers to have a perfectly uniform thickness without local defects (such as trapped dust particles or general surface roughness). Still, it should give a feeling for the error sensitivity of the structure.

In this way, 200 different ”defect” structures are generated for each separate number of repetitions N, to provide a decent sample size for statistical analysis of manufacturability at different amounts of repetition and precision errors. Introducing these errors significantly affects the performance of the repeated structures, both in their transmission intensity and matching of the correct phase parabola. An example of this erroneous behavior can be seen in figure 3.13, which shows the average RMSE of the phase and transmission of the complete batch of samples with defects between -1 nm and 1 nm, against those of the ideal structure of design 1.

To gauge the highest effective distance that could be manufactured given a certain maximum precision error, all samples were tested to a set of criteria: a minimum of 25% average transmission over the intended angular range (0 to 5 degrees), a phase profile match with a Strehl ratio above 0.8 (meaning RMSE < 0.223), and in the case of the polarization matched designs the different compression factors of both polarizations were to remain within 5% of each other. When less than 10% of all defect structures adhered to these criteria, it was deemed that the used number of repetitions would no longer result in working spaceplates for the tested manufacture error, enabling the plotting of maximum achievable effective distance. This test resulted in the plots shown in figures 3.14a, 3.14b and 3.14c.

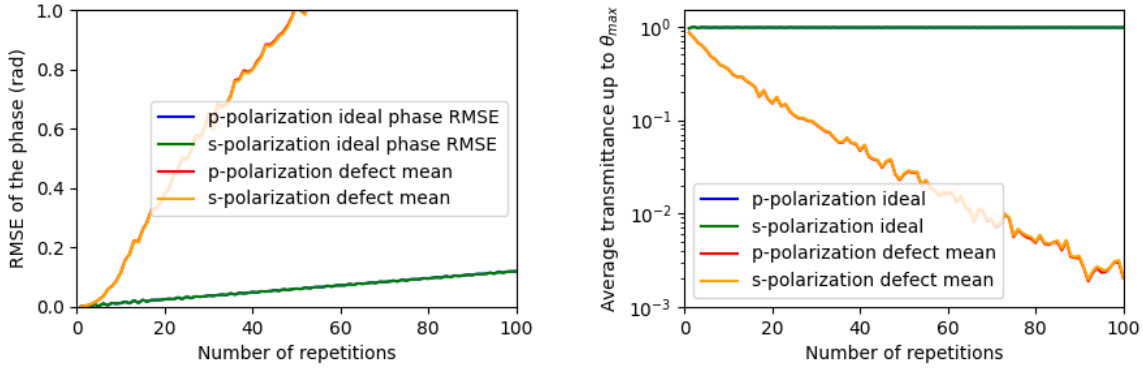

(a) RMSE of the phase parabola

(b) Average transmission

Figure 3.13: The result of introducing defects between -1 nm and 1 nm in design 1. Transmission data show the average transmission within the wanted angular regime, up to 5 degrees, with the defect lines showing the mean of that parameter for the 200 samples per number of repetitions.

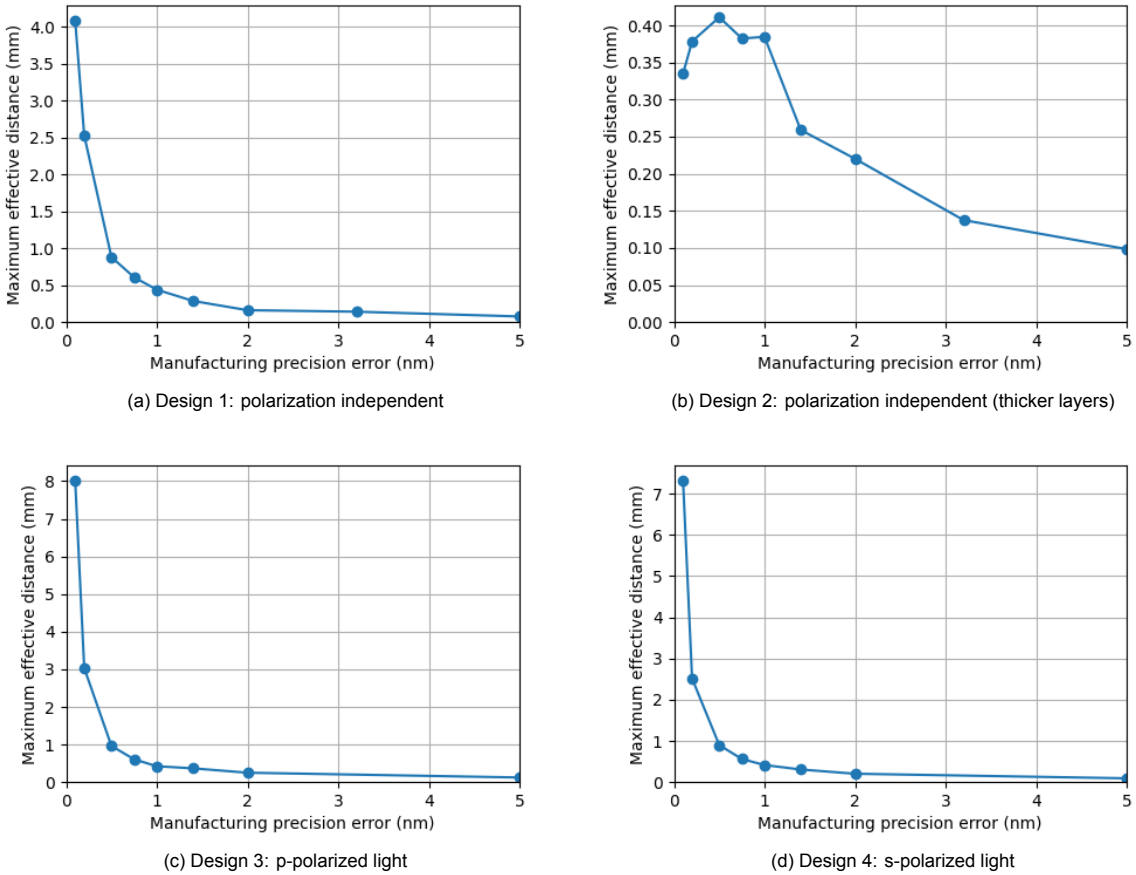

(a) Design 1: polarization independent

(b) Design 2: polarization independent (thicker layers)

(c) Design 3: p-polarized light

(d) Design 4: s-polarized light

Figure 3.14: Manufacturing precision error size e_p (see equation 3.2) versus maximum effective distance for all designs, where design 3 has different achievable effective distances depending on polarization.

As these figures show, manufacturing errors have a large influence on the viability of thin film spaceplate with a large effective distance. Furthermore, these figures do not show the quality of the transmission intensity profile, only whether the average transmission intensity is sufficiently high. When plotting single defect structures, it becomes apparent that the ideal even transmission profile is far from guaranteed when precision errors are introduced, as shown in figure 3.15. The shown transmission profile is that with the average transmission out of all defect samples at the given number of repetitions.

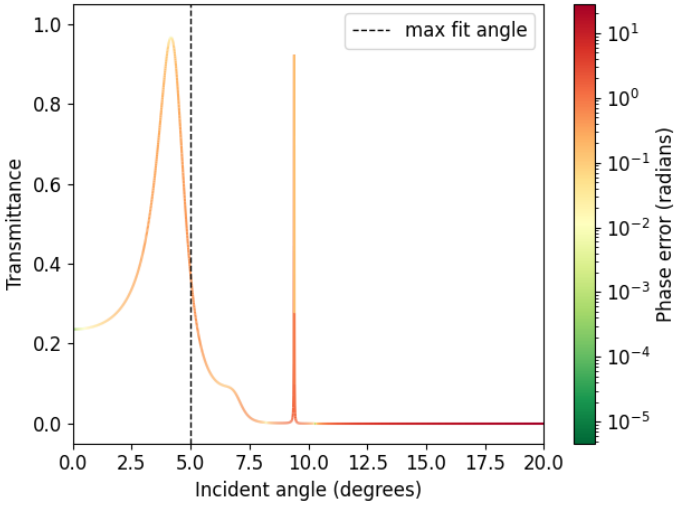

Figure 3.15: Transmission profile of design 1 repeated 6 times with introduced defects between -1 and 1 nm, of sample with the average transmission out of all defect samples at N=6. Average intended transmission of 0.4483, Strehl ratio of 0.818.

3.4. Angular stray light filters

To create angular stray light filters, the input parameters of the optimization algorithm were chosen such that only the transmission profile of the thin film structure was taken into account. The figure of merit was dependent only on the terms $w_{T,w}\sigma_{T,w}$ and $w_{T,f}\sigma_{T,f}$, while all other weights were set to zero. In defining the wanted and unwanted angular regimes, a range of angular tolerance region sizes were also taken into account to study their effect. A typical transmission profile with the different angular regimes included looks something like figure 3.16. The tolerance region signifies a range of incoming angles for which there is no target that the optimizer is trying to converge towards, and was introduced to allow a continuous slope downwards between optimized regions. It was devised this way since the transition from full transmission to zero transmission will be a continuous curve, and doing it without a tolerance region may result in lower values in the range where full transmission is required. This way, the location of the slope can hopefully be more consciously placed. The optimizer was given layer thickness boundaries of 150 to 300 nm and a θ_{max} of 5 degrees.

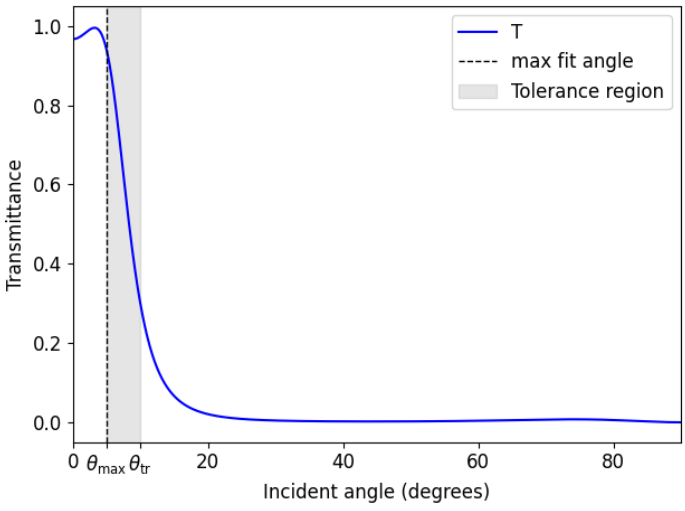

Figure 3.16: A typical transmission profile with a hypothetical tolerance region with a size of 5 degrees ($\theta_{max} = 5$ and $\theta_{tr} = 10$) on which no explicit optimization is performed.

3.4.1. Single function

To evaluate the performance of the thin film structures as angular stray light filters, contrast ($\mathbb{C}$) and suppression ratio (R_{supp}) were used as metrics. They are defined as:

$$\mathbb{C} = \frac{\bar{T}_w - \bar{T}_f}{\bar{T}_w + \bar{T}_f} \tag{3.3}$$

$$R_{supp} = \frac{\bar{T}_w}{\bar{T}_f} \tag{3.4}$$

Where:

$$\bar{T}_w = \frac{1}{\theta_{max}} \int_0^{\theta_{max}} T d\theta \tag{3.5}$$

$$\bar{T}_f = \frac{1}{\frac{\pi}{2} - (\theta_{max} + \theta_{tr})} \int_{\theta_{max}+\theta_{tr}}^{\frac{\pi}{2}} T d\theta \tag{3.6}$$

In which θ_{max} is the incoming angle up to which full transmission is desired and θ_{tr} is the size of the tolerance region before the angular region that is to be filtered out.

Furthermore, to be able to compare them to periodic structures like that of Qian et al., 2017, additional optimizations were done to find periodic angular stray light filters. These optimizations were done by having a period of 2, 4, or 6 layers which had variable layer thicknesses, and repeating these 500 or 1000 times every time before evaluating the result. This way, they are assumed to be able to represent periodic solutions that are created based on the idea of photonic bands, where infinite periodicity is assumed. They were optimized with a tolerance region size of 2 degrees, and layer thickness boundaries of 150 to 300 nm, just like the non-periodic ones. The two best periodic filters were chosen to use for comparison to the non-periodic filters, their resulting photonic band plots can be seen in figure 3.17.

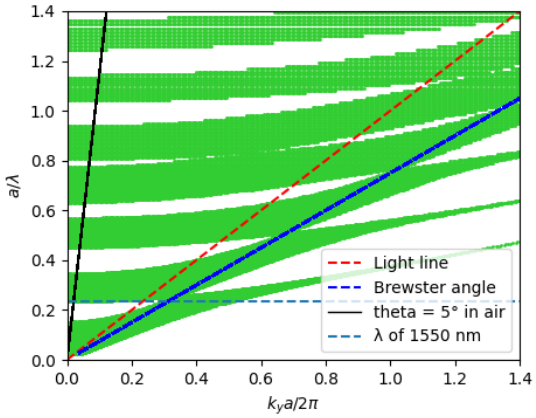

(a) Photonic band structure for p-polarized light — 2-layer period

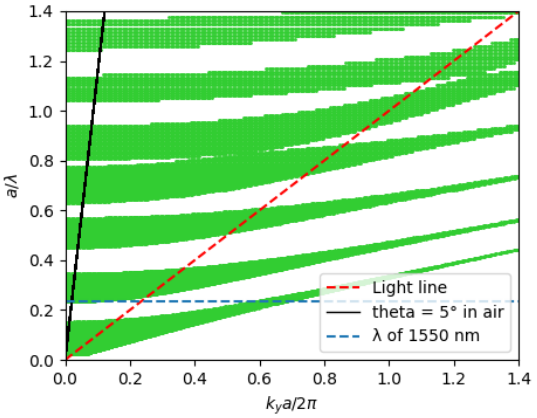

(b) Photonic band structure for s-polarized light — 2-layer period

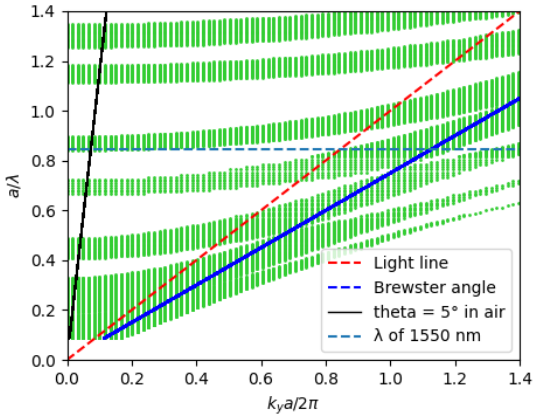

(c) Photonic band structure for p-polarized light — 6-layer period

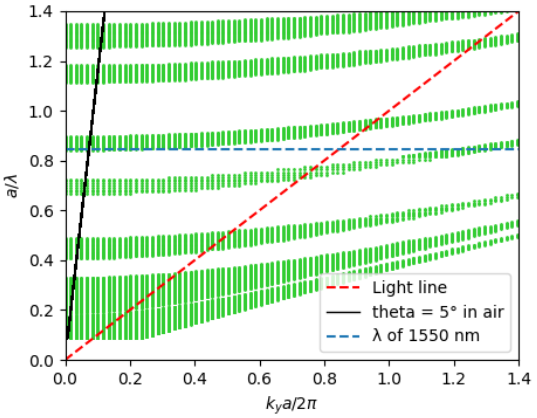

(d) Photonic band structure for s-polarized light — 6-layer period

Figure 3.17: Photonic band structures of optimized periodic filters for p- and s-polarized light. Bandgaps appear near the design wavelengths, similar to the concept discussed in Qian et al., 2017. In the 6-layer period plots, resolution limitations cause partial cutoff at the bottom. Parameter a is equal to the total thickness of a single period, k_y is the transversal wavenumber, also referred to as k_{tv} in this thesis.

To compare the periodic solutions with the non-periodic ones, the contrasts of both are plotted. In the periodic case, this means the contrast of a structure made of N periods, with N being an integer, such that the total amount of layers in the thin film stack matches that on the x-axis. The plots of non-periodic solutions optimized with tolerance region sizes 0.5 and 2.0 degrees can be seen in figure 3.18. They are both plotted without taking into account a tolerance region, even though that was included in the optimization process, to permit fair comparison.

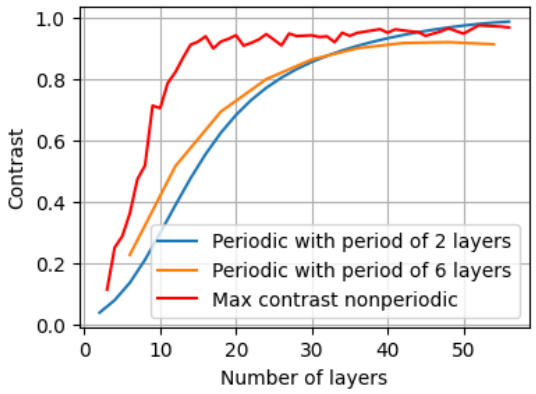

(a) Max contrast (p-polarization) — 0.5° tolerance region design

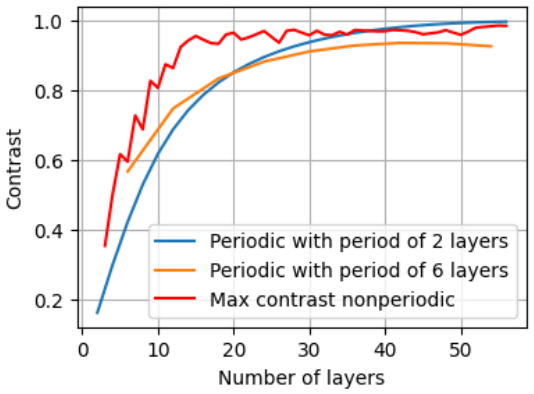

(b) Max contrast (s-polarization) — 0.5° tolerance region design

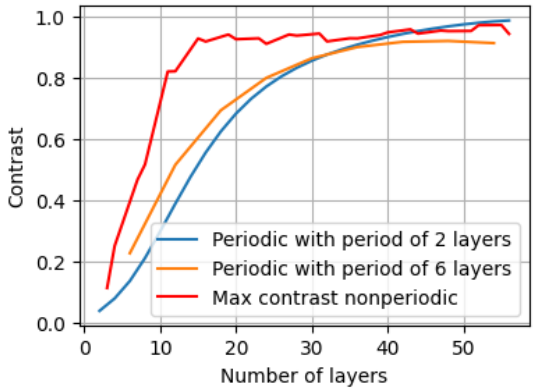

(c) Max contrast (p-polarization) — 2° tolerance region design

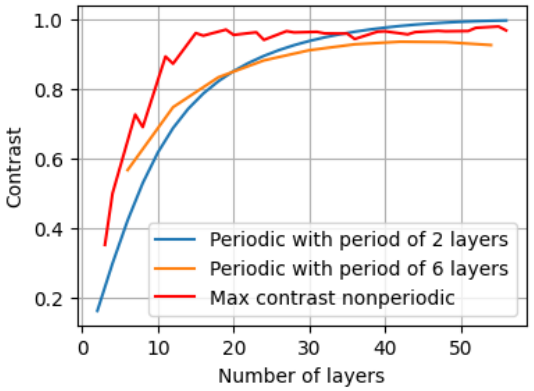

(d) Max contrast (s-polarization) — 2° tolerance region design

Figure 3.18: Maximum contrast found versus number of layers in the structure, for both p- and s-polarized light. Top row: structures optimized with a 0.5° tolerance region; bottom row: with a 2° tolerance region. In all cases, contrast is plotted assuming no tolerance region is permitted during evaluation.

This plot shows that situations exist where non-periodic solutions will greatly outperform the periodic ones. In this case, one can observe that the contrast achieved by non-periodic solutions when the amount of available layers is below 25, with the given layer thickness boundaries, is much greater using an optimized non-periodic solution than a periodic one. It is also worth noting that the difference between the angular stray light filters optimized using a tolerance region size of 0.5 degrees do not differ much from those with a size of 2 degrees. Zooming in showed slightly higher peaks in the case of 0.5 degrees, and so for the next plots a non-periodic design from that batch was chosen.

The chosen angular stray light filter is a design with 24 layers, chosen conveniently for comparisons since 24 is divisible by all periods in the set of periodic solutions. Note that at lower numbers of layers, the difference between non-periodic and periodic solutions is even larger, but for the sake of fair comparison they were not chosen here. The transmission profile of the chosen design can be seen in figure 3.19.

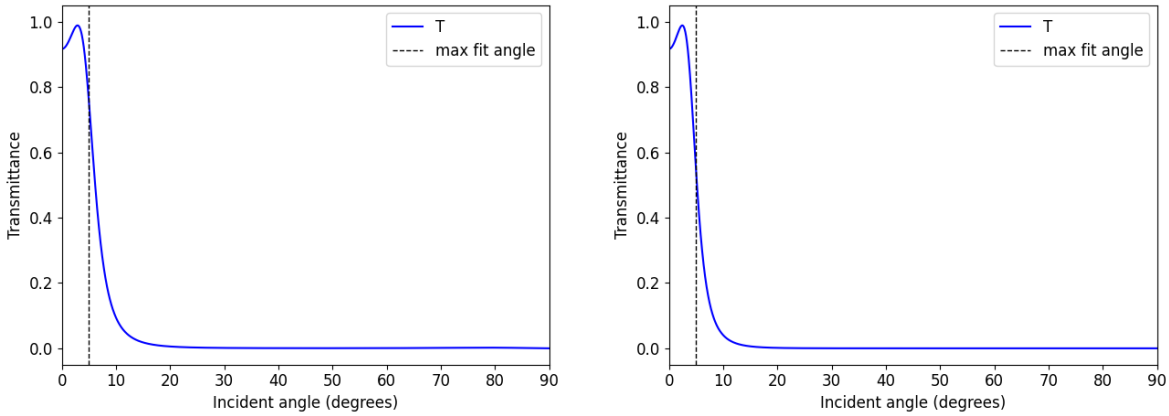

(a) Transmission intensity for p-polarization

(b) Transmission intensity for s-polarization

Figure 3.19: Transmission intensity of angular stray light filter design with 24 layers, with $\bar{T_p} = 0.9352$ and $\bar{T_s} = 0.8915$.

As these transmission intensity plots show, the cut-off at the maximum acceptance angle is not an absolute step from T = 1 to T = 0. Instead, a small angular range is needed to transition between high and low transmission intensity. Ideally, an application of this filter would be a system where the maximum incidence angle of the desired light is 5 degrees or lower, but the angular stray light to be filtered only occurs at higher angles, effectively allowing for a tolerance region in the application requirements. Increasing the size of the tolerance region likely increases the performance of the filter. The contrast versus tolerance region size of the non-periodic and periodic designs is shown in figure 3.20.

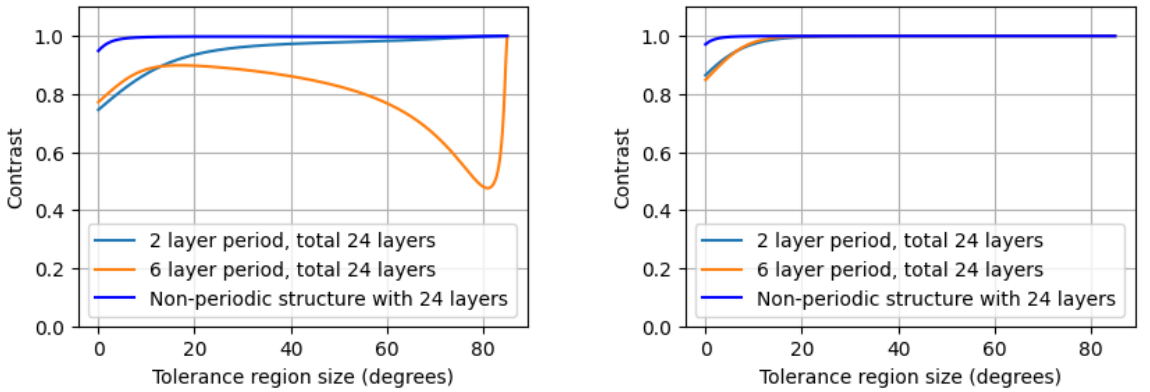

(a) Contrast versus tolerance region size for p-polarized light

(b) Contrast versus tolerance region size for s-polarized light

Figure 3.20: Contrast vs tolerance region size of 24-layer angular stray light filter designs.

The tolerance region size ranges from 0 to 85 degrees, since it needs to fit between $\theta_{max} = 5$ and 90 degrees. These plots show that contrast is only very slightly worse overall in p-polarization in comparison to s-polarization, which can be explained by the fact that the transmission coefficient of p-polarized light at an interface is always larger than that of s-polarized light at the same incoming angle. This difference becomes more clear when plotting the transmission intensity values in a log scale, like in figure 3.21.

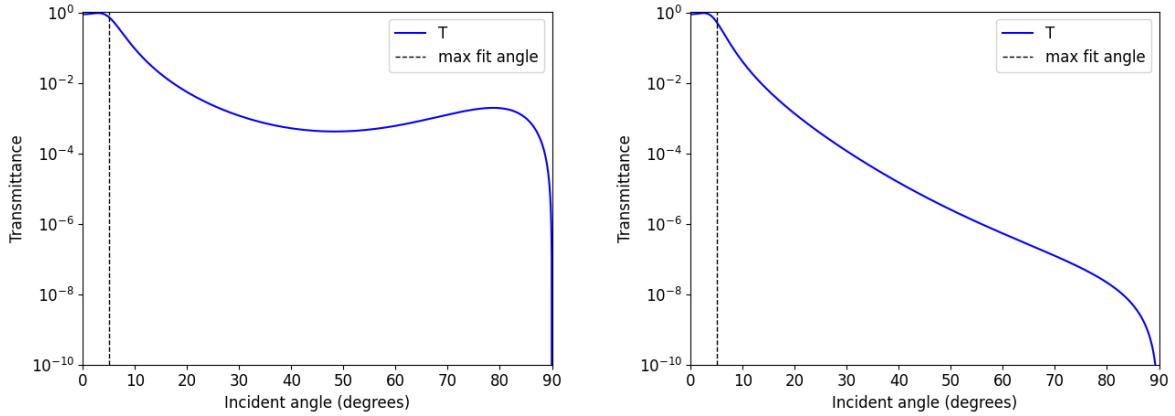

(a) Transmission intensity for p-polarization

(b) Transmission intensity for s-polarization

Figure 3.21: Transmission intensity of the same design as shown in figure 3.19, with a log scale to show the actual attainable values.

Interesting behavior shows when plotting the suppression ratio versus tolerance region size instead, as shown in figure 3.22. For p-polarized light, the suppression ratio starts going down at a tolerance region size of approximately 27 degrees, after which it shoots back up after a tolerance region size of approximately 65 degrees. This is due to the increase in transmission intensity around 65 degrees for p-polarized light. However, since the expected applications would probably need a tolerance region size lower than 65 degrees, this effect seems trivial.

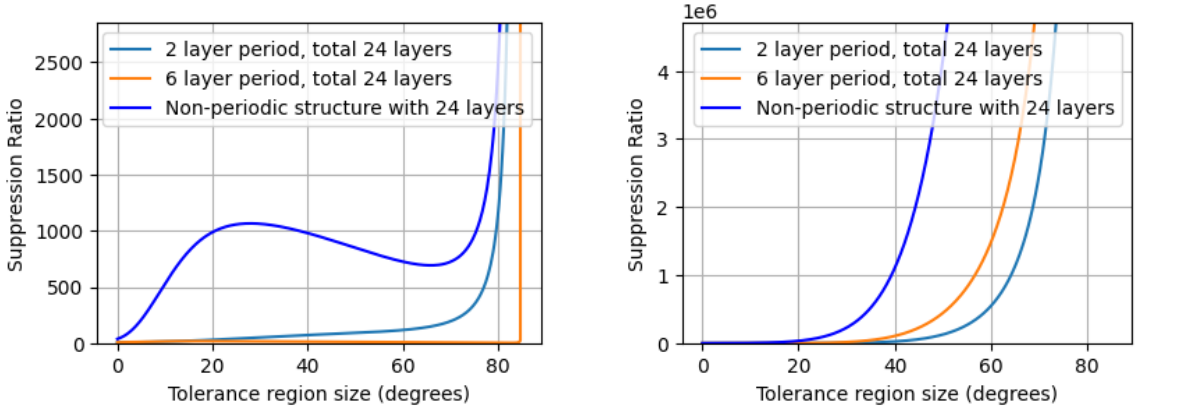

(a) Suppression ratio versus tolerance region size for p-polarized light

(b) Suppression ratio versus tolerance region size for s-polarized light

Figure 3.22: Suppression ratio vs tolerance region size of 24-layer angular stray light filter designs.

With angular stray light filters, just as with spaceplate action before, the sensitivity toward precision errors is important to consider. Therefore, 200 samples of each of the considered structures were generated and had defects introduced to their layer thicknesses. The defects were randomly generated according to a normal distribution around zero, with a given standard deviation. The resulting contrast and suppression ratio (with a tolerance region size of zero) depending on precision error can be seen in figure 3.23. From these plots, it is clear that the suppression ratio of the non-periodic angular stray light filter remains better than that of periodic solutions. However, the contrast versus precision plot shows that the non-periodic mean contrast goes lower than the periodic ones. This is likely due to the fact that at lower values of $\bar{T_w}$, contrast will go down quicker than suppression ratio. Still, the area around the mean shows a possibility of structures that still outperform the periodic ones at standard deviations of layer thicknesses above 4 nanometers.

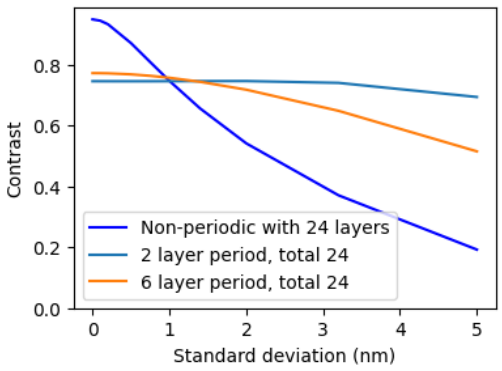

(a) Contrast vs standard deviation for p-polarized light

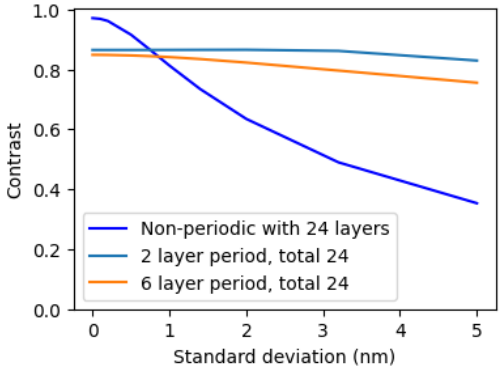

(b) Contrast vs standard deviation for s-polarized light

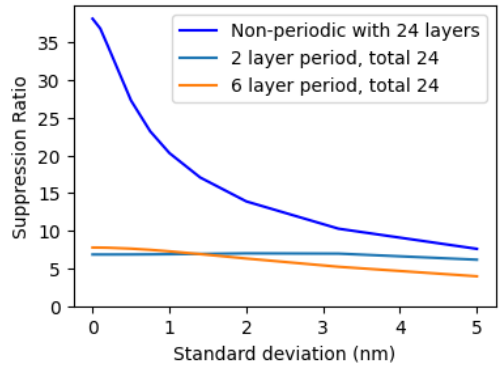

(c) Suppression ratio vs standard deviation for p-polarized light

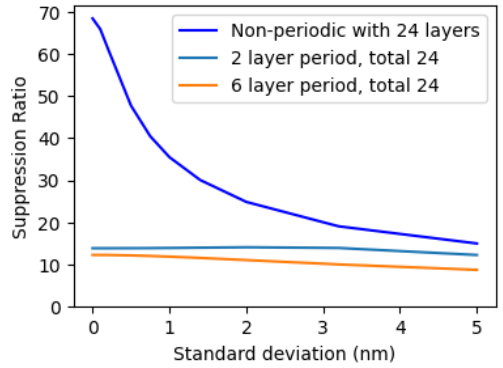

(d) Suppression ratio vs standard deviation for s-polarized light

Figure 3.23: Contrast and suppression ratio versus standard deviation of intended layer thicknesses of 24-layer angular stray light filter designs. Each plot shows the mean value as a line, with one standard deviation indicated by the surrounding color.

By assuming that it is allowable that only a certain percentage of the products of manufacturing make the cut, one can select the best samples. Taking the 90th percentile of all samples plotted previously shows what would happen if only the best 10 percent of produced filters are considered. The results of this are shown in figure 3.24. This shows that the non-periodic structure can outperform periodic structures if production losses are accepted.

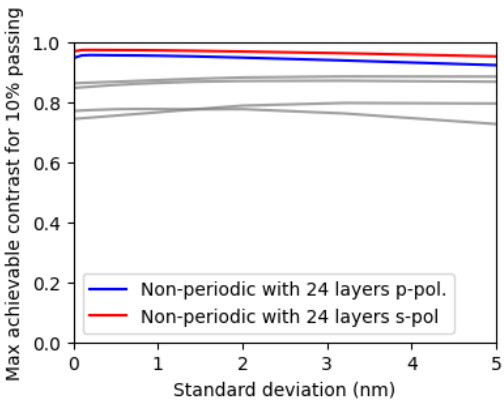

(a) Average contrast of best 10% of defect structures versus standard deviation of layer thicknesses

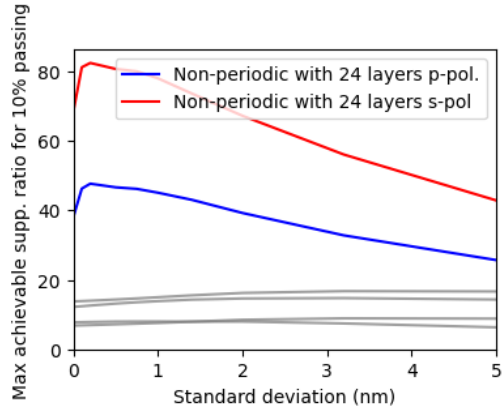

(b) Average suppression ratio of best 10% of defect structures versus standard deviation of layer thicknesses

Figure 3.24: Average contrast and suppression ratio of the best 10% of defect structures, in which all non-labeled gray lines are the results from the periodic devices, with no permitted tolerance region.

Reviewing the transmission intensity data of these selected defect structures shows in figure 3.25 that the average remains above 0.5, meaning they could feasibly be used in real applications.

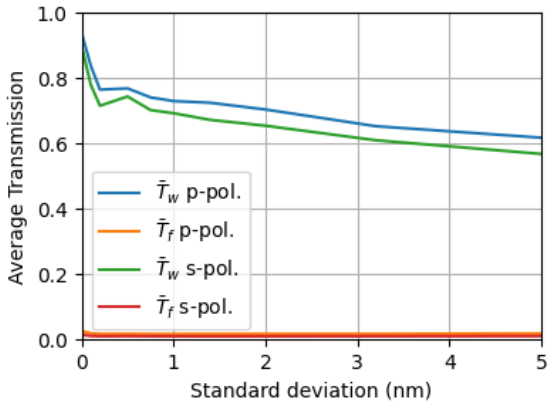

Figure 3.25: Average $\bar{T}_w$ and $\bar{T}_f$ from best performing 10% of defect structures in terms of contrast.

Also noteworthy, though not explored further in this thesis, is the difference in transmission intensity over a broader spectrum of wavelengths. Figure 3.26 shows that the non-periodic angular stray light filter only allows transmission for a few select wavelength ranges, while the periodic filter allows transmission in a relatively broad wavelength band. This implies the possibility of also using non-periodic filters to filter out other wavelengths. This could be an added functionality, if an application calls for it. However, at oblique angles a small range of wavelengths lower than the intended wavelengths will still have a nonzero transmission due to the curve of the transmissive band.

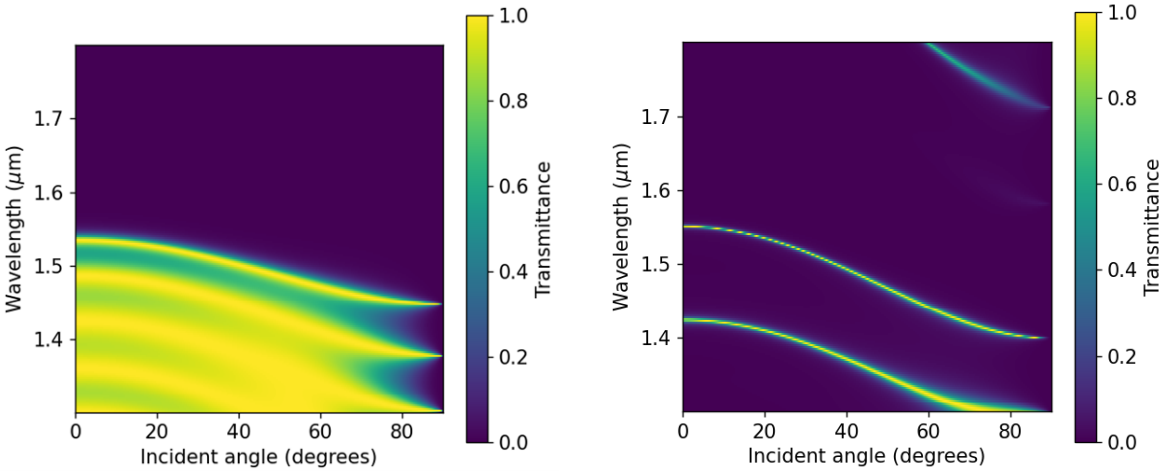

(a) Transmission intensity spectrum of periodic filter of 24 layers with 2 layer period (orange line in previous plots).

(b) Transmission intensity spectrum of the non-periodic filter of 24 layers.

Figure 3.26: The transmission intensity of the periodic and non-periodic filter depending on wavelength and incoming angle, displaying a very different distribution depending on periodicity.

3.4.2. Unintended spaceplate action

When evaluating the transmitted phase profile, an unexpected correlation emerges. It appears as if any time a thin film stack has the desired transmission intensity profile, spaceplate action is automatically guaranteed. The phase fits of the specific angular stray light filter discussed in the previous sections can be seen in figure 3.27. In the region of high transmission, the phase profiles of the filter almost perfectly coincide with the scaled free space propagation phase profiles.

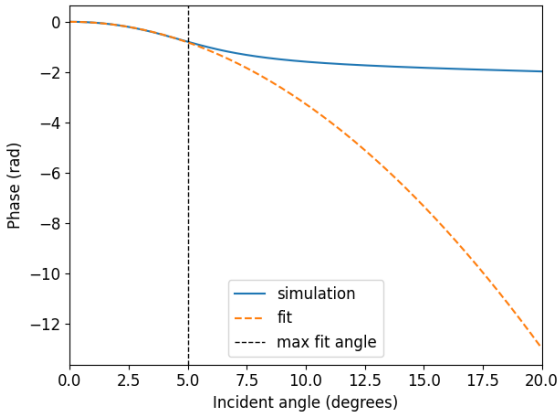

(a) Phase fit of simulated phase profile for p-polarized light

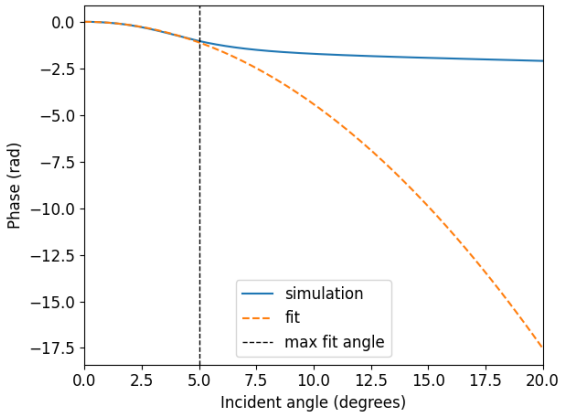

(b) Phase fit of simulated phase profile for s-polarized light

Figure 3.27: Phase fit of simulated phase profile for both polarizations, with a compression ratio for p- and s-polarized light of 9.9533 and 13.4485 and Strehl ratios 0.9947 and 0.9816 respectively.

To ensure this is not a fluke, this behavior was also analyzed for a angular stray light filter with $\theta_{max} = 30$. This also shows a very decent match of the phase within the optimized angular range. Interestingly, the compression factor of this filter is very close to 1. This is somewhat consistent with the relation implied by figure 3.7 in section 3.2, of having lower compression ratios for larger θ_{max}.

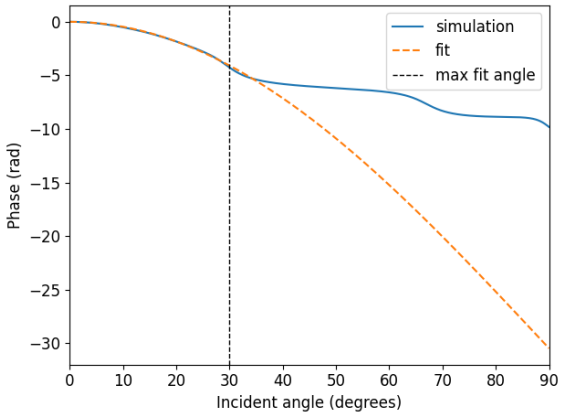

(a) Phase fit of simulated phase profile for p-polarized light

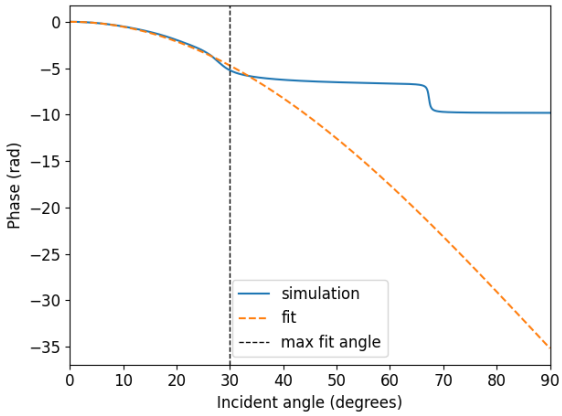

(b) Phase fit of simulated phase profile for s-polarized light

Figure 3.28: Phase fit of simulated phase profile for both polarizations, with a compression ratio for p- and s-polarized light of 1.0155 and 1.1726 and Strehl ratios 0.9566 and 0.8576 respectively.

Lastly, to ensure it is not an artifact or bug of some sort in the optimization code, a random structure was generated with layer thicknesses between 150 and 300 nm and its transmission intensity depending on wavelength was reviewed, after which a wavelength was chosen for which it could technically function as an angular stray light filter. Its transmission intensity and phase fit for p-polarized light can be seen in figure 3.29. The transmission intensity profile shows some high values at higher angles, since no optimization was performed on either phase or transmission of the structure.

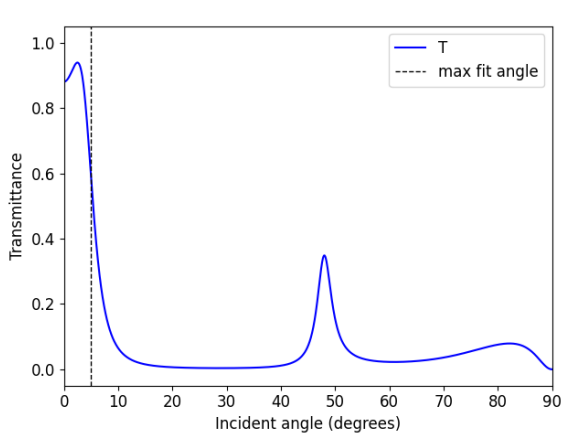

(a) Transmission profile of a random structure for p-polarized light

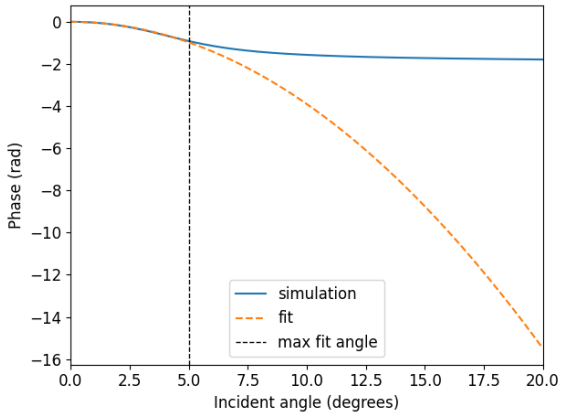

(b) Phase fit of simulated phase profile of random structure for p-polarized light

Figure 3.29: Transmission properties of a random structure for p-polarized light at a wavelength of 1474 nm, with compression ratio of 12.1602 and Strehl ratio of 0.9846.

In an attempt to find the cause of this phenomenon, the phase behavior of general thin film stacks is evaluated here. To derive the phase dependent on incoming angle of light transmitted through an arbitrary thin film structure, one can attempt using the Bloch wavenumber K. As mentioned in section1.5, within photonic bands, K is a real number, which as a result means that the transmission phase dependent on ω and k_y is equal to $K\Lambda$, where $k_y = k_{tv}$ is the magnitude of the transversal component of angular wave vector $\mathbf{k}$. Important to realize is that this is equivalent to saying the phase dependent on wavelength λ and incoming angle θ, since $\omega = \frac{2\pi}{c}$ and $k_0 \sin\theta = k_y$. Then, taking a non-periodic thin film structure as simply being a single period of a structure (meaning the thickness of the structure equals Λ) and assuming the relevant angular and wavelength range to be within a photonic band, the phase of transmitted light through that structure can be written:

$$\varphi = K(\lambda, k_y)\Lambda \tag{3.7}$$

Expanding K around $k_y = 0$ can lead to a parabolic phase at small angles (i.e. small k_y), which is required to construct a spaceplate:

$$K(\lambda, k_y) = K(\lambda, 0) + \frac{1}{2}K''(\lambda, 0)k_y^2 + \mathcal{O}(k_y^4) \tag{3.8}$$

Then assuming small angles, one can formulate the phase relationship for a spaceplate:

$$k_z d_{eff} + \varphi_{global} \approx k_0 d_{eff} - \frac{k_y^2}{2k_0} d_{eff} \approx K(\lambda, 0)\Lambda + \frac{1}{2}K''(\lambda, 0)k_y^2\Lambda \tag{3.9}$$

Only taking non-global phase components, meaning the ones dependent on incoming angle, this allows one to find the approximate compression factor:

$$-\frac{k_y^2}{2k_0} d_{eff} \approx \frac{1}{2}K''(\lambda, 0)k_y^2\Lambda \tag{3.10}$$

$$R \approx -K''(\lambda, 0)k_0 \tag{3.11}$$

This implies that for small angles, any structure that operates within a photonic band for a certain angular and wavelength range will mimic free space, just as a spaceplate would, within that same range. However, just from these equations, there is no guarantee that R will be larger than one, and so it does not guarantee that a thin film structure operating within a photonic band will make it a good compressive spaceplate for that regime. One could try to find it through finding a formula for $K''(\lambda, 0)$ but this is a variable dependent on a series of matrices, which makes it very hard to do analytically, and still won't help in finding whether there is a fundamental rule at work here.

There is also a somewhat intuitive way the compressive spaceplate behavior could be explained, though it is very far from being a rigorous proof. Whenever a thin film structure successfully transmits light, this implies there is a state in which the electromagnetic wave can sustain itself within the structure through a (near) resonant state.

Whenever such a state is reached, it automatically means many reflections must occur inside the thin film structure itself, as these reflected waves are necessary to uphold the resonance. Considering only a single film for the moment, the situation is like what is shown in figure 3.30. When the outgoing rays experience a path length difference equal to $j\pi$ with j an integer number, they are able to constructively interfere with one another, effectively adding them up. Using the assumption that the location of the observed outgoing beam would then be at the center of energy of the constructively interfering beams, one could interpret this as a lateral shift of the center of the transmitted beam in regards to the incident beam. This lateral shift, as described in figure 1.1 in the introduction, is the reason a spaceplate can compress space.

Figure 3.30 only shows the result of transmission through a single layer, and so most of the transmitted energy is most likely in the least shifted beam (since $|t| < 1$ and $|r| < 1$), making the lateral shift quite small. However, when multiple layers are stacked atop one another, more internal reflections of will occur, which will result in a bigger lateral shift of the center of energy of the beam. This may offer an intuitive explanation of why angular stray light filters with a certain highly transmissive angular regime also automatically attain compression ratio significantly higher than 1. However, as said before, no actual formula or rigorous analytical explanation has yet been found to pinpoint the exact relation.

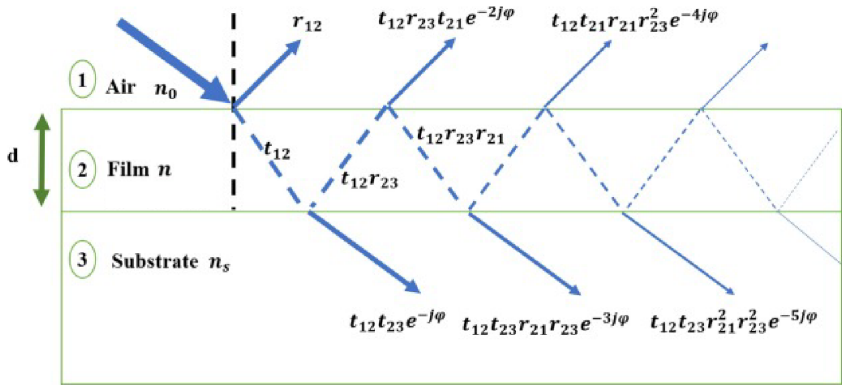

Figure 3.30: Transmission through single thin film where incoming field at interface is taken to be 1 and φ signifies phase accumulated when crossing the film once. Image adapted from Tchenka et al., 2024.

3.4.3. Accounting for polarization dependent compression

Since angular stray light filters automatically compress space, once again, polarization dependent compression factors need to be taken into account when designing a angular stray light filter. This is not focusing on good spaceplate action with high compression numbers and perfectly shaped phase profiles, but instead on matching the distance experienced by both p- and s-polarized light traveling through the filter and this way ensure polarization independence. By optimizing for this, and the same parameters as before, one can again plot the maximum contrast found, versus the number of layers in the structure, which is shown in figure 3.31. The contrast reached using this extra requirement is generally slightly lower, which is to be expected since angular stray light filtering was no longer the sole priority in the optimization algorithm. Still, for structures with less than 25 layers, the non-periodic filters are shown to perform better than the periodic ones.

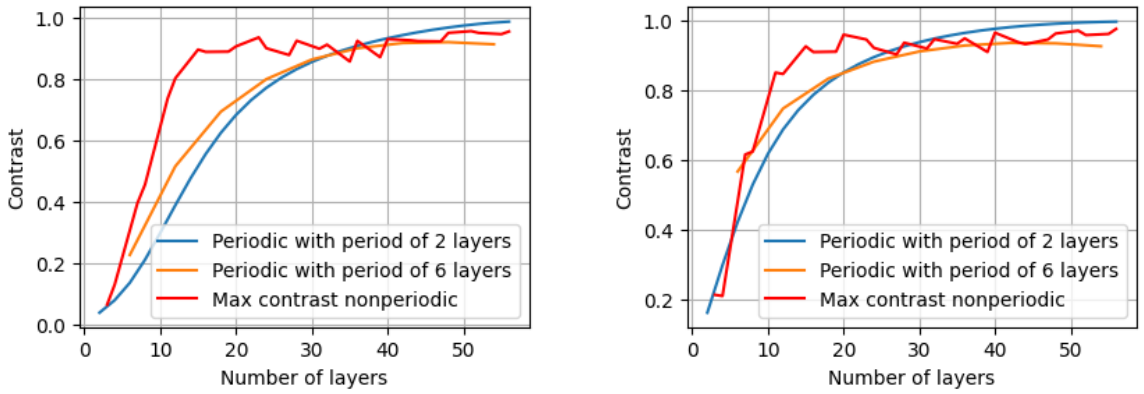

(a) Max contrast for p-polarization

(b) Max contrast for s-polarization

Figure 3.31: Maximum contrast found versus number of layers in the structure, optimized with tolerance region size of 0.5 degrees and with matching effective distances for p- and s-polarized light.

Using the previous plot, a angular stray light filter was chosen with 20 layers. At 20 layers, there is still a significant difference in performance of the different filters, and the periodic solutions with periods of 2 and 4 layers can both compare fairly at 20 layers as well since 20 is divisible by 2 and 4. The chosen filter displayed compressive behavior, with a compression ratio for p-polarization of 7.6437 and one for s-polarization of 7.6314, with the structure itself being 4.01 μm thick. The Strehl ratios for p- and s-polarized light were equal to 0.9989 and 0.9993 respectively. The resultant shift in experienced effective distance was 0.05 μm. Its transmission intensity profile can be seen in figure 3.32.

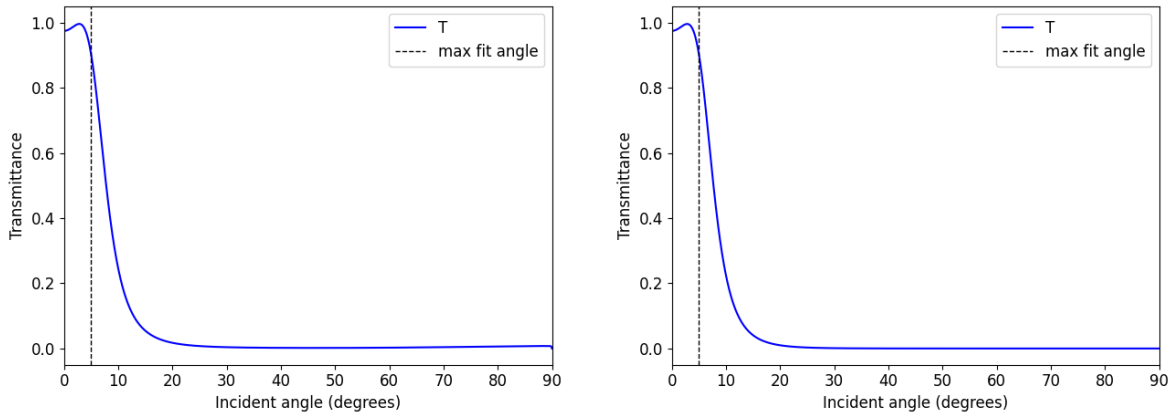

(a) Transmission intensity for p-polarization

(b) Transmission intensity for s-polarization

Figure 3.32: Transmission intensity of angular stray light filter design with 24 layers, with $\bar{T_p} = 0.9352$ and $\bar{T_s} = 0.8915$.

Repeating the same plots as for the filter in section 3.4.1, shows this filter has very similar properties. The contrast and suppression dependent on tolerance region size for both polarizations both still show a well-performing angular stray light filter, as can be seen in figures 3.33.

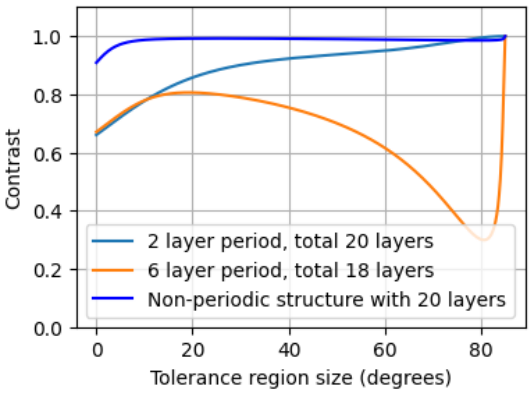

(a) Contrast vs tolerance region size for p-polarized light

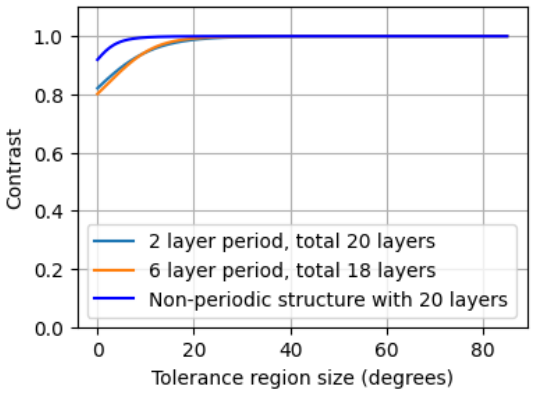

(b) Contrast vs tolerance region size for s-polarized light

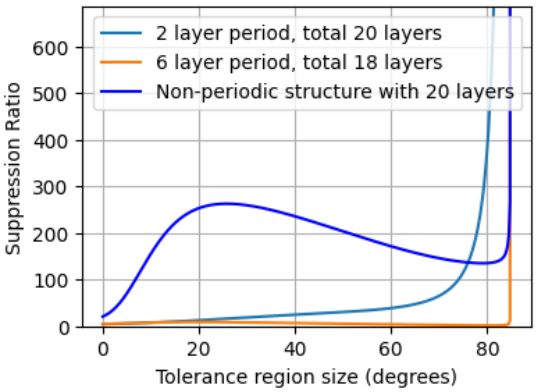

(c) Suppression ratio vs tolerance region size for p-polarized light

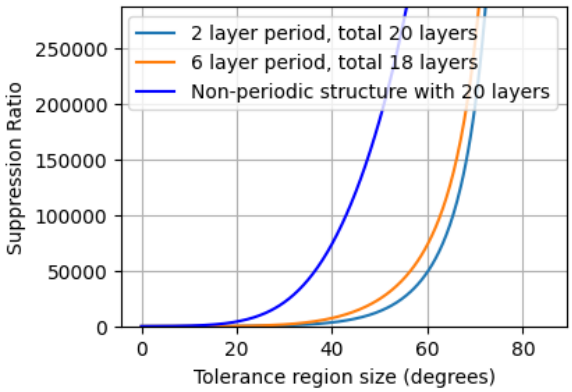

(d) Suppression ratio vs tolerance region size for s-polarized light

Figure 3.33: Contrast and suppression ratio versus tolerance region size for 20-layer angular stray light filter designs.

Taking, once again, the best 10 percent of produced filters from 200 samples in which defects were introduced using a normal distribution, this filter still proves to be outperforming its periodic counterparts, as shown in figure 3.34. However, the constraint of matching polarizations did significantly lower the contrast in comparison to the filter of section 3.4.1, even when accounting for the difference in the number of layers.

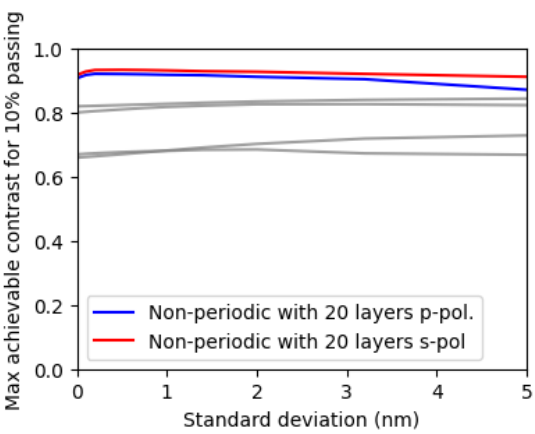

(a) Contrast of best 10% of defect structures versus standard deviation of layer thicknesses

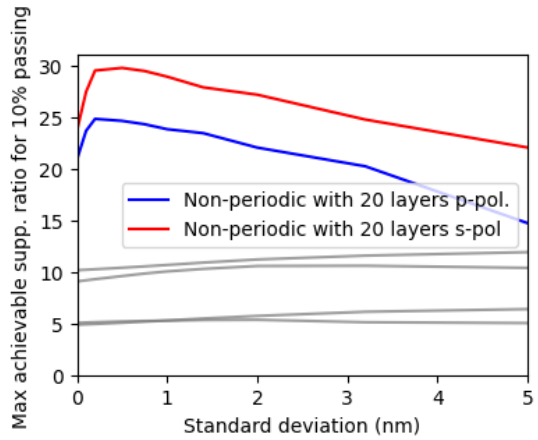

(b) Suppression ratio of best 10% of defect structures versus standard deviation of layer thicknesses

Figure 3.34: The result of choosing the best 10% of defect structures, in which all non-labeled gray lines are periodic solutions.

Once again reviewing the resulting transmission intensity values shows that these structures have average transmission intensities above 0.5 as shown in fig 3.35 which points to a reasonable feasibility for real life applications.

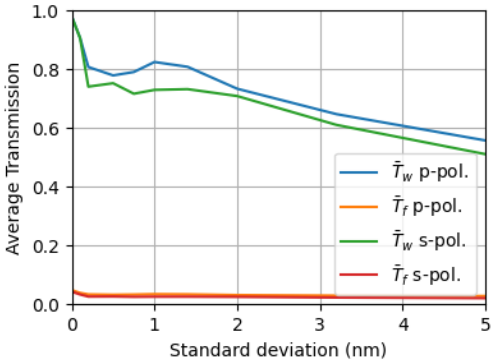

Figure 3.35: Average $\bar{T}_w$ and $\bar{T}_f$ from best performing 10% of defect structures in terms of contrast.

3.5. Multifunctional spaceplates

As the previous section shows, it is possible to create spaceplates which have both stray light filtering properties and a decent compression ratio. These would be a different type of multifunctional spaceplates than those shown by Shao et al., 2024 which are discussed in section 1.4. However, since the transmitted phase profiles of the structures was not consciously optimized to fit perfectly, it may be possible still to improve upon the phase fit. This may be done by adding back the term for phase fitting ($w_{fit}\sigma_{fit}$) into the figure of merit (FOM). The resulting maximum contrast dependent on the number of layers can be seen in figure 3.36. This still shows that the non-periodic filter is significantly better than the periodic counterparts at a number of layers below 25. However, due to the added constraint in the optimization algorithm, the values have once again shifted down slightly.

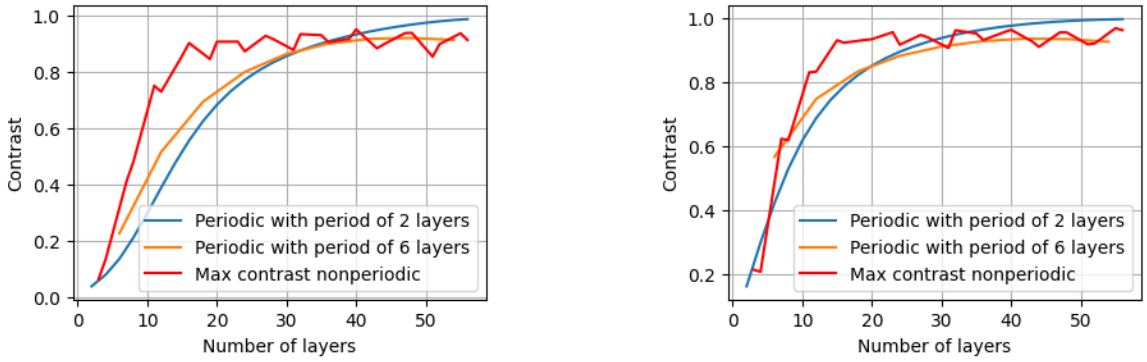

(a) Max contrast for p-polarization

(b) Max contrast for s-polarization

Figure 3.36: Maximum contrast found versus number of layers in the structure, optimized with tolerance region size of 0.5 degrees, for matching effective distances between polarizations and a good phase fit.

By focusing, once again, on the best performing structure with 20 layers, the transmitted phase and intensity for each polarization of this structure are shown in figure 3.37:

Strangely, this spaceplate does not outperform the one shown in section 3.4.3, neither in its Strehl ratio nor in the difference of effective distance. It appears adding the constraint only made the optimization landscape more complex, while similar or better results are achievable solely by optimizing for good transmission. However, if one wants to optimize to get close to a desired compression factor R, then optimizing for the specific phase parabola may still prove fruitful.

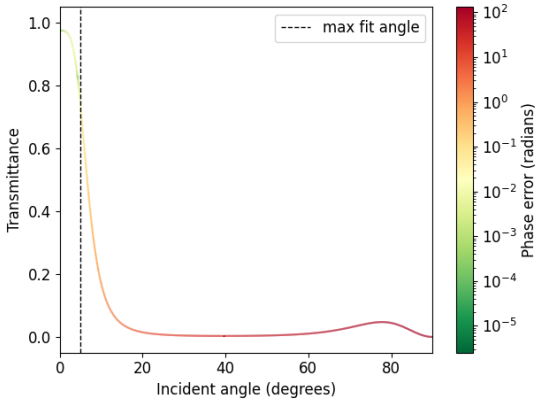

(a) Transmission intensity for p-polarized light

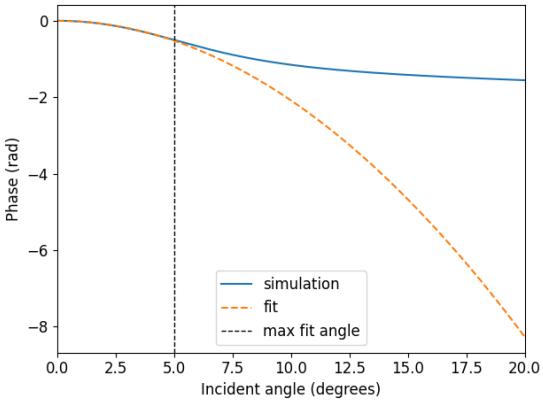

(b) Transmitted phase for p-polarized light

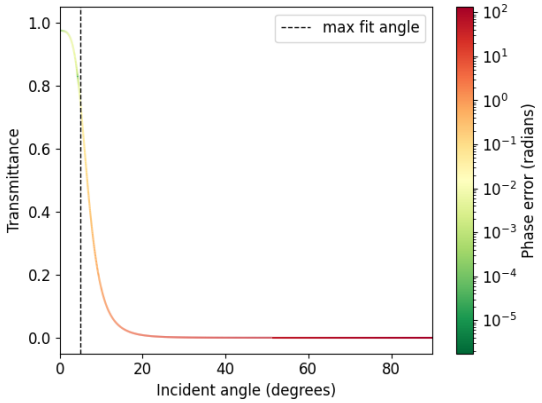

(c) Transmission intensity for s-polarized light

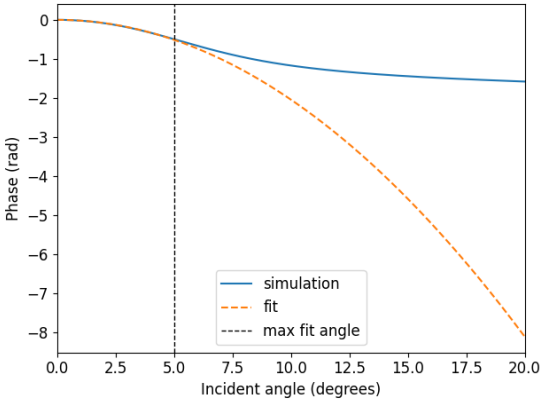

(d) Transmitted phase for s-polarized light

Figure 3.37: Transmitted intensity and phase profiles with compression ratios of 6.8713 and 6.7331 and Strehl ratios of 0.9943 and 0.9955 for p- and s-polarized light respectively, and a thickness of 4.92 μm resulting in a difference of d_{eff} of 0.02 μm.

4

Conclusions and outlook

Successful implementation of physical principles

Part of this thesis work included implementing the numerical side of the methods named in chapter 2 in python code. In the case of transfer matrix methods, the characteristic method was already successfully implemented by J. Pagé and Reshef, 2021, and was independently validated by implementing the Fresnel approach and comparing results. The optimization protocol and evaluation protocols for all designs were also rewritten specifically for this thesis, as was part of the plotting infrastructure. Lastly, the numerical implementation for plotting photonic bands was also created for this thesis. The code is available upon reasonable request to the author.

General properties of thin film spaceplates

This thesis has shown using simulations that spaceplates made by optimizing thin film structures have certain properties. Firstly, as expected from the formulation of the limits as in section 1.3, at higher numerical apertures, the achievable compression ratio lowers significantly. This also implies that achieving the same effective distance with a spaceplate at higher numerical apertures requires significantly more layers, making their manufacturing increasingly difficult. The results also show that it is technically possible to design a multilayer thin film spaceplate in such a way that the effective distance is, to a certain extent, the same for both p- and s-polarized light. This indicates polarization independent spaceplates are possible using this design approach.

Another property displayed by the spaceplates in this thesis is that added requirements almost always led to worse performance with respect to the original optimization targets. This, however, may not be a general property of thin film spaceplates themselves, instead being caused by a more complex optimization space with different local optima. Still, when doing inverse design through optimization like this, adding requirements will usually worsen the performance overall, which should be considered before using this design methodology.

Maximizing theoretical effective distances

The results of the simulations where single spaceplates are repeatedly stacked seem to indicate some practical possibilities. Firstly, they show that under ideal manufacturing conditions, assuming no layer thickness deviations or other defects, effective distances of a few centimeters are achievable for the chosen parameters while retaining a Strehl ratio above 0.8, meaning diffraction will generally limit image resolution more than introduced aberrations. These simulations show that transmission intensity within the desired angular range does not have to suffer from repeating the structure in this way, and neither does the compression factor.

Secondly, the results seem to indicate that there are some properties which makes the RMSE of the phase profile increase at different rates with the number of repetitions. This could be a combination of the quality of the unit cell phase fit, variance of layer thickness, or potential other factors yet to be identified. Pinpointing these properties or blindly optimizing by writing an evaluating function for the behavior may still improve the largest reachable effective distance assuming perfect manufacturing.

In general, this shows that this strategy of repeating a spaceplate design is a decent way to extend the theoretical effective distance of the structure.

Maximum effective distances considering manufacture

As soon as defects of reasonable size are introduced (say, $\geq$1 nm), the big difference in achievable effective distance observed between designs in the perfect manufacturing case is significantly reduced. The thin film structures are very susceptible to precision errors, and the bigger the error, the less important the initial base structure properties become in the eventual effective distance reached. Achieving manufacturing errors smaller than 0.5 nm across thousands of layers thicker than 100 nm is extremely difficult Hattrick-Simpers et al., 2019 and so from these results can be concluded that physical spaceplates using thin film multilayer structures with a half-angle of 5 degrees will probably not reach effective distances much larger than a millimeter. However, possible applications at such effective distances may still be feasible, such as in small cameras (Peng, 2013, Steinich and Blahnik, 2012) and microlens arrays for 3D-imaging (Yuan et al., 2018).

In conclusion, for single wavelength operation, thin film spaceplates show some promise, especially for applications with needed effective distances <1 mm and with low numerical apertures.

Manufacturing error representation

The introduced manufacturing errors in this thesis are not completely consistent between sections. At the different sections discussing manufacturing errors (sections 3.3.3 and 3.4) two different distributions were used to represent defects in the layer thicknesses. In the first, a uniform distribution was used. The decision to use a uniform distribution was made early in the project and reconsidered only after most simulations had already been completed. In the latter case, the error distribution was changed to a normal distribution, which should more accurately represent the distribution of manufacturing errors that can occur in real life. Unfortunately, due to time constraints, the first of the two could not be redone with a normal distribution, and is therefore a less realistic model of actual manufacturing processes. However, the results still give an idea of the effect of a manufacturing error on the properties of the spaceplates, and were kept in the thesis report to illustrate general trends. Should this particular study very much be of interest, then repeating it for a normal distribution is advisable.

Even with a normal distribution however, the errors presented in this thesis still cannot fully represent real manufacturing processes. In reality, manufacturing errors would not solely be uniform thickness variations along the entire film. Instead, manufacturing errors exist in three dimensions, and can be started by dust particles getting caught and those defects propagating through subsequent layers or by local differences in relevant variables like local temperature, local deposition rates, and other factors. Further research into error tolerances is advisable if these structures are to be produced, especially if they require many layers. This could be done both in simulations and through physical experimentation.

Angular stray light filtering

The results of the exploration into monochromatic angular stray light filtering strongly suggest there are situations in which a non-periodic, optimized structure will have better angular stray light filtering properties than a periodic one with the same amount of layers, both in terms of contrast and suppression ratio. Even when defects of a reasonable size (>3 nm) are introduced, the top ten percent of the non-periodic solutions consistently outperform their periodic counterparts. Therefore, more research into this specific application of optimized non-periodic thin film structures should be performed.

Additionally, when examining the spectral response difference between periodic and non-periodic angular stray light filters, the simulations showed a higher selectivity in wavelength by the non-periodic solution. This was not further explored in this thesis, but may point to an extra possible functionality of these structures as spectral filters.

Lastly, an effect was observed where optimizing for a high transmission intensity in a certain angular range starting at normal incidence will automatically give it a phase profile which satisfies the conditions for a spaceplate with a compression factor significantly greater than one within that same angular range. Since no rigorous analytical explanation has yet been found for this behavior, it should be studied more extensively in order to get a greater understanding of thin film spaceplates.

Multifunctional spaceplates

The results of this thesis definitively show that polarization independent spaceplates which also act as angular stray light filters are a viable option, at least theoretically. They are able to compress space with effective distances in the μm range for low numerical apertures (i.e. small θ_{max}) and at a single wavelength, while also filtering out transmission at higher incoming angles. Furthermore, figure 3.26 seems to suggest further optimization of filtering capabilities may be possible, specifically filtering out a limited range of wavelengths around the desired band. This could lead to a spaceplate with two different added filtering functions. Whether these functions could also be combined with those talked about in Shao et al., 2024 is a topic which demands further research.

Metasurfaces

The technique discussed in this thesis was to make a spaceplate using thin film layers, and in that way manipulate the transmitted phase profile. Multilayer thin film structures only allow for variations in material choice, layer thicknesses, and numbers of layers. However, as mentioned in chapter 1, it is possible to manipulate the properties of the transmitted electric field with metasurfaces, which have an explicitly designed 2D geometry, which significantly expands the available design space.

Furthermore, combining thin film spaceplates or even metasurface spaceplates (like those discussed in section 1.2.5) may open up more possibilities for fully monolithic optical systems.

Optimization limitations

There are a few limitations inherent to using optimization processes for design. First of all, the optimization itself operates solely based on the objective functions and constraints defined by the designer. The consequence of this is that the input parameters can be tweaked and chosen precisely to attempt to get the best result for a given situation. One could even try to optimize the input parameters themselves by doing multiple runs with different inputs and evaluating the performance of the different designs. This has not been attempted in this study, but may still yield better results than have been shown here.

Secondly, it is within the nature of optimization algorithms on landscapes with many local optima that one can not be completely certain that a global optimum is reached. In the case of the optimizations done in this thesis, it is likely that the global optimum was not reached, due to a large optimization space with as many dimensions as there are layers, which cannot feasibly be fully explored with the available computing power. Therefore, better solutions most likely exist for most of the structures shown in this thesis. However, the shown structures usually are already handpicked from a batch of optimization attempts, and therefore it is assumed that they are somewhat close to the global optimum for their specific input parameters.

Lastly, the scientific field of optimization is quite big and complex, and many different algorithms could have been applied to optimize the given problems. The choice was made here to use optimization techniques which are still relatively simple, and in the end only two optimization steps were used; particle swarm optimization for a global search followed by the Fletcher-Reeves conjugate gradient method to refine the found optimum. Whether or not other techniques could be more successful is not certain, and may still deliver improvements.

Periodic angular stray light filter representation

The periodic representations of angular stray light filters were not optimized using a true ”infinite” amount of layers. The situation called for a representation of periodic structures and simulating repeated structures and optimizing those was already very convenient due to pre-existing code, but optimizing using a theoretical infinite periodic structure is possible through Bloch theory, like that shown in section 1.5 and appendix A. Using this method may still result in better periodic solutions than those shown in this thesis and could hence be worth exploring.

Situational statements

Many of the statements made in this thesis can only be applied to real situations as long as they occur under the conditions matching those in the simulations present in this study. For instance, non-periodic angular stray light filters have only been found to be better than the periodic solution when using the layer thickness boundaries of 150 to 300 nm for both structures, and only at certain numbers of layers. This means that applying this knowledge to a known application will require a repeat of this study for

the situation at hand, and may have different results. However, though situational, the study still shows that this may be worth the effort, like in the given example.

Additionally, many of the spaceplates in this thesis, and also in the literature, are designed for operation on either p- or s-polarized light, but not on both at the same time. When one imagines a cone-shaped focusing beam of light onto a surface (such as one resultant of a parallel beam going through a typical focusing lens), a simple linear polarizer would be insufficient to ensure the correct polarization state at that surface. The needed polarization state is either radial or azimuthal polarization, for which polarizers do exist (Edmund Optics, n.d.), though they can be rather costly. One should take this into account when designing a spaceplate for their own application, which is also why the added interest in polarization independence existed in this thesis.

Final remarks

This thesis demonstrates both the potential and the limitations of designing multilayer thin film spaceplates using inverse design through optimization techniques. While achieving large effective distances remains a significant manufacturing challenge, the simulations suggest that distances of up to several centimeters may be theoretically attainable. Moreover, the combination of angular stray light filtering with spaceplate functionality appears promising, warranting further research in this direction.

Bibliography

Arbabi, A., & Faraon, A. (2023). Advances in optical metalenses. *Nature Photonics*, *17*(1), 16–25. https://doi.org/10.1038/s41566-022-01108-6

Born, M., & Wolf, E. (1999). *Principles of optics: Electromagnetic theory of propagation, interference and diffraction of light* (7th). Cambridge University Press. https://doi.org/10.1017/CBO9781139644181

Chen, A., & Monticone, F. (2021). Dielectric nonlocal metasurfaces for fully solid-state ultrathin optical systems. *ACS Photonics*, *8*(5), 1439–1447. https://doi.org/10.1021/acsphotonics.1c00189

Clerc, M. (2012). *Standard particle swarm optimisation* (tech. rep. No. hal-00764996) (Accessed: 24-11-2024). HAL Open Science. https://hal.science/hal-00764996

Danielzik, B., Heming, M., Krause, D., & Thelen, A. (2003). Overview — thin films on glass: An established technology. In H. Bach & D. Krause (Eds.), *Thin films on glass* (pp. 1–21). Springer Berlin Heidelberg. https://doi.org/10.1007/978-3-662-03475-0_1

Darrigol, O. (2012). *A history of optics from greek antiquity to the nineteenth century*. OUP Oxford.

Díaz-Fernández, F. J., Máñez-Espina, L. M., Díaz-Rubio, A., & Asadchy, V. (2024). Broadband transparent huygens' spaceplates. *npj Nanophotonics*, *1*(1), 30. https://doi.org/10.1038/s44310-024-00025-6

Edmund Optics. (n.d.). *Radial polarization converters* [Accessed: 2025-06-15]. https://www.edmundoptics.com/f/radial-polarization-converters/14901/

Gerken, M., & Miller, D. A. B. (2005). Limits on the performance of dispersive thin-film stacks. *Appl. Opt.*, *44*(16), 3349–3357. https://doi.org/10.1364/AO.44.003349

Guo, C., Wang, H., & Fan, S. (2020). Squeeze free space with nonlocal flat optics. *Optica*, *7*(9), 1133–1138. https://doi.org/10.1364/OPTICA.392978

Hattrick-Simpers, J. R., Zakutayev, A., Barron, S. C., Trautt, Z. T., Nguyen, N., Choudhary, K., DeCost, B., Phillips, C., Kusne, A. G., Yi, F., Mehta, A., Takeuchi, I., Perkins, J. D., & Green, M. L. (2019). An inter-laboratory study of zn–sn–ti–o thin films using high-throughput experimental methods. *ACS Combinatorial Science*, *21*(5), 350–361. https://doi.org/10.1021/acscombsci.8b00158

Historiek.nl. (2024, September). Hans lippershey en de allereerste telescoop [Accessed: 12-06-2025]. https://historiek.net/hans-lipperhey-uitvinding-telescoop/121780/#gsc.tab=0

Horsley, S. A. R., Wu, J.-H., Artoni, M., & Rocca, G. C. L. (2014). Revisiting the bragg reflector to illustrate modern developments in optics. *American Journal of Physics*, *82*(3), 206–213. https://doi.org/10.1119/1.4832436

Joannopoulos, J., Johnson, S., Winn, J., & Meade, R. (2011). Photonic crystals: Molding the flow of light. In *Photonic crystals*. Princeton University Press.

Jones, J. (2018). Liquid crystal displays. In J. Dakin & R. Brown (Eds.), *Handbook of optoelectronics: Enabling technologies* (pp. 137–224, Vol. 2). CRC Press.

Kennedy, J., & Eberhart, R. (1995). Particle swarm optimization. *Proceedings of ICNN'95 - International Conference on Neural Networks*, *4*, 1942–1948 vol.4. https://doi.org/10.1109/ICNN.1995.488968

Mann, S. A., Sounas, D. L., & Alù, A. (2019). Nonreciprocal cavities and the time–bandwidth limit. *Optica*, *6*(1), 104–110. https://doi.org/10.1364/OPTICA.6.000104

Maxwell, J. C. (1865). Viii. a dynamical theory of the electromagnetic field. *Philosophical Transactions of the Royal Society of London*, *155*, 459–512. https://doi.org/10.1098/rstl.1865.0008

McKay, M. D., Beckman, R. J., & Conover, W. J. (1979). A comparison of three methods for selecting values of input variables in the analysis of output from a computer code. *Technometrics*, *21*(2), 239–245. Retrieved June 8, 2025, from http://www.jstor.org/stable/1268522

Mielenz, K. D. (1960). Tolerances for layer thicknesses in dielectric multilayer coatings and interference filters. *J Res Natl Bur Stand A Phys Chem*, *64A*(6), 487–495.

Miller, D. A. B. (2007). Fundamental limit to linear one-dimensional slow light structures. *Phys. Rev. Lett.*, *99*, 203903. https://doi.org/10.1103/PhysRevLett.99.203903

Miller, D. A. B. (2023). Why optics needs thickness. *Science*, *379*(6627), 41–45. https://doi.org/10.1126/science.ade3395

Moiseyev, N. (2011). *Non-hermitian quantum mechanics*. Cambridge University Press.

Monticone, F., & Alù, A. (2016). Invisibility exposed: Physical bounds on passive cloaking. *Optica*, *3*(7), 718–724. https://doi.org/10.1364/OPTICA.3.000718

Mrnka, M., Hendry, E., Láčík, J., Lennon, R. A., Barr, L. E., Hooper, I., & Phillips, D. B. (2022). Space squeezing optics: Performance limits and implementation at microwave frequencies. *APL Photonics*, *7*(7), 076105. https://doi.org/10.1063/5.0095735

Pagé, J., & Reshef, O. (2021). Inverse design spaceplate [GitHub repository, accessed September 7, 2024]. https://github.com/MagicIncubator/Inverse_Design_Spaceplate

Pagé, J. T. R., Reshef, O., Boyd, R. W., & Lundeen, J. S. (2022). Designing high-performance propagation-compressing spaceplates using thin-film multilayer stacks. *Opt. Express*, *30*(2), 2197–2205. https://doi.org/10.1364/OE.443067

Papalambros, P. Y., & Wilde, D. J. (2017). *Principles of optimal design: Modeling and computation* (3rd). Cambridge university press.

Pedrotti, F. L., Pedrotti, L. M., & Pedrotti, L. S. (2017). *Introduction to optics* (3rd ed.). Cambridge University Press.

Peng, X. (2013). Design of high pixel mobile phone camera lens. *Res. J. Appl. Sci. Eng. Technol*, *6*, 1160–1165.

Pfeiffer, C., & Grbic, A. (2013). Metamaterial huygens' surfaces: Tailoring wave fronts with reflectionless sheets. *Phys. Rev. Lett.*, *110*, 197401. https://doi.org/10.1103/PhysRevLett.110.197401

Qian, Q., Xu, C., & Wang, C. (2017). All-dielectric polarization-independent optical angular filter. *Scientific Reports*, *7*(1), 16574. https://doi.org/10.1038/s41598-017-16837-w

Reshef, O., DelMastro, M. P., Bearne, K. K. M., Alhulaymi, A. H., Giner, L., Boyd, R. W., & Lundeen, J. S. (2021). An optic to replace space and its application towards ultra-thin imaging systems. *Nature Communications*, *12*(1), 3512. https://doi.org/10.1038/s41467-021-23358-8

SciPy Developers. (n.d.). *Scipy.stats.qmc.latinhypercube* [Accessed: 2024-11-28]. https://docs.scipy.org/doc/scipy/reference/generated/scipy.stats.qmc.LatinHypercube.html

Shao, Y., Lupoiu, R., Jiang, J., Zhou, Y., Milster, T. D., & Fan, J. A. (2024). Multifunctional spaceplates for optical aberration correction. *ACS Photonics*, *11*(4), 1753–1760. https://doi.org/10.1021/acsphotonics.4c00086

Shastri, K., Reshef, O., Boyd, R. W., Lundeen, J. S., & Monticone, F. (2022). To what extent can space be compressed? bandwidth limits of spaceplates. *Optica*, *9*(7), 738–745. https://doi.org/10.1364/OPTICA.455680

Sorensen, N. J., Weil, M. T., & Lundeen, J. S. (2023). Large-scale optical compression of free-space using an experimental three-lens spaceplate. *Opt. Express*, *31*(12), 19766–19776. https://doi.org/10.1364/OE.487255

Steinich, T., & Blahnik, V. (2012). Optical design of camera optics for mobile phones. *Advanced Optical Technologies*, *1*(1-2), 51–58.

Tchenka, A., Agdad, A., & Ech-Chamikh, E. (2024). Determination of the thickness and optical properties by reflectance method. *Infrared Physics & Technology*, *137*, 105117. https://doi.org/10.1016/j.infrared.2024.105117

van den Bos, A. (2000). Aberration and the strehl ratio. *J. Opt. Soc. Am. A*, *17*(2), 356–358. https://doi.org/10.1364/JOSAA.17.000356

Wei, G. (2024). *Inverse design and optimization of spaceplate structures using rigorous coupled-wave analysis* [Master's Thesis]. Aalto University, School of Electrical Engineering. https://aaltodoc.aalto.fi/items/7f31f1df-33ba-4347-b595-1af112e6ff83

Yariv, A., & Yeh, P. (2007). *Photonics: Optical electronics in modern communications*. Oxford University Press.

Yuan, W., Li, L.-H., Lee, W.-B., & Chan, C.-Y. (2018). Fabrication of microlens array and its application: A review. *Chinese Journal of Mechanical Engineering*, *31*(1), 1–9. https://doi.org/10.1186/s10033-018-0204-y

A

Photonic bands of periodic media

The theory in this appendix was taken from chapter 12 from Yariv and Yeh, 2007.

A periodic thin film stack is equivalent to a one-dimensional crystal, meaning one can move through the structure with a distance equal to an integer amount of periods and find the same exact structure as before the translation. As an equation:

$$n^2(z) = n^2(z + \Lambda) \tag{A.1}$$

Where Λ is the length of a single period. An example of a finite version of such a structure can be seen in figure A.1.

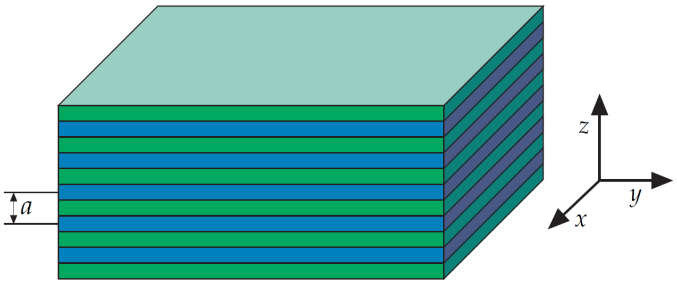

Figure A.1: A finite periodic structure with a period consisting of two layers. Figure adapted from Joannopoulos et al., 2011

Using the Bloch theorem, one can state that the electric field vector of a normal mode of propagation in a periodic medium can be written as:

$$\mathbf{E} = \mathbf{E}_K(z)e^{-iKz}e^{i(\omega t - k_y y)} \tag{A.2}$$

Where $\mathbf{E}_K(z)$ is a periodic function, depending on K (the Bloch wavenumber) and with a period Λ such that:

$$\mathbf{E}_K(z) = \mathbf{E}_K(z + \Lambda) \tag{A.3}$$

Furthermore, within a periodic medium, one can relate the forward and backward traveling wave at either end of a single period inside the structure by using the transfer matrix formalism which is laid out in section 2.1.1, which leads to a single 2x2 matrix representing the transformation done through a single period (the unit-cell translation matrix):

$$\begin{pmatrix} v_{n-1} \\ w_{n-1} \end{pmatrix} = \begin{pmatrix} A & B \\ C & D \end{pmatrix} \begin{pmatrix} v_n \\ w_n \end{pmatrix} \tag{A.4}$$

Where v and w represent the forward and backward traveling wave, respectively and subscripts n and $n + 1$ represent the number of periods Λ at which they occur.

By combining equations A.2, A.3 and A.4, one can come to:

$$\begin{pmatrix} v_{n-1} \\ w_{n-1} \end{pmatrix} = \begin{pmatrix} A & B \\ C & D \end{pmatrix} \begin{pmatrix} v_n \\ w_n \end{pmatrix} = e^{iK\Lambda} \begin{pmatrix} v_n \\ w_n \end{pmatrix} \tag{A.5}$$

This is an eigenvalue problem, which can be solved to find:

$$e^{iK\Lambda} = \frac{1}{2}(A + D) \pm \sqrt{\frac{1}{4}(A + D)^2 - 1} \tag{A.6}$$

Which is equivalent to:

$$\cos K\Lambda = \frac{1}{2}(A + D) \tag{A.7}$$

Finally, this allows derivation of K itself:

$$K(\omega, k_y) = \frac{1}{\Lambda} \arccos\left(\frac{1}{2}(A + D)\right) \tag{A.8}$$

In which A and D are themselves dependent on ω and k_y. Here k_y is the transverse component (meaning perpendicular to the optical axis) of the k-vector of the transmitted plane wave.

Additionally, one can see that finding the forward and backward traveling wave through a stack consisting of many periods can now simply be expressed as:

$$\begin{pmatrix} v_n \\ w_n \end{pmatrix} = e^{-inK\Lambda} \begin{pmatrix} v_0 \\ w_0 \end{pmatrix} \tag{A.9}$$

In which n and Λ are always real numbers. The consequence of equations A.8 and A.9 is that with purely real Bloch wavenumbers $K(\omega, k_y)$, factor $e^{-inK(\omega,k_y)\Lambda}$ will merely represent a phase transformation of incoming light. However, should $\frac{1}{2}(A + D)$ exceed a value of 1, then K will have an imaginary component, which will lead to an evanescent wave, meaning it would exponentially decay through the structure like in figure A.2a. These cases represent a photonic bandgap, a region of (ω, k_y) which cannot be transmitted through the crystal structure, assuming it consists of an infinite amount of periods. If there are defects in these structures, transmissive states may occur however, like in figure A.2b. Explicitly taking this resonance into the period of the structure instead shows that the transmissive property increases massively, as in figure A.2c.

An example of photonic bands of a perfectly periodic structure is given in figure A.3. The Brewster angle in this specific case exists only in states that have no possible incoming angle from air, meaning that for p-polarization it is possible to find a wavelength (range) for which no transmission is possible at any angle.

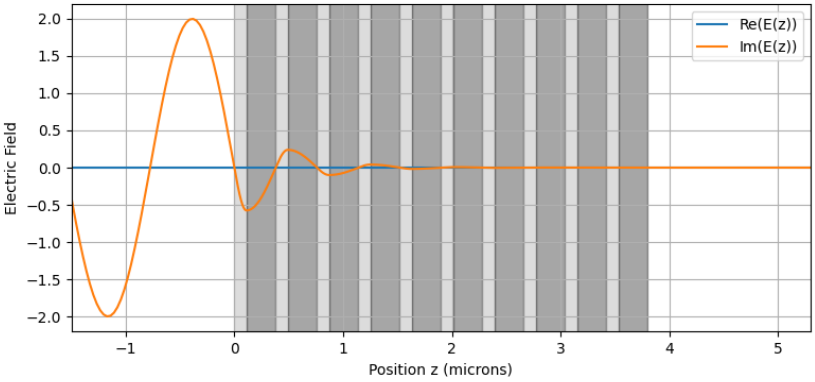

(a) Bragg mirror without defects

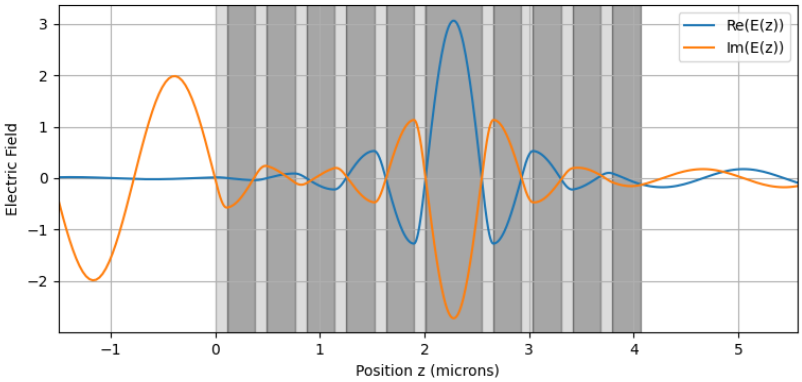

(b) Bragg mirror with single defect, being a double layer thickness

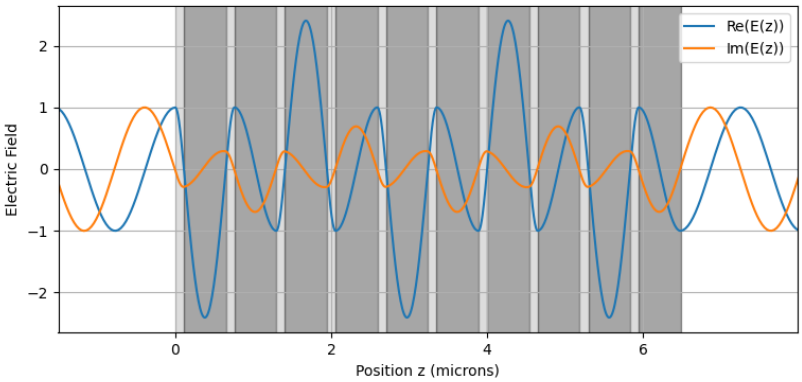

(c) Repeating structure of subsequent quarter-wave and half-wave thicknesses

Figure A.2: Electric field amplitude of light at normal incidence traveling through selected structures. (a) Exponentially decaying waves in a Bragg mirror with refractive indices 3.48 and 1.44 with 10 periods. (b) The result of a single defect layer with half-wave instead of quarter-wave thickness. (c) A periodic structure with alternating quarter-wave and half-wave thick layers.

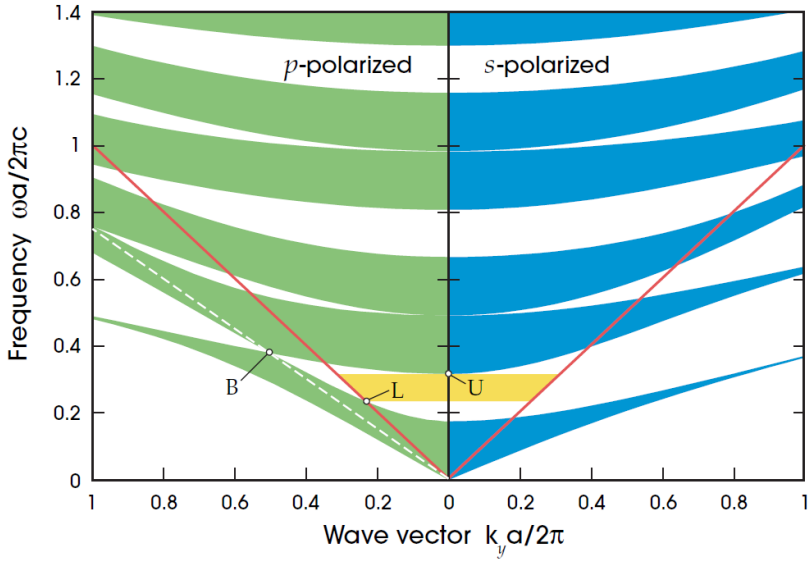

Figure A.3: Photonic bands of a quarter-wave stack with dielectric constants ε of 13 and 2. Incoming angles through air only exist above the straight red line, the light line ($\omega = ck_y$). The white dashed line represents the Brewster angle, causing a crossing at B. The yellow shaded region between lower edge L and upper edge U represents the range of wavelengths that will be reflected in air regardless of incoming angle. Figure adapted from Joannopoulos et al., 2011.

B

Fabry-Pérot spaceplate derivation

To come to equations 1.15 and 1.17, a comparison of the structure with a series of parallel LC-circuits (electrical inductor capacitor circuits) was made (supplementary text of Chen and Monticone, 2021). This comparison can be seen in figure B.1.

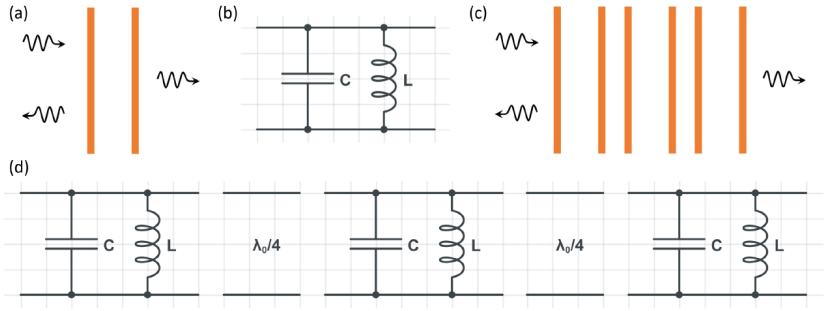

Figure B.1: **a** A single resonant structure. **b** A parallel LC resonator representing the structure in a. **c** A number n resonant structures in series. **d** A series of n parallel LC resonators in series with quarter-wavelength transmission line segments in between, representing the structure in c.

To make this comparison, a few assumptions are made. First and foremost, it is assumed that the frequency of light traveling through the structure is very close to the first even Fabry-Pérot resonance. Secondly, in this narrow band of frequencies the spacers of $\lambda_0/4$ give a global added phase of $\pi/2$ each, regardless of (angular) frequency. Lastly, the LC-circuit comparison assumes normal incidence, meaning $k_{xy} = 0$. However, at oblique incidence it approximates the response relatively well, if a shift of the resonant frequency $\omega_r = \omega_r(k_{xy})$ is taken into account.

Taking the assumptions as true, this comparison can be made using the derivation found in the supplementary text of Monticone and Alù, 2016, and in this case delivers:

$$L = \frac{2\varepsilon_1\eta_0}{\pi\omega_r(\varepsilon_1 - 1)(1 + \sqrt{\varepsilon_1} + \varepsilon_1)} \tag{B.1}$$

$$C = \frac{\pi(\varepsilon_1 - 1)(1 + \sqrt{\varepsilon_1} + \varepsilon_1)}{2\varepsilon_1\eta_0\omega_r} \tag{B.2}$$

According to Chen and Monticone, 2021, a single LC-resonator will then have the complex transmission coefficient:

$$t = \frac{-2i\omega L}{-2i\omega L + \eta_0 - LC\eta_0\omega^2} \tag{B.3}$$

By using the fact that $LC = \omega_r^{-2}$ and by using parameter $\gamma_0 = \frac{\omega_r^2 L}{\eta_0}$ one can rewrite to get:

$$t = \frac{2\omega\gamma_0}{2\omega\gamma_0 - i(\omega^2 - \omega_r^2)} \tag{B.4}$$

By assuming then that $\omega \approx \omega_r$, the right term in the denominator can be rewritten:

$$\omega^2 - \omega_r^2 = (\omega - \omega_r)(\omega + \omega_r) \approx 2\omega(\omega - \omega_r) \tag{B.5}$$

This results in a complex transmission for a single resonator:

$$t = \frac{\gamma_0}{\gamma_0 - i(\omega - \omega_r)} \tag{B.6}$$

With a non global phase:

$$\arg(t) = \arctan(\frac{\omega - \omega_r}{\gamma_0}) \approx \frac{\omega - \omega_r}{\gamma_0} + \mathcal{O}\left[\left(\frac{\omega - \omega_r}{\gamma_0}\right)^3\right] \tag{B.7}$$

Chen and Monticone, 2021 then states that for a chain of n of these resonators the resonators can be assumed to be decoupled if $\omega \approx \omega_r$. This makes the total complex transmission of the stack, including the quarter wavelength spacers, equal:

$$t = \frac{2y(\gamma_0\omega_r)^n}{(iy - \gamma_0\omega_r)(\omega_r(\omega_r - \omega) - y)^n + (iy + \gamma_0\omega_r)(\omega_r(\omega_r - \omega) + y)^n} \tag{B.8}$$

In which:

$$y = \omega_r\sqrt{(\omega - \omega_r)^2 - \gamma_0^2} \tag{B.9}$$

This is then expanded in a Taylor series:

$$t = (i)^{n-1}\left[1 + in(\frac{\omega - \omega_r}{\gamma_0}) + \mathcal{O}(\omega - \omega_r)^2\right] \tag{B.10}$$

Here $(i)^{n-1}$ represents the contribution of the spacers with $\pi/2$ per spacer, which is assumed to be a global phase, and the right part of the equation represents the phase imparted depending on incoming angle. By only looking at the phase contribution of the right term, this leaves the imparted phase of n resonators as:

$$\arg(t) = \arctan(n\frac{\omega - \omega_r}{\gamma_0}) \approx n\frac{\omega - \omega_r}{\gamma_0} + \mathcal{O}\left[n\frac{\omega - \omega_r}{\gamma_0}\right]^3 \tag{B.11}$$

C

Different situations of three-lens spaceplate

This appendix shows the functioning of the three-lens system as a spaceplate in different situations. This is to highlight the fact that regardless of position in the beam, the system will still work as a spaceplate. It also shows that the light within the second space between lenses inside the system will not always be collimated, underlining the need for the space between these lenses from a ray optics perspective. All of the situations drawn out in this appendix have the same exact incoming/outgoing angle. Ideal thin lenses are in black, and focal planes of the external lenses in red.

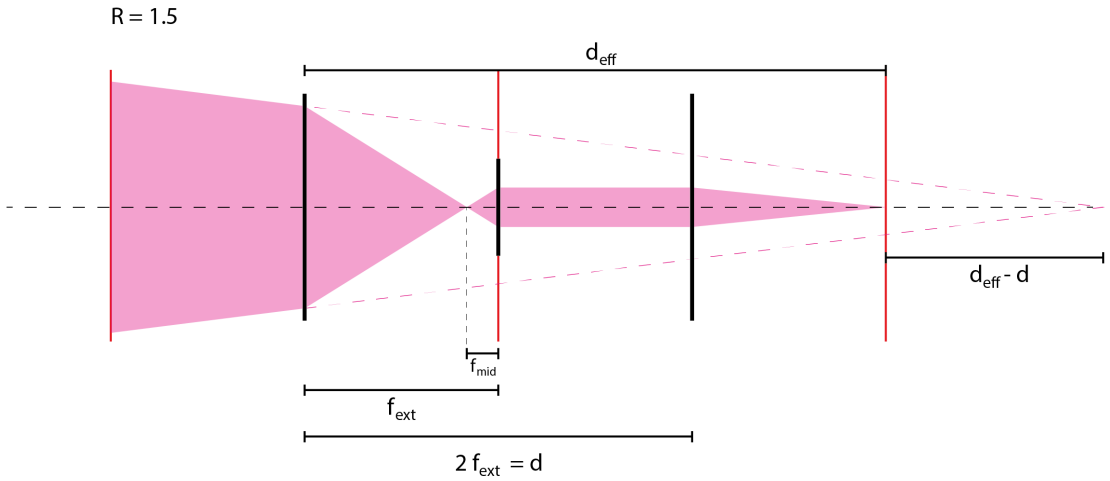

Figure C.1: Situation with focus at focal distance of last lens.

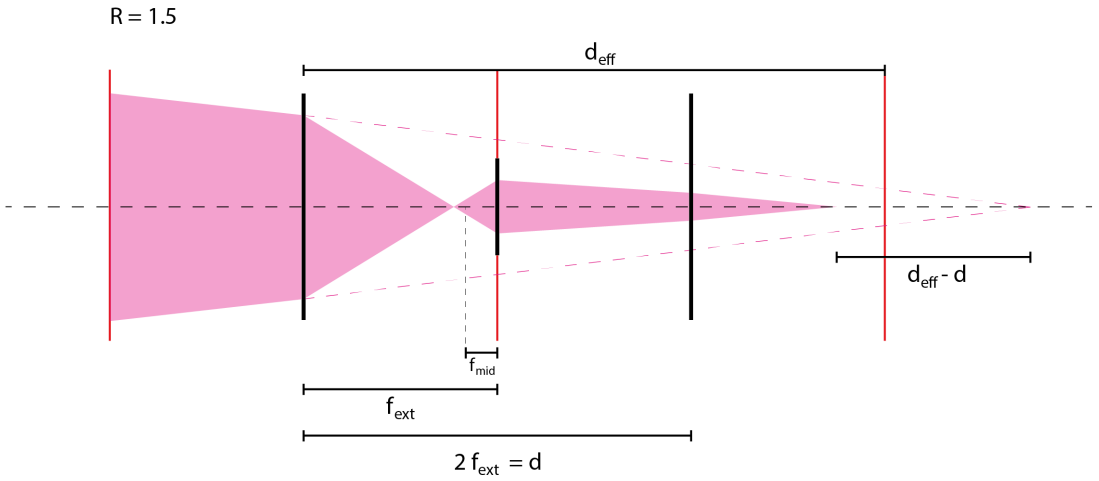

Figure C.2: Situation with focus before focal distance of last lens.

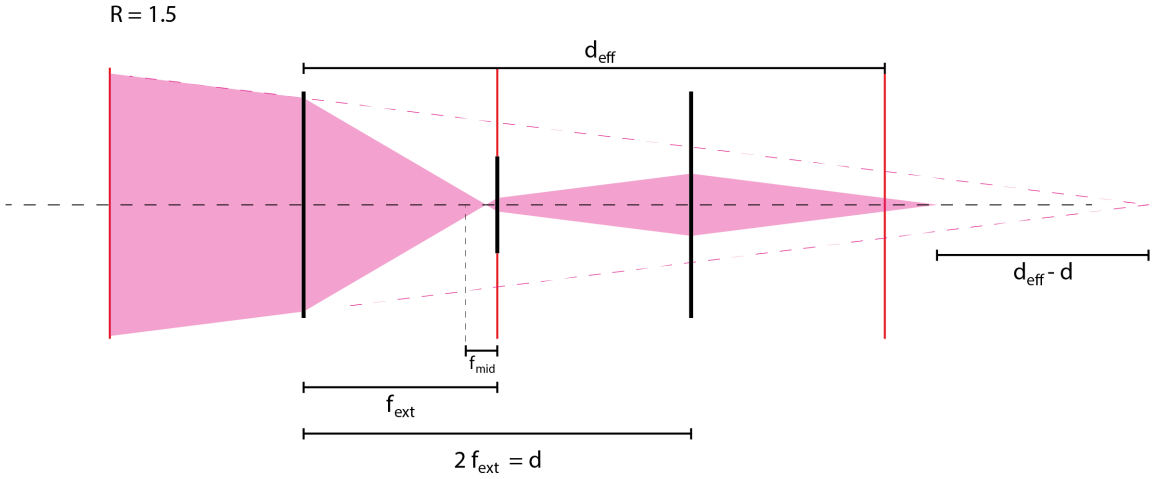

Figure C.3: Situation with focus behind focal distance of last lens.

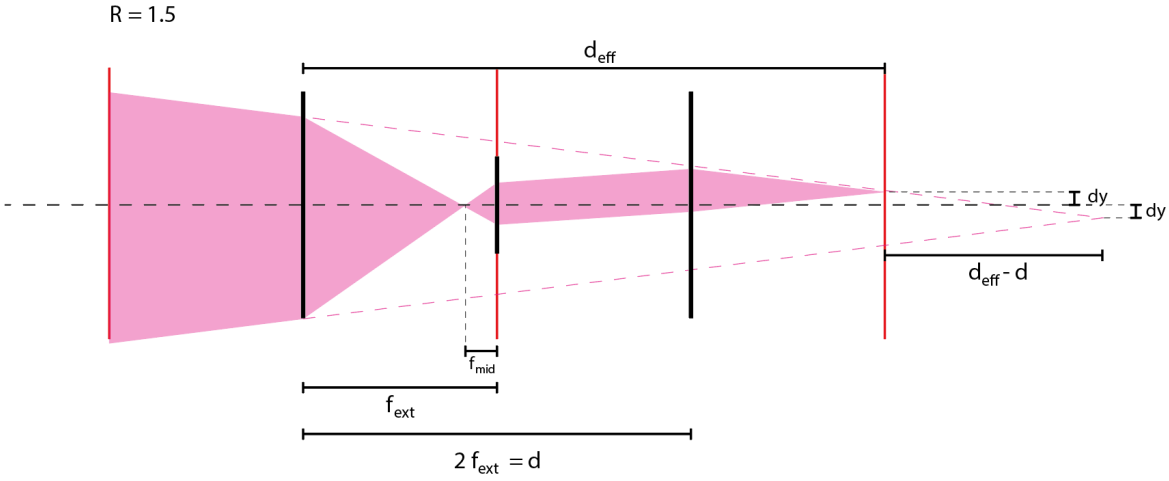

Figure C.4: Situation with off-axis incoming beam, focus again at focal distance of last lens, showcasing the mirroring about the optical axis.

D

Periodic angular stray light filters

For the sake of readability of figures, not all periodic angular stray light filter representations could be shown in section 3.4. In total, there were six periodic filters, of which two were optimized with a period of two layers, two with a period of four, and two with a period of six. Every pair had one version which was optimized by repeating the period 500 times before evaluating the figure of merit, and one which was repeated 1000 times instead. The intention is that this simulates the design strategy used when designing a periodic angular stray light filter based on photonic bands, which are generated under the assumption of infinite periodicity.

Of all designs shown here, consistently, the ones used in section 3.4 were the ones corresponding to the brown and orange line in the plots shown in this appendix. They were chosen based on their performance in the figures shown in this appendix, and so most other periodic solutions will have worse performance than those shown in section 3.4.

The contrast and suppression ratio versus the number of layers of each of the periodic designs for a tolerance region of 0 degrees can be seen in figure D.1.

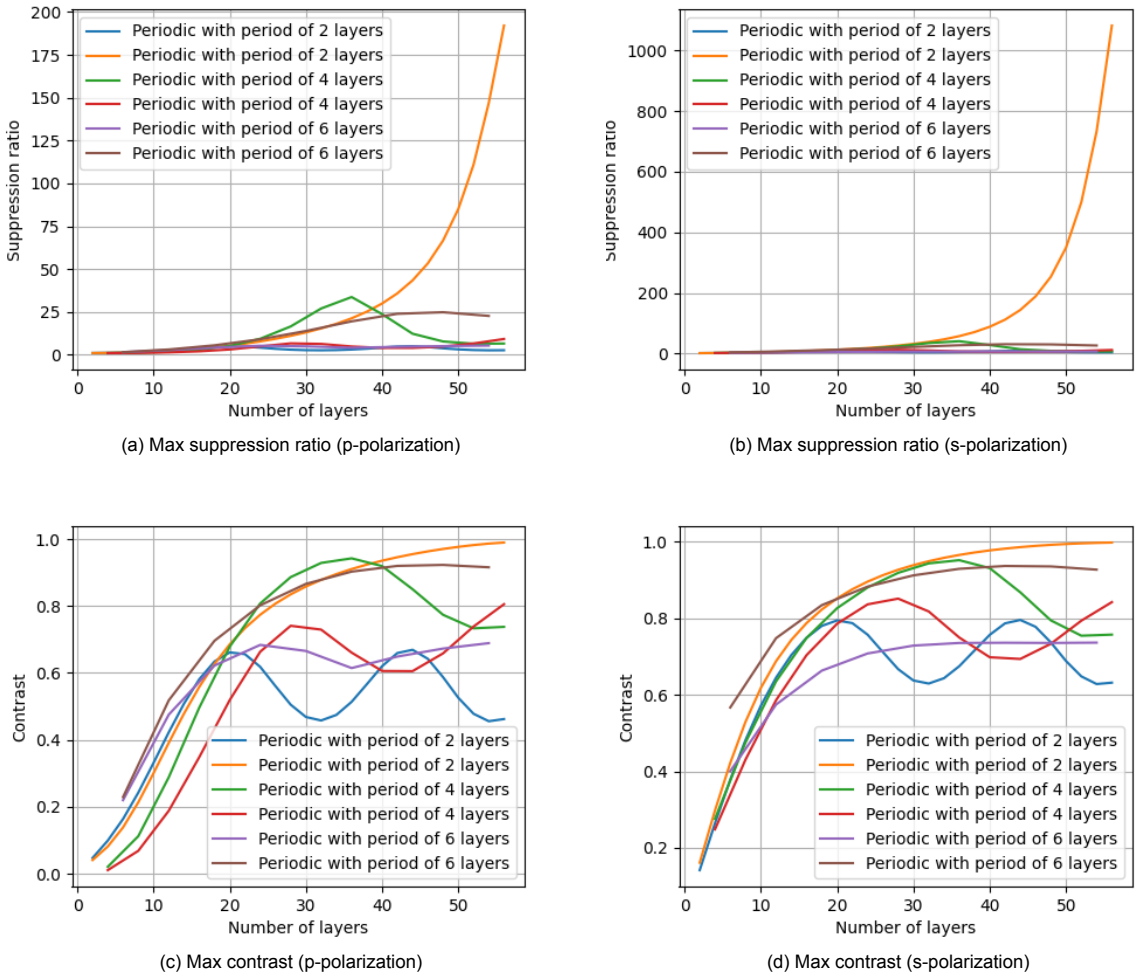

(a) Max suppression ratio (p-polarization)

(b) Max suppression ratio (s-polarization)

(c) Max contrast (p-polarization)

(d) Max contrast (s-polarization)

Figure D.1: Maximum contrast and suppression ratio found versus number of layers in the structure, for both p- and s-polarized light, plotted assuming no tolerance region is permitted.

Using 24 layers just as in section 3.4.1, the resulting contrast and suppression ratio of the periodic designs can be seen in figure D.2. One of the periodic solution has a very low contrast at an approximate tolerance region size of 80 degrees, which is due to a transmission intensity peak at this location. In the worst cases, this could even become negative, as the definition for contrast assumes $\bar{T}_w > \bar{T}_f$ and otherwise will become negative.

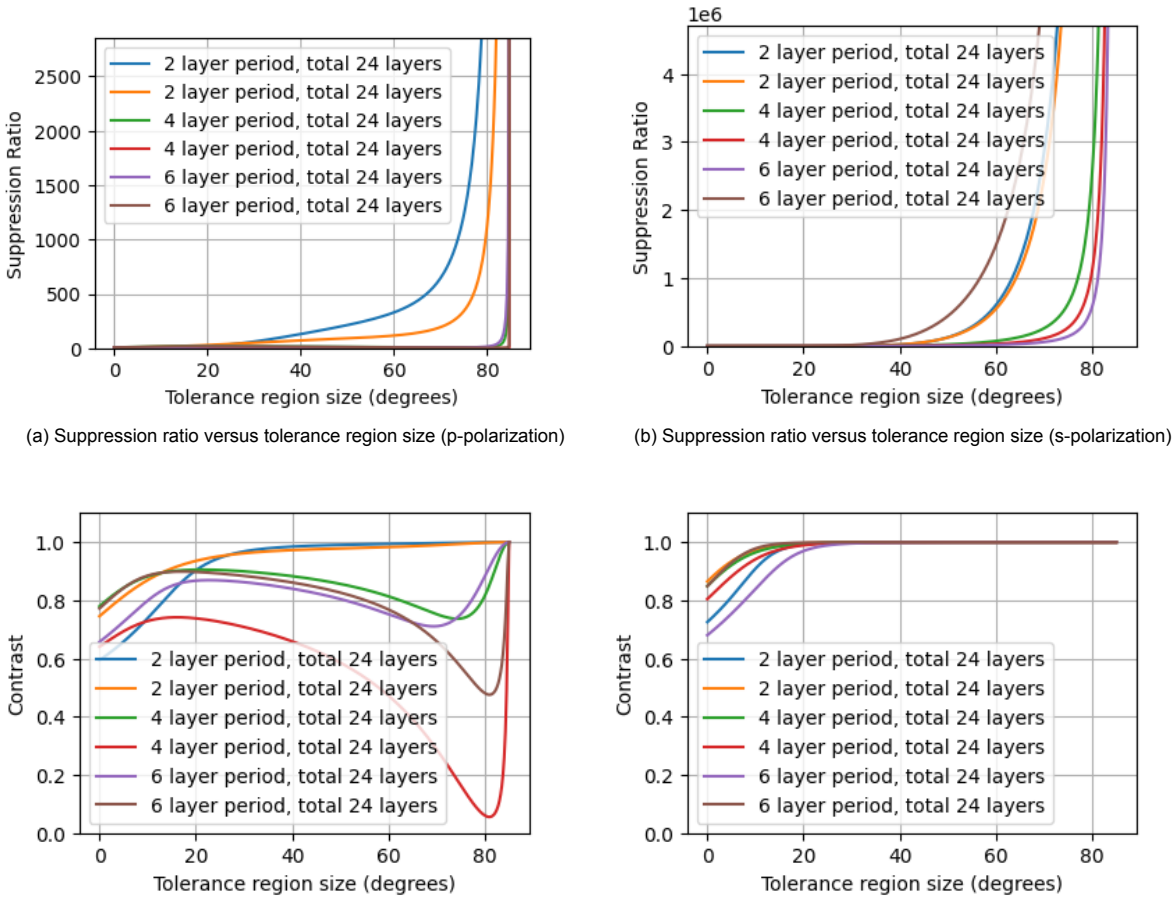

(a) Suppression ratio versus tolerance region size (p-polarization)

(b) Suppression ratio versus tolerance region size (s-polarization)

(c) Contrast versus tolerance region size (p-polarization)

(d) Contrast versus tolerance region size (s-polarization)

Figure D.2: Contrast and suppression ratio found versus number of layers in the structure, for both p- and s-polarized light for a 24-layer structure.

Continuing with the 24-layer design, the mean contrast and suppression ratio at a tolerance region of 0 degrees of the generated defect samples of all periodic designs are shown in figure D.3. Lastly, the resulting best 10% of samples are shown in figure D.4. Here, the nonperiodic solution from figure 3.24 are still shown and colored, with all periodic solutions being grayed out.

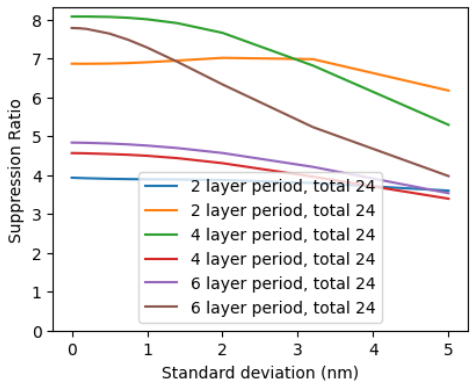

(a) Suppression ratio versus standard deviation (p-polarization)

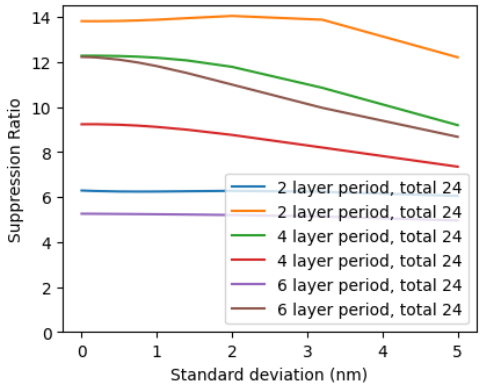

(b) Suppression ratio versus standard deviation (s-polarization)

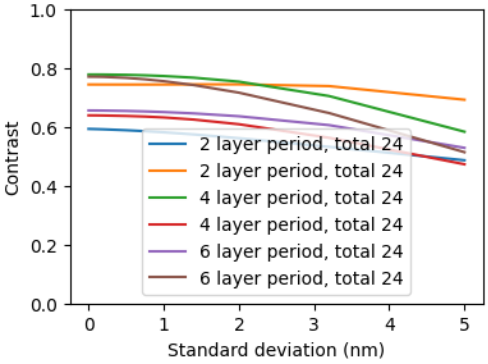

(c) Contrast versus standard deviation (p-polarization)

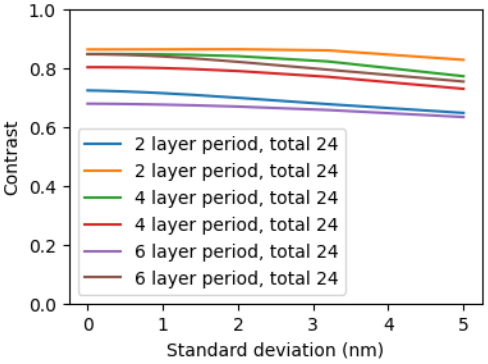

(d) Contrast versus standard deviation (s-polarization)

Figure D.3: Mean contrast and suppression ratio found versus standard deviation of layer thicknesses, for both p- and s-polarized light for a 24-layer structure with a tolerance region of 0 degrees.

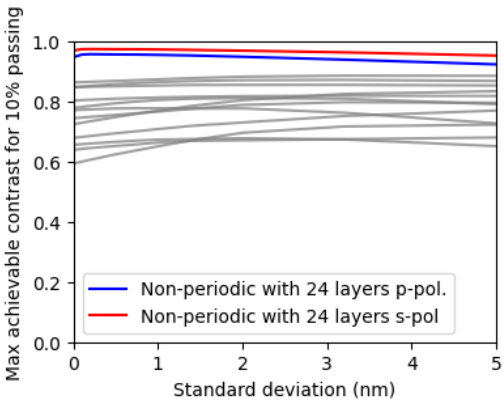

(a) Average contrast of best 10% of defect structures versus standard deviation of layer thicknesses

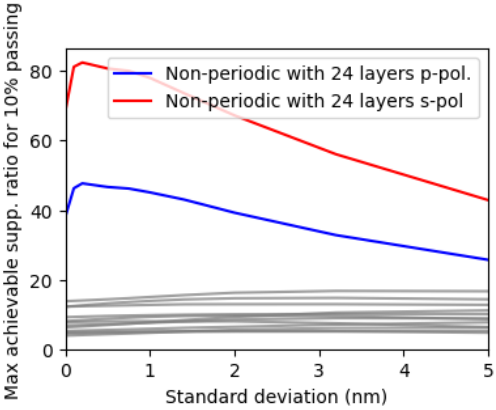

(b) Average suppression ratio of best 10% of defect structures versus standard deviation of layer thicknesses

Figure D.4: Average contrast and suppression ratio the best 10% of defect structures, in which all non-labeled gray lines are the results from the periodic devices, with no permitted tolerance region..